2019

Radiotherapy Response Using Intravoxel Incoherent Motion Magnetic Resonance Imaging in Liver Patients Treated with Stereotactic Body Radiotherapy

Benjamin C. Lewis
Virginia Commonwealth University

RADIOTHERAPY RESPONSE USING INTRAVOXEL INCOHERENT MOTION MAGNETIC RESONANCE IMAGING IN LIVER PATIENTS TREATED WITH STEREOTACTIC BODY RADIOTHERAPY

A dissertation submitted in partial fulfillment of the requirements for the degree of Doctor of Philosophy at Virginia Commonwealth University.

by

BENJAMIN CHARLES LEWIS

B.A. Washington University in St. Louis - 2014

Director: Siyong Kim,

Professor, Department of Radiation Oncology

Virginia Commonwealth University

Richmond, Virginia

May, 2019

Acknowledgements

During my time at Virginia Commonwealth University I had the fortune of working under the direction of two advisors, over three time periods, and receiving the benefits of their combined scientific insights and clinical expertise. I am thankful for Dr. Siyong Kim, my advisor when I entered the program and now as I conclude my time here, for sharing his wisdom and providing a wealth of knowledge. For Dr. Taeho Kim, my advisor through the bulk of my studies, I thank him for providing a continuous challenge to my ability, and pushing me to be the best researcher I could be. I would also like to thank Dr. William Song for his guidance and enthusiasm in research and the direction of our graduate program. This work would not have been possible without the support and knowledge provided by Dr. Joel Steinberg. I am thankful for the contributions of Dr. Emma Fields, who's guidance provided invaluable insights into the clinical applicability of this work. For Dr. Christopher Chipko, I am thankful for his energy and enthusiasm in collaborating with me, and his work on image fusion and contouring. Additionally, I thank Robert Cadrain for his technical insights on image acquisition with MRI. I am also grateful to the Collaborative Advanced Research Imaging (CARI) program at the VCU Wright Center for Clinical and Translational Research for providing the use of their research MRI machine. I am thankful for the financial support provided by the VCU Health Department of Radiation Oncology, and the American Cancer Society.

Finally, I would like to thank the members of our program that offered guidance, feedback, and emotional support throughout my time here: Katie Goracke, Sarah Holler, Matthew Riblett, Nicky Mahon, Mark Ostyn, Siqiu Wang, Samantha Conrad, and my professors throughout the years. Thank you to everyone for all you have done.

Abstract

RADIOTHERAPY RESPONSE USING INTRAVOXEL INCOHERENT MOTION MAGNETIC RESONANCE IMAGING IN LIVER PATIENTS TREATED WITH STEREOTACTIC BODY RADIOTHERAPY

By Benjamin Charles Lewis

A dissertation submitted in partial fulfillment of the requirements for the degree of Doctor of Philosophy at Virginia Commonwealth University.

Virginia Commonwealth University, 2019.

Director: Siyong Kim,
Professor, Department of Radiation Oncology

Magnetic resonance imaging is utilized as an important tool in radiation oncology for delineation of healthy and cancerous tissues, and evaluating the functionality of those tissues, structures, and organs. Currently, the clinical imaging protocol at Virginia Commonwealth University includes anatomical imaging for tissue and structure delineation, and to observe treatment induced changes. Diffusion weighted imaging (DWI) is also acquired for calculation of apparent diffusion coefficient (ADC) values to provide quantitative information on tissue diffusivity and microstructure. However, anatomical images and ADC values may not display the true extent of changes in tissue. This work seeks to further utilize the capabilities of MRI and expand its role in treatment response monitoring for liver cancer patients treated with stereotactic body radiotherapy (SBRT). To do so, an imaging protocol and image analysis methodology to evaluate treatment changes on pre- and post-treatment image sets was developed. An extension of DWI, termed intravoxel incoherent motion

(IVIM) imaging, was utilized to quantitatively assess levels of perfusion and diffusion within the liver and tumor. Acquisition of high quality diffusion weighted images of the liver necessitated the development of an MR safe respiratory motion management device, which was designed, constructed and evaluated in this work. An imaging protocol was developed providing anatomical and functional images of the liver, acquired under breath hold, utilizing the respiratory motion management device. An IVIM parameter calculation and texture analysis workflow was developed using MATLAB, and applied to acquired data sets from multiple studies, including past clinical cases, investigator, healthy volunteer, and liver cancer patient. Differences in IVIM and texture analysis parameters were investigated for healthy and diseased tissue, and for select dose regions from pre- and post-treatment imaging sessions. Significant differences, at a voxel level, were found between healthy and diseased tissue, and pre- and post-treatment volumes, for multiple parameters, including apparent diffusion coefficient, pure diffusion, and perfusion, as well as for various texture features. Overall, this study showed the potential of IVIM and texture analysis to be used for discriminating between healthy and diseased tissues in the liver, and for indication of treatment response.

TABLE OF CONTENTS

Abbreviations

4DCT 4 Dimensional CT

ABC Active breathing coordinator

ADC Apparent diffusion coefficient

AP Anterior-posterior

BH Breath hold

BTFE Balanced turbo field echo

BW RF pulse bandwidth

CBCT Cone beam computed tomography

CoV Coefficient of variation

CT Computed tomography

CTsim Computed tomography simulation

CTV Clinical target volume

D Diffusion coefficient

D* Perfusion coefficient

DCE Dynamic contrast-enhanced

DRR Digitally reconstructed radiograph

DVH Dose volume histogram

DWI Diffusion weighted imaging

FB Free breathing

FID Free induction decay

Fx Treatment fraction

GI Gastro-intestinal

GLCM Gray level co-occurrence matrix

GUI Graphical user interface

HBV Hepatitis B virus

HCC Hepatocellular carcinoma

HCV Hepatitis C virus

IGRT Image guided radiotherapy

IMRT Intensity modulated radiotherapy

IVIM Intravoxel incoherent motion

MI Mutual information

ML Mediolateral

MVCT Megavoltage computed tomography

NMR Nuclear magnetic resonance

NSA Number of signal averages

PDI Power-data interface

PF Perfusion fraction

PGSE Pulsed gradient spin echo

PTV Planning target volume

RF Radio-frequency

RMM Respiratory motion management

SBRT Stereotactic body radiotherapy

SE Spin echo

SI Superior-inferior

SRS Stereotactic radiosurgery

T1w T1 weighted

T2w T2 weighted

TA Texture analysis

TE Echo time

TFE Turbo field echo

TSE Turbo spin echo

US Ultrasound

LIST OF TABLES

LIST OF FIGURES

CHAPTER 1

INTRODUCTION

A major barrier to effective treatment in oncology, and specifically radiation oncology, is the ability to predict treatment outcome for individual patients. Predicting response becomes increasingly important for more aggressive treatments, such as stereotactic body radiotherapy (SBRT), where high doses of radiation are delivered to the target area of the patient in five or fewer treatment sessions. Being able to determine if a patient will respond positively to a treatment where the possibility of radiation induced toxicity is high may prevent those with little to gain from aggressive treatment from experiencing increased risk.

This work uses multiple diffusion weighted images of the liver acquired both pre- and post-treatment to calculate quantitative data using an intravoxel incoherent motion model (IVIM), and texture feature analysis, to investigate indicators for efficacy of SBRT treatment. These quantitative parameters provide information on tissue change that is not apparent on current clinical imaging protocols. This work is the first application of the full IVIM method to radiation response of SBRT in the liver and produces a robust and accurate image processing architecture to accurately quantify functional data from the acquired images.

1.1 Liver Tumors

Tumors occur when cell reproductive cycles and growth checkpoints do not function normally. This unregulated cell division results in an abnormal mass of tissue, which can impact normal organ function and spread to other parts of the body. Tu-

mors found in the liver are identified as liver tumors and can be grouped into two main categories: primary or secondary.

Primary liver tumors arise from multiple types of cells, including hepatocytes, the lining of the bile duct, and the cell lining of liver blood vessels. Hepatocellular carcinoma, starting in the hepatocytes, is the most common type of primary liver cancer.

Secondary liver cancer refers to metastases found in the liver. These cancers do not originate in the liver, but are the result of cancer cells separating from a primary tumor site elsewhere in the body, being transported through the blood or lymphatic system, and being deposited at the metastasis site. These metastatic tumors of the liver are more common than primary liver tumors in the United States [1].

1.1.1 Primary Liver Tumors: Hepatocellular Carcinoma

Hepatocellular carcinoma (HCC) is the most common primary liver malignancy, the leading cause of cancer-related death worldwide, and the ninth leading cause of cancer death in the United States [2]. Risk factors associated with HCC include chronic liver disease, cirrhosis, and diabetes. Chronic viral Hepatitis B and C (HBV and HCV) demonstrate the highest risk of hepatocarcinogenicity, and the odds of HCC occurrence increase 8-fold when both HBV and HCV are present [3, 4, 5]. Diabetes is an independent risk factor for HCC, and shows up to a 4-fold increased risk of HCC [5, 6]. The high mortality rate is due to diagnosis of HCC at an advanced stage with severe liver impairment [7]. Screening modalities for HCC include radiographic tests and serological marker. Ultrasound (US), computed tomography (CT), and MRI with contrast are all current viable radiological tests, with US being the most common [8]. However, US has poor sensitivity to small HCC nodules, less than 2cm in diameter, and obesity can further reduce ultrasound's ability to detect

these small lesions [9]. Multiple treatment methods exist for HCC, including surgical resection, liver transplant, transarterial chemoembolization, transarterial radiation, percutaneous local ablation, microwave ablation, and focal radiation. Surgical resection retains its position as the mainstay of treatment for HCC, with a 5-year survival of 41% to 74%. However, some tumors are not resectable due to tumor size, location, liver function, and if the remaining liver volume will allow for resection without drastic increase in morbidity and mortality [10]. Recently, advances in radiotherapy have allowed for treatment of HCC with radiation to become more effective, especially when focal radiation is applied at high doses, as in stereotactic body radiotherapy, which will be described in following sections. Radiation therapy causes damage to both diseased and healthy tissue by damaging genetic material such as DNA within the tumor cell, limiting the cell's ability to reproduce or resulting in mitotic progeny which are unable to replicate [11, 12]. If a tumor cell is less able to repair DNA damage than healthy cells, radiotherapy is a viable treatment, and the cumulative effect of unrepaired DNA strand breaks can result in cell death of tumor cells at a rate higher than the healthy cell death rate.

1.1.2 Secondary Liver Tumors

Liver metastasis is a result of malignant tumors elsewhere in the body. The most common sites of primary tumor are breast, lung, and colorectal cancer [13, 14, 15, 16]. Some studies have reported hepatic metastasis in as many as 40 to 50% of adult patients with extrahepatic primary tumors [16]. The high incidence of hepatic metastases has been attributed to two mechanisms [16]. First, the dual blood supply of the liver from the portal vein and systemic circulation increases the likelihood of metastatic cell deposition in the liver. Second, the hepatic sinusoidal epithelium has fenestrations, which enable easier penetration of the metastatic cells into the liver

parenchyma.

1.2 Stereotactic Body Radiotherapy

1.2.1 General SBRT

Stereotactic radiosurgery (SRS) was first described in 1951 by Leksell, using a frame based system to direct narrow beams of radiation at a target in the brain, described by a 3D coordinate system [17]. SRS has since been vastly improved, with implementation no longer requiring a fixed frame attached to the patient for guidance, and extension of the method beyond the brain to the rest of the body with a method called stereotactic body radiotherapy. With this expansion of methodology, the main principles remain the same, delivery of a high dose radiation beam with rapid dose fall-off outside of the target volume, extreme dose conformality of the prescribed dose to the target, and extremely high repositioning accuracy [18]. The rapid dose fall-off allows for high doses to be delivered over a few fractions, using a hypofractionated treatment, while sparing normal tissue in close proximity to the target volume. Treatment in typical intensity modulated radiotherapy (IMRT) plans is delivered in 1-3Gy fractions, over 10 or more fractions, while in SBRT plans typically deliver 10-20Gy/fx, and only 1-5 fractions for the entire course of treatment [19]. To achieve normal tissue sparing, margins around the target must be reduced significantly. The increased treatment accuracy is produced by utilizing immobilization equipment, including vacuum lock air bags, leg restraints, and head and neck masks. Immobilization equipment alone is often not sufficient to achieve the desired tumor localization due to respiratory motion and initial setup error. Target motion due to respiratory motion can be significantly reduced with utilization of breath hold techniques at inhale or exhale. As an example, the liver position can deviate by up to 4cm

during regular respiratory motion in the cranio-caudal direction, and this motion can be reduced to a reproducible position within 0.4cm using an active breathing coordinator (ABC) [20]. Further target localization can be achieved using image guidance, again allowing for reduced dose to normal tissues and improved tumor control [21]. To perform image guided radiotherapy (IGRT), the patient is imaged just prior to treatment delivery, and corrections applied to match the planning CT or digitally reconstructed radiographs (DRRs) [22]. On-board imaging can be performed with a broad spectrum of imaging modalities, such as on-board cone beam CT (CBCT), megavoltage CT (MVCT), MRI, orthogonal kilovoltage imaging, electromagnetic systems, optical systems, and ultrasound [23, 24]. Use of an appropriate IGRT system is especially important for abdominal lesions, such as those in the liver.

1.2.2 Liver radiotherapy and motion uncertainty

As noted in previous sections, primary and metastatic liver cancer is prevalent in the United States and around the world. Liver cancer is also distinguished by its high mortality rates and short survival periods when compared to other cancers. While surgical resection remains the primary treatment method, radiation treatment is becoming more prevalent. SBRT has emerged as an effective, non-invasive option for treatment of liver lesions [25, 26, 27]. It has been shown that there is an increase in local control rates with increased doses; however, increased doses also result in greater normal tissue complications. In addition to this, patients with primary liver tumors are more likely to suffer from liver injury as a result of radiotherapy than patients with metastatic lesions, and position of the tumor or pre-existing gastro-intestinal (GI) conditions can significantly increase the risk of GI toxicity [28, 29]. The liver, similar to the lungs, is an organ composed of parallel functioning tissue, meaning the volume of the liver irradiated must be limited, even at low doses. A summary of dose

constraints for liver radiotherapy by number of fractions can be found in Table 1. A further complication in liver SBRT is that lesions have very low contrast with healthy tissue on CT and CBCT images, resulting in difficulty during image guided set up without the use of anatomical surrogates, such as the dome of the liver and vertebral bodies.

Organ at risk	**3 fraction (RAS trial [30])**	**5 fraction (TG-101 [31])**	**QUANTEC (1.8-2Gy per fraction [32])**
Liver (excluding CTV)	700 mL < 15 Gy	700 mL < 21 Gy	D mean < 30 Gy
Esophagus	D 1 mL < 21 Gy	D 5 mL < 19.5 Gy	V 35 < 50%
Stomach	D 1 mL < 21 Gy	D 10 mL < 18 Gy	D 100 < 35 Gy
Kidney	D 35% < 15 Gy	200 mL < 17.5 Gy	D mean < 28 Gy
Bowel and duodenum	D 1 mL < 21 Gy	D 5 mL < 18 Gy	D 45 < 195 cc

Table 1. Summary of dose constraints by fractionation schedule. CTV: Clinical target volume

An example of clinical IMRT and SBRT plans are shown in Figure 1. The IMRT plan in the left column shows a much larger low dose wash, and a greater volume of the liver and kidneys receiving a high dose, than the SBRT plan in the right column.

In addition to poor tissue contrast on CT, and high dosimetric risk, organ motion in the abdominothoracic cavity can be significant. This motion can cause artifacts in abdominal imaging, resulting in decreased analytic value of images, and geometric miss of the defined target during radiation delivery. Suramo et al. suggested that the liver has a movement range of 9 mm during breath hold, increasing to 25 mm during

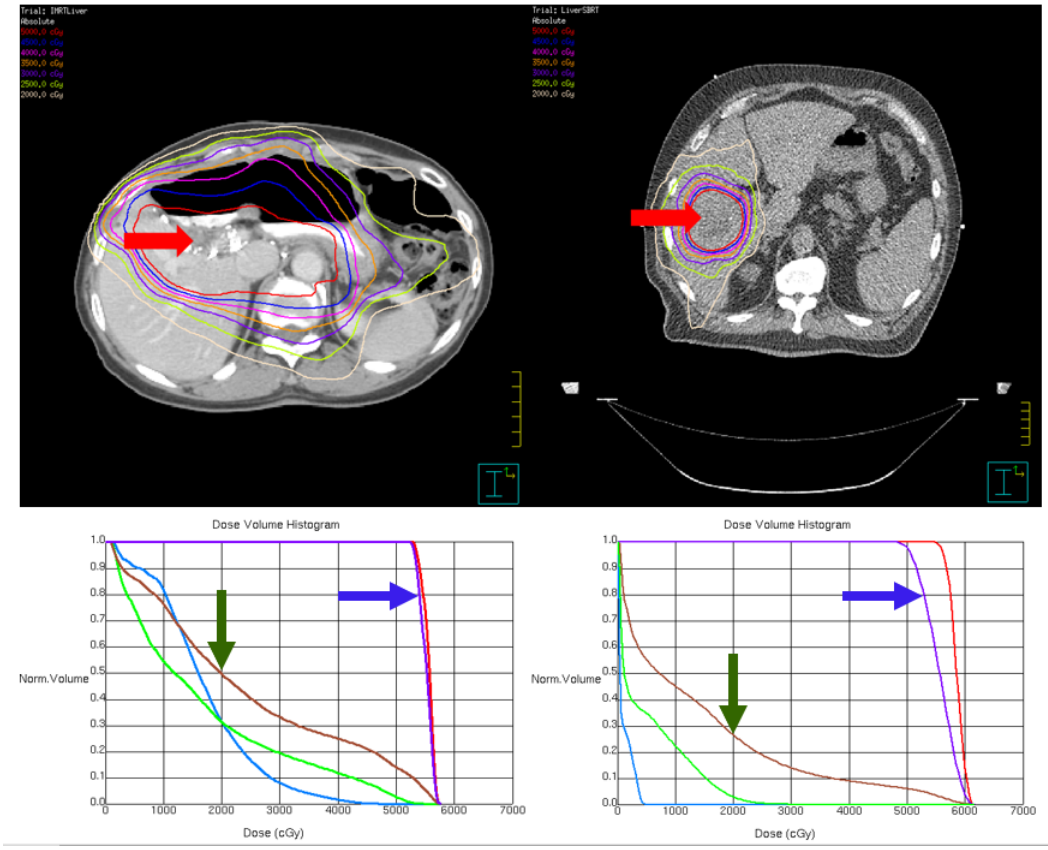

Fig. 1. The left column shows a planning CT and dose volume histogram (DVH) for a patient receiving IMRT treatment for liver cancer. The right column shows a planning CT and DVH for a patient receiving SBRT treatment for liver cancer. The red arrow indicates the position of the target volume. In the DVHs: purple line is the planning target volume (purple arrows), red line is the internal target volume or clinical target volume, brown line is the liver (brown arrows), blue is the left kidney, and green is the right kidney.

normal respiration, and becoming as high as 55 mm during maximum respiration [33, 34]. Another study by Blackall et al. found that liver motion was 19±8 mm during shallow breathing, and 37±8 mm during deep breathing [35, 36]. Danrad et al. reported that the major component of liver motion occurs along the superior-inferior (SI) direction with an average displacement of 10±8 mm, with a range of 7-28 mm, and the same is true for the diaphragm, which they found to move 12±7mm, with a range of 7-28 mm [37, 38]. The motion of the liver translates to motion of the liver tumors, with Shimizu et al. reporting a mean SI tumor displacement of 21 mm, 8 mm in the anterior-posterior (AP) direction, and 9 mm in the lateral direction [39, 40]. A further collection of live motion data can be found in Table 2. Many studies also assume the liver as a rigid body; however, Paulsson et al. reported that the liver frequently experiences intraorgan deformation and a study of fiducial markers found that the rigid body estimation has an average error of 7.1 mm with a range of 1.9-11.4 mm at the periphery of the liver [41]. These deformations decreased toward the central part of the liver, with an average error of 3.4 mm, ranging from 0.5-9.1 mm.

1.2.3 Magnetic resonance imaging for radiotherapy

Magnetic resonance imaging is a powerful tool in radiation oncology, with the unique ability of being able to perform both anatomical and functional imaging, while providing no ionizing radiation dose to the patient, and providing soft tissue contrast vastly superior to CT imaging. This difference in soft tissue contrast becomes especially stark when comparing CTsim images to MR, as in Figure 2. In addition to improved anatomical imaging, MRI can produce functional image acquisitions which provide detail on the tissue micro-environment. These specialized acquisition protocols will be further discussed in Chapter 2.

Author et al.	**Description**	**AP (mm)**	**ML (mm)**	**SI (mm)**
Case [42] (29 patients)	Mean (range)	4.3 (0.1-12.1)	1.8 (0.1-7.0)	8.0 (0.1-18.8)
Hallman [43] (18 patients)	Mean (range)	4.8 (1-16)	-	9.7 (3-18)
Yang [44] (14 patients)	Mean	4.5	17.5	7.1
Dhont [45] (18 patients)	Mean	5.1	2.4	11.8
Wysocka [46] (22 patients)	Free breathing mean (range)	2.0 (0.1-8.9)	1.8 (0.1-9.5)	6.5 (0.5-24.0)
	Expiration mean (range)	1.6 (0.2-21)	1.4 (0-8.2)	1.6 (0.2-21.0)
	Inspiration mean (range)	4.2 (0.2-14.0)	2.0 (0.1-9.5)	3.8 (0.1-30.0)

Table 2. Summary of liver motion during respiration using fluoroscopy, 4DCT, and dynamic MRI acquisition.

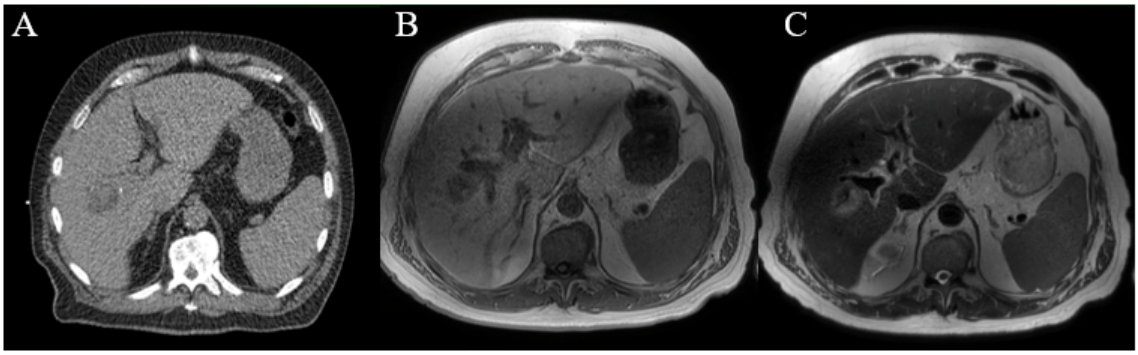

Fig. 2. Example of images acquired on a wide bore CT scanner for CT simulation (A), and a T1w (B) and a T2w (C) image from a 3T MRI at the same position on different days. The tumor mass is visible on all three images; however, it is most easily delineated on the MR images.

Standard prognostic factors currently include stage, grade, histology, and patient comorbidities; however, histology sampling is not always a possibility, and the other factors do not provide a detailed description of the micro-environment of the tumor. Dynamic contrast-enhanced (DCE) MRI has become a widely used tool to investigate the perfusion and permeability of tumors [47]. DCE utilizes a contrast agent, and rapid MR image acquisitions post injection, to follow the temporal enhancement pattern of tissue as the contrast agent moves through the vascular system. The measured signal intensity depends on the concentration of the injected paramagnetic particles, which enter and disperse through the tissue. Pharmacokinetic analysis of the signal intensity curves is then used to calculate K^{trans}, the transfer constant for contrast agent transport from the blood plasma into the extravascular extracellular space, and v_e, the volume fraction of the extravascular extracellular space. Previous studies have also shown DCE-MRI to be correlated with tumor oxygenation, vascularity, and cellular proliferation [48, 49, 50]. However, to perform DCE, contrast agents must be administered to the patient, which often include gadolinium and other compounds that can do significant damage to the kidneys if renal function is impaired, resulting

in nephrogenic systemic fibrosis, and some studies have shown uptake of gadolinium in the brain in patients with no history of kidney disease [51]. Damage to the kidneys is suspected to be caused by reduction in medullary blood flow leading to hypoxia and direct tubular damage due to the toxicity of contrast media. Measuring response without contrast agents has been performed using DW imaging, fat- or water-saturated T2 sequences, and vascular enhancement imaging using in- and out-of-phase T1 sequences [52, 53]. Mardor et al. found that ADC of brain metastases slightly increased one day post-treatment, with further increases over time. A 40% increase in ADC 7 days post-treatment was associated with an 89% decrease in tumor volume 55 days post-treatment [52]. In hepatocellular carcinoma, Oldrini et al. found that the absence of a hyperintense region in DWI correlated with the probability of complete response three months later on the subsequent MRI [53]. To the author's knowledge, the only study utilizing IVIM methods for measuring tumor response to radiotherapy is for breast cancer liver metastases undergoing radio-embolization; however, the study uses a simplified version, utilizing only three b-values, which is often considered insufficient for accurate quantification [54].

1.3 Radiotherapy respiratory motion management

To achieve the required position, immobilization equipment including vacuum lock air bags, leg restraints, and hand holds are used to prevent the patient from moving while on the table, and multiple imaging modalities are used to align the patient to the correct position [55]. However, none of these methods succeed in sufficiently achieving tumor localization due to respiratory motion. Multiple techniques have been developed to mitigate respiratory motion, including self-enforced breath hold, device-enforced breath hold with an active breathing coordinator unit, compression using hard plastic plates or belts, and machine gating to the patients

respiratory pattern [56]. These methods have all been shown to decrease respiratory motion, but often are only implemented during CT simulation (CTsim) for treatment planning and on the treatment machine. Further, the respiratory motion management devices are not compatible with MRI machines. MR imaging is an integral part of diagnosing, planning, and treatment response monitoring, but without a consistent motion management mechanism across imaging platforms, it can be difficult to register multi-modality images and assess changes to the anatomy.

1.4 Summary of complications

Within radiotherapy of the liver, and MR imaging for assessing radiotherapy response, this work identifies three major difficulties. The first issue is the absence of a respiratory motion management device that can be utilized across the radiotherapy treatment process, including at the treatment machine, during CT imaging, and during MR acquisition. A robust motion management device is required to acquire high quality abdominal diffusion weighted images without motion artifacts, and to correctly position the patient for treatment delivery. The second complication is what imaging protocol to use, including number of b-values, number of signal averages, respiratory motion management technique, and image acquisition technique. The correct choice of protocol will allow for high quality and sufficient input data for IVIM parameter calculation. Finally, the third complication of interest is the absence of a standardized IVIM parameter calculation workflow for comparison of tissue types and radiotherapy induced tissue changes. A standard protocol is vital to the application of IVIM parameters in the clinical setting, and for extension of the protocol to other institutions. The following specific aims, in Section 1.5, were set forth to address these identified complications.

1.5 Specific aims

The work in this dissertation aimed to develop an MR safe respiratory motion management system which provides biofeedback to the subject, and investigate the application of IVIM models and texture analysis in patients with liver cancer. The study focuses on post-processing image analysis of the liver and cancerous liver lesions acquired under breath hold, and the development of a software toolbox to easily and reliably generate tissue maps of the investigated biomarkers. This work also presents the first application of the full IVIM method to tumor response in radiotherapy to the author's knowledge, as previously stated.

Hypothesis: quantitative tissue parameters obtained using IVIM imaging and analysis can provide information on tumor and liver changes for liver cancer patients treated with SBRT, and can identify changes not visible using the current clinical imaging protocol.

1. To develop an MR safe respiratory motion monitor and manager, which also provides biofeedback to the patient. This system will be usable in both imaging and treatment environments, and will introduce minimum image artifacts in both MRI and CT acquisitions.

   This aim addresses the absence of a suitable respiratory motion management system usable across all platforms involved in radiotherapy, addressed in section 1.3.

   (a) Develop a respiratory motion manager and monitor, which provides biofeedback to the subject, and is usable across MR and CT imaging systems, as well as RT delivery systems.

(b) Evaluate the reduction of respiratory motion when utilizing the system, and introduction of imaging artifacts.

2. To develop a set of MR imaging sequences that provide anatomical and functional information for the liver. This imaging protocol will include multiple DW images to be used with the IVIM imaging method, anatomical imaging sequences (T1w and T2w), and other quantitative or qualitative image acquisitions.

3. To develop a workflow for analyzing images acquired with the imaging protocol developed in aim 2, which produces a comparison of tissue information from pre- and post-treatment imaging sessions for liver cancer patients treated with SBRT.

   (a) Investigate methods for improving IVIM parameter map quality utilizing image registration and de-noising.

   (b) Apply workflow to IVIM datasets and identify parameter changes from pre- and post-treatment delivery.

In addition to development of a novel RMM device, imaging protocol, and workflow for IVIM analysis, a graphical user interface (GUI) was created to improve the ease of use for the workflow, described in Chapter 7. The GUI was designed to incorporate each part of this work into a modular system, where the operator can decide what image post-processing and analysis features to use. The MATLAB code for this system is included in the Appendices of this work. Further, an initial assessment of liver tissue change with dose region was performed for one week post-treatment and one month post-treatment imaging data sets. Although the number of patients

available for this study is limited, it lays the ground work for a large clinic-wide study and can also be extended to other disease sites.

CHAPTER 2

DIFFUSION AND PERFUSION WEIGHTED MR IMAGING

This Chapter provides background on MR imaging, and how it can be used to provide functional details of the tissue micro-environment and micro-structure.

2.1 MR Imaging

MR imaging utilizes the physical phenomenon known as nuclear magnetic resonance (NMR). NMR and the idea of nuclear spin are introduced here. Hydrogen-1, Carbon-13, Fluorine-19, Sodium-23, and Phosphorous-31 atoms all exhibit NMR and can be found in the human body [57]. ^{1}H is the most common isotope in the human body, constituting approximately 70% of the adult human body. Because of this, protons are the most common isotope utilized for clinical MR imaging [58]. From here on, the discussion will focus on the ^{1}H isotope

2.1.1 NMR

NMR active nuclei are those which possess nuclear spin. Nuclear spin is a property of nuclei containing unpaired nucleons (neutrons and protons), each of which possess a nuclear spin of one half. The unpaired nucleon results in a non-zero spin quantum number ($\mathbf{I}$), and possesses spin angular momentum ($\mathbf{S}$).

$$\mathbf{S} = \hbar \mathbf{I} \tag{2.1}$$

where $\hbar$ is Planck's constant (divided by 2π). In the case of ^{1}H, $\mathbf{I} = 1/2$, corresponding to the single proton in the nucleus. Associated with $\mathbf{S}$ is a magnetic

Nucleus	$\gamma/2\pi$ **[MHz/T]**	**Relative Sensitivity**
^{1}H	42.577	1.000
^{13}C	10.705	0.016
^{19}F	40.054	0.830
^{23}Na	11.262	0.093
^{31}P	17.235	0.066

Table 3. Gyromagnetic ratios and relative sensitivities for NMR isotopes [57].

dipole moment μ, defined in equation (2.2).

$$\mu = \gamma \mathbf{S} = \gamma \hbar \mathbf{I} \tag{2.2}$$

where γ is the gyromagnetic ratio, a known constant unique to different nuclear species. Values for γ can be found in Table 3.

When $\mathbf{S}$ is defined along a given axis, it defines the number of possible spin orientations along that axis and is defined by equation (2.3).

$$\mathbf{S} = 2\mathbf{I} + 1 \tag{2.3}$$

For an ^{1}H nucleus, this results in two possible spin states, $m = +1/2$ and $m = -1/2$. Absent an external magnetic field, these two spin states are degenerate and have no net magnetic moment. If these nuclei are subjected to a static magnetic field, the interactions between μ and $\mathbf{B}_0$, the static magnetic field, result in a splitting of spin states, and a net magnetization moment, $\mathbf{M}$.

These two energy states are separated by ΔE, described in equation (2.4).

$$\Delta E = \gamma \hbar B_0 = h \frac{\gamma}{2\pi} B_0 \tag{2.4}$$

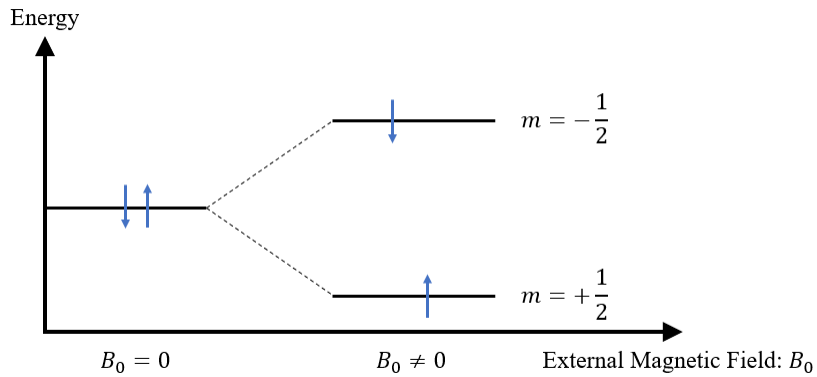

Fig. 3. Energy level diagram for a proton nucleus in the absence of an external magnetic field ($\mathbf{B}_0 = 0$) and spin splitting in the presence of an applied magnetic field ($\mathbf{B}_0 \neq 0$).

The $+1/2$ spin state is of less energy than the $-1/2$, and tends to have the higher population; however, thermal energy is sufficiently high at room temperature to exceed the energy separation. This results in the population ratio to be dependent on the Boltzmann distribution, described in equation (2.5)

$$\frac{+1/2}{-1/2} = e^{-\frac{\Delta E}{kT}} \tag{2.5}$$

where k is the Boltzmann constant and T is the absolute temperature. At standard temperature (273.15 K) this results in an excess of 7 in 10^6 in the parallel state, and a weak polarization macroscopically. In an applied field, the equilibrium nuclear magnetization M_0 can be calculated using (2.6)

$$M_0 = \frac{N\gamma^2\hbar^2 I_z(I_z+1)B_0}{3kT} \tag{2.6}$$

where N is the number of nuclear spins per unit volume. This shows that M_0 is proportional to the applied external magnetic field B_0. It is this M_0 that is manipulated in MR imaging and forms the basis for all acquisition methods. The applied

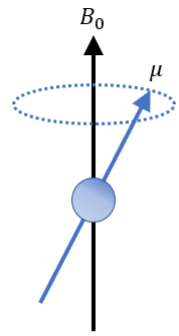

Fig. 4. Precession of a nucleus in an external magnetic field.

magnetic field also imposes a torque on the nuclear spins, resulting in a precession, which is proportional to γ and the applied magnetic field, as shown in equation (2.7), and Figure 4.

$$\omega = \frac{\gamma B_0}{2\pi} \tag{2.7}$$

2.1.2 RF pulses

A magnetic field B_1 applied in the transverse direction of the M_0, with a frequency equivalent to the resonant frequency of the M_0 results in a transition between spin-states, and generates an NMR signal when the magnetization vector, M, precesses orthogonally to the applied field. Under Faraday's law of induction, an electromotive force is induced within the receiver coil. The maximum NMR signal is produced when the radio-frequency (RF) pulse brings the M vector parallel to the xy transverse plane. This corresponds to an RF pulse with intensity and duration resulting in a rotation of 90 degrees. The rotation angle is known as the tip angle or flip angle (Θ), which is calculated using equation (2.8)

$$\Theta = \gamma B_1 \tau \tag{2.8}$$

where B_1 is the generated RF field and τ is the time duration of the applied pulse. M will continue to precess about the z-axis at a precessional frequency proportional to the applied field. Over time, M will eventually return to its equilibrium state along the z axis, and the signal decay over time is called the free induction decay (FID). This implies that the longitudinal component M_z must regrow, and the transverse component M_{xy} must decay. The MR parameters T_1 and T_2 characterize this return to equilibrium, and are known as relaxation time constants.

2.1.3 Relaxation

The excited spins return to thermal equilibrium by spin-lattice (T_1), and spin-spin (T_2) relaxation processes, shown in Figure 5. Longitudinal relaxation, or T_1 relaxation, corresponds to spins moving between energy levels to restore thermal equilibrium. Moving from high to low energy states results in a release of energy from the spins to the surrounding environment, the lattice. The T_1 time constant is defined as the time it takes for the signal to recover back to 63% of its original value and is described by equation (2.9) [59]

$$M_z = M_0(1 - e^{-\frac{t}{T_1}}) \tag{2.9}$$

where t is the time delay allowed for longitudinal relaxation. The T_2 relaxation, or transverse relaxation, corresponds to the loss of phase coherence in the xy plane. After an RF pulse, spins have a phase coherence by aligning in the transverse plane. Inter- and intra-molecular interactions disrupt this phase coherence, which is eventually lost. The T_2 time constant is described by equation (2.10) [59].

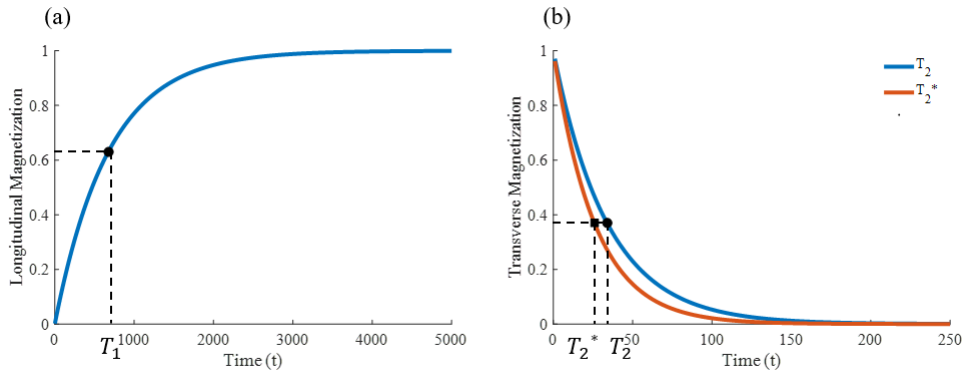

Fig. 5. Relaxation of an excited spin back to thermal equilibrium. Recovery of M_z with longitudinal recovery and decay of M_{xy} with transverse relaxation over time. The T_1 relaxation time is defined as 63% of M_0. The T_2 relaxation time is defined as reduction of M_{xy} to 37% of M_0

$$M_z = M_0 e^{-\frac{t}{T_2}} \tag{2.10}$$

The T_2 time constant is highly susceptible to inhomogeneities in the applied magnetic field, and the true decay recorded by the receiver coils is significantly faster than natural T_2. This faster rate is denoted as T_2*, and can be considered the observed or effective T_2

The three orthogonal components of the magnetization, M_x, M_y, and M_z can be explicitly written using the following Bloch equations:

$$\begin{cases} \frac{dM_x}{dt} = \gamma M_y B_0 \\ \frac{dM_y}{dt} = -\gamma M_x B_0 \\ \frac{dM_z}{dt} = 0 \end{cases} \tag{2.11}$$

When taking into account relaxation effects, the Bloch equations become:

$$\begin{cases} \frac{dM_x}{dt} = \gamma M_y B_0 - \frac{M_x}{T_2} \\ \frac{dM_y}{dt} = -\gamma M_x B_0 - \frac{M_y}{T_2} \\ \frac{dM_z}{dt} = \frac{M_z - M_0}{T_1} \end{cases} \tag{2.12}$$

The signal recorded during MR imaging is the transverse complex magnetization, $M_{xy}(t)$, which is a combination of $M_x(t)$ and $M_y(t)$, $M_{xy}(t) = M_x(t) + iM_y(t)$. The Bloch equations become:

$$\begin{cases} \frac{dM_{xy}}{dt} = -i\gamma M_{xy} B_0 - \frac{M_{xy}}{T_2} \\ \frac{dM_z}{dt} = \frac{M_z - M_0}{T_1} \end{cases} \tag{2.13}$$

To solve this set of equations, we assume that at $t = 0$, the magnetization is only present in the z-direction. Thus, the initial conditions for the magnetization are $M_{xy}(t = 0) = 0$ and $M_z(t = 0) = M_0$. Solving equation (2.13) with these initial conditions results in:

$$\begin{cases} M_{xy}(t) = M_0 e^{\frac{-t}{T_2}} e^{-i\gamma B_0 t} \\ M_z(t) = M_0(1 - e^{\frac{-t}{T_1}}) \end{cases} \tag{2.14}$$

2.1.4 Image acquisition

The previous equations described methods which apply in both MRI and NMR. This section introduces spatial encoding gradients, the main difference between MRI and NMR that allows for image acquisition. The spatial encoding gradients include the frequency, phase encoding, and slice selection gradients. These gradients apply a spatially linear variation to the static magnetic field, adding or subtracting to B_0 along their respective directions, as shown in Figure 6. Along the gradient, spins precess at a decreased or increased rate dependent on their position. By applying an

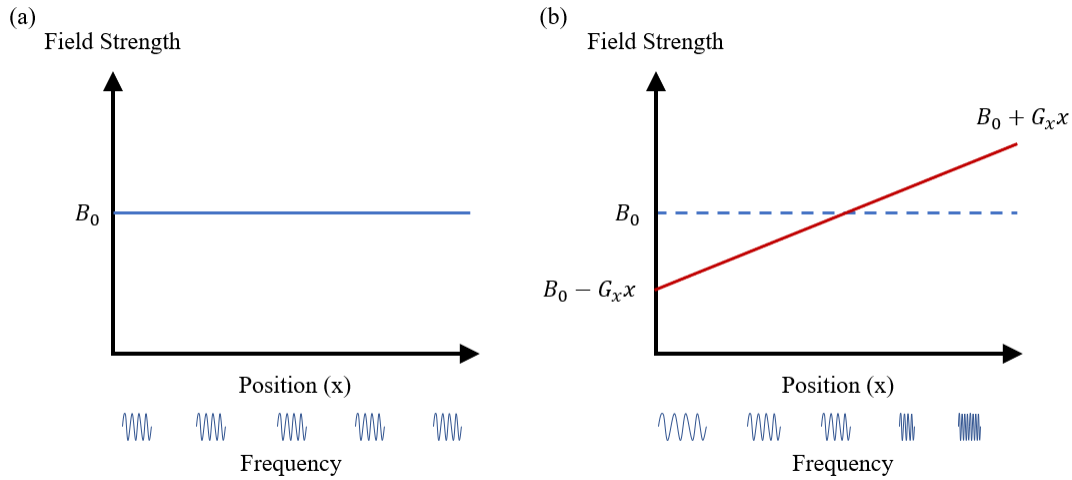

Fig. 6. An illustration of the magnetic field gradient and its impact on the B field and spin precession frequency.(a) represents the magnetic field without a gradient applied, resulting in a consistent precessional frequency over space. (b) represents the magnetic field with a gradient applied, resulting in an increase in frequency as the B field strength increases.

RF pulse associated with a frequency along this gradient a slice of thickness T can be excited, characterized by the other two directions. T is defined in equation (2.15)

$$T = \frac{BW}{\gamma G_{Slice}} \tag{2.15}$$

where BW is the RF pulse bandwidth, and G_{Slice} is the slice selection gradient.

After the slice selective excitation pulse, a gradient is applied along one of the remaining two directions. Again, spins experience different magnetic field strengths depending on their position in space, and a phase shift is introduced between $t = 0$ and the recording of the signal. The phase accumulated during a pulse sequence for a given voxel is given by the following equation

$$\phi(t) = \int_0^t \gamma \vec{G}_{Im}(t') \cdot \vec{x} dt' = 2\pi \vec{k} \cdot \vec{x} \tag{2.16}$$

where $\vec{k}$ is the encoding vector, containing the information given by the gradients. Finally, by adding a frequency encoding gradient in the third direction, the Larmor frequency of spins are separated into a spectrum, resulting in a voxel location defined by the slice, frequency, and phase information.

With the addition of complex transverse magnetization, and the presence of imaging gradients, the change in M_{xy} over time in the presence of gradient fields is considered, starting from the Bloch equation for M_{xy}.

$$\frac{dM_{xy}}{dt} = -i\gamma B_0 M_{xy} - \frac{M_{xy}}{T_2} \tag{2.17}$$

The Larmor frequency is modified by gradients as follows.

$$\omega = \gamma B_0 + \gamma \vec{G}_{im}(t) \cdot \vec{x} \tag{2.18}$$

Where $\vec{G}_{im}$ is the imaging gradient vector and $\vec{x}$ is the position vector of the observed voxel. Replacing γB_0 with ω in equation (2.17) gives:

$$\frac{dM_{xy}}{dt} = -i\omega_0 M_{xy} - \frac{M_{xy}}{T_2} - i\gamma \vec{G}_{Im}(t) \cdot \vec{x} M_{xy} \tag{2.19}$$

And when solved for M_{xy}:

$$M_{xy}(t) = M_0 \exp\left(\frac{-t}{T_2}\right) \exp\left(-i\omega_0 t\right) \exp\left(-i \int_0^t \gamma \vec{G}_{Im}(t') \cdot \vec{x} dt'\right) \tag{2.20}$$

To simplify the equation, relaxation effects are neglected and a rotating reference frame, the solution for the Bloch equation in (2.20) becomes:

$$M_{xy}(t) = M_0 \exp\left(-i \int_0^t \gamma \vec{G}_{Im}(t') \cdot \vec{x} dt'\right) \tag{2.21}$$

Using (2.16) and (2.21), a spatial frequency domain, or k-space, can be defined

that contains the location information of encoding vector $\vec{k}$. The total magnetization of a volume is expressed as:

$$M_{xy}(\vec{k}) = \int |M_{xy}(\vec{x})| e^{-i\phi(\vec{x})} d\vec{r} = \int |M_{xy}(\vec{x})| e^{-i2\pi\vec{k}\cdot\vec{x}} d\vec{x} \tag{2.22}$$

The k-space described by equation (2.22) is of equivalent size to the final image; however, a single pixel in k-space does not contain the information for a single voxel in image space. The k-space holds an array of intensities along the axes of phase and frequency. Image reconstruction using only part of k-space results in a blurred image if only central k-space is used (low spatial frequencies) and an edge defining image if the periphery of k-space is used (high spatial frequencies). An example of this can be seen in Figure 7. From equation (2.22) the magnitude of magnetization, $|M_{xy}(\vec{x})|$, can be obtained by applying an inverse Fourier transformation.

$$|M_{xy}(\vec{x})| = FT^{-1}[M_{xy}(\vec{k})] = \int |M_{xy}(\vec{k})| e^{-i2\pi\vec{k}\cdot\vec{x}} d\vec{k} \tag{2.23}$$

Application of the Fourier transform results in an x-space MR image, which may be used for image analysis.

2.1.5 Basic MR pulse sequences

To generate useful image contrast, the excitation and gradient selection pulses must be applied at precise times and durations. These are described as MR pulse sequences, a subset of which will be described below.

2.1.5.1 Gradient Echo Sequence

An illustration of the gradient echo pulse (GE) pulse sequence is shown in Figure 8. This pulse sequence utilizes 90 degree selective excitation pulse. A negative slice

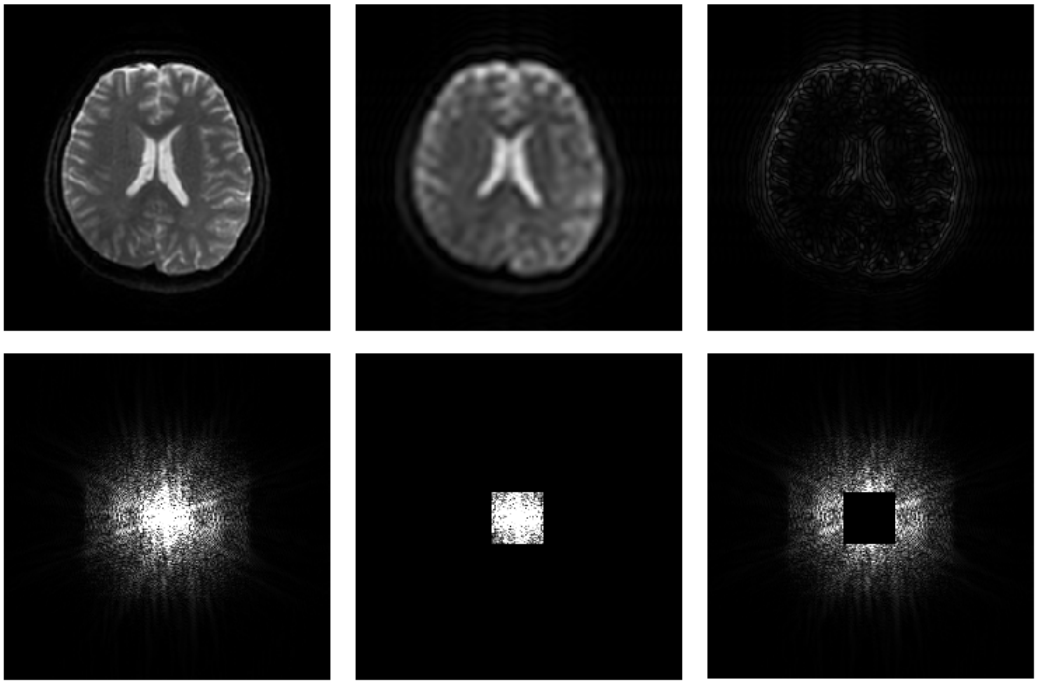

Fig. 7. K-space spectra and their reconstructed images showing: (a) reconstruction of all spatial frequencies, (b) low spatial frequencies (central 2.5% of k-space), and (c) high spatial frequencies (peripheral 97.5% of k-space)

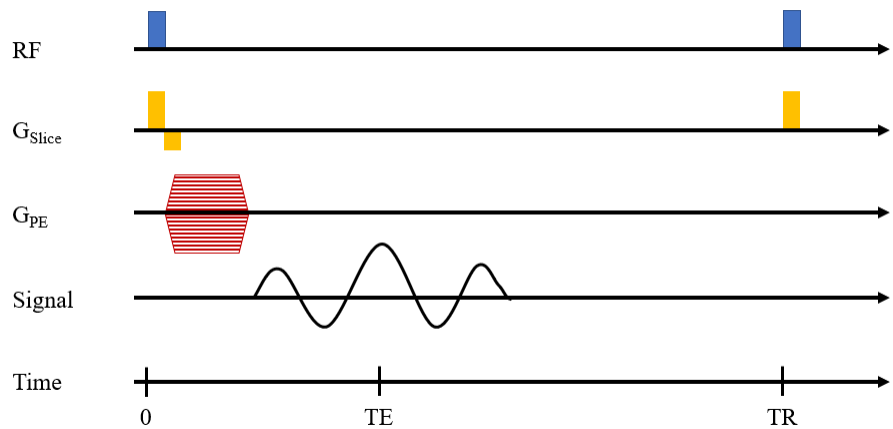

Fig. 8. Sequence diagram for GE pulse sequence.

gradient is applied, causing rapid dephasing of the transverse magnetization for a short time after the excitation pulse. After the negative lobe, a positive gradient is applied which reverses the magnetic field gradient, causing spins to rephase. This positive gradient only compensates for the negative gradient dephasing, and does not refocus dephasing due to main magnetic field inhomogeneities or spin-spin relaxation. The signal of the produced echo is determined by the FID decay curve and T_2*.

$$S_{GE} = S_0 \exp\left[-\frac{TE}{T_2*}\right] \tag{2.24}$$

2.1.5.2 Spin Echo sequence

An illustration of the spin echo (SE) pulse sequence is shown in Figure 9. This pulse sequence utilizes a 90 degree selective excitation pulse, tipping the spins into the transverse plane. After a time delay τ during which the spins are dephasing, a 180 degree refocusing pulse is applied. Spins which were previously dephasing begin to rephase, leading to the term refocusing pulse. This process is similar to the rephasing of spins in GE pulse sequences, however it utilizes an inversion RF pulse, instead of

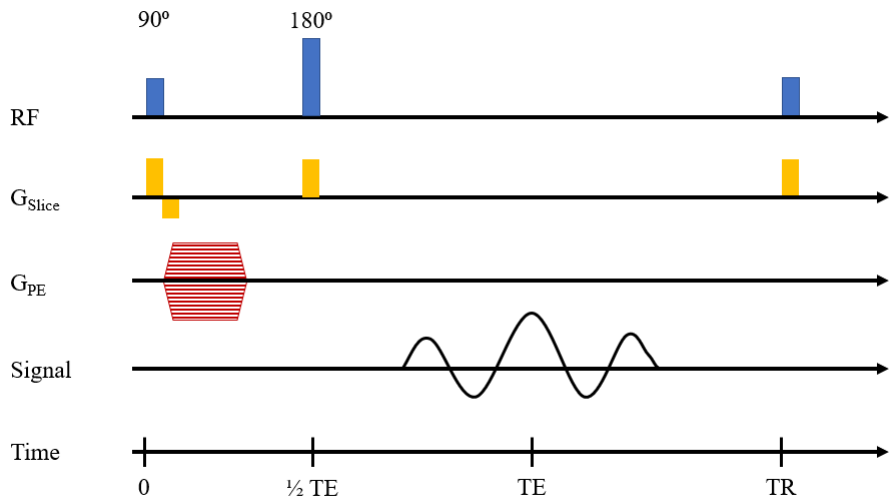

Fig. 9. Sequence diagram for SE pulse sequence.

an equal and opposite magnetic field gradient. At $t = 2\tau$, an echo forms, and this time is defined as the echo time (TE). Static spins experience the same magnetic field inhomogeneities during the time τ prior to the 180 degree pulse, and between the 180 degree pulse and the readout pulse. Due to the 180 degree pulse, T_2 can be used, instead of T_2*, to describe the signal intensity. The addition of the 180 degree RF pulse increases acquisition time compared to GE acquisitions. This pulse sequence is commonly used to produce T_2w images with a signal described by equation (2.25)

$$S_{SE} = S_0 \exp\left[-\frac{TE}{T_2} - \frac{2}{3}\gamma^2 \Delta B^2 D(\frac{TE}{2})\right] \tag{2.25}$$

where ΔB describes the magnetic field inhomogeneities, and D is the apparent diffusion coefficient (ADC) of the tissue. Because D is typically around $10^{-3} mm^2/s$ and TE is generally short compared with T_2, equation (2.25) can be simplified to:

$$S_{SE} = S_0 \exp\left[-\frac{TE}{T_2}\right] \tag{2.26}$$

2.2 Diffusion MR imaging

Diffusion weighted imaging (DWI) is an important noninvasive tool for assessing functional status of tissue in the body. This technique exploits the sensitivity of MRI to diffusion of water in tissue while in the presence of diffusion gradient pulses. The following sections will describe the origin of diffusion in the body, and how it is measured with MRI.

2.2.1 Physical and biological origins

Robert Brown studied the motion of small particles inside a fluid and found a type of motion common to all particles in this state, termed the random-walk, or Brownian motion [60]. Brownian motion is the description of microscopic diffusion phenomenon. It is caused by the thermal energy possessed by molecules, and results in molecular mixing. This diffusion is intrinsic to a medium and is dependent on the size of the molecules, temperature, and micro-structure. Albert Einstein later formulated the mathematical definition for the diffusion coefficient of a particle experiencing Brownian motion [61].

$$D = \frac{\left\langle R^2 \right\rangle}{2nT} \tag{2.27}$$

where $\left\langle R^2 \right\rangle$ is the mean squared displacement of a particle diffusing during a time T and in the dimension of displacement n. The Einstein equation describes diffusion as a Gaussian function, where the width of the distribution is determined by D. However, diffusion in biological tissue is not free, resulting in deviation from the Gaussian behavior and the molecular displacement distribution becoming sharper [62].

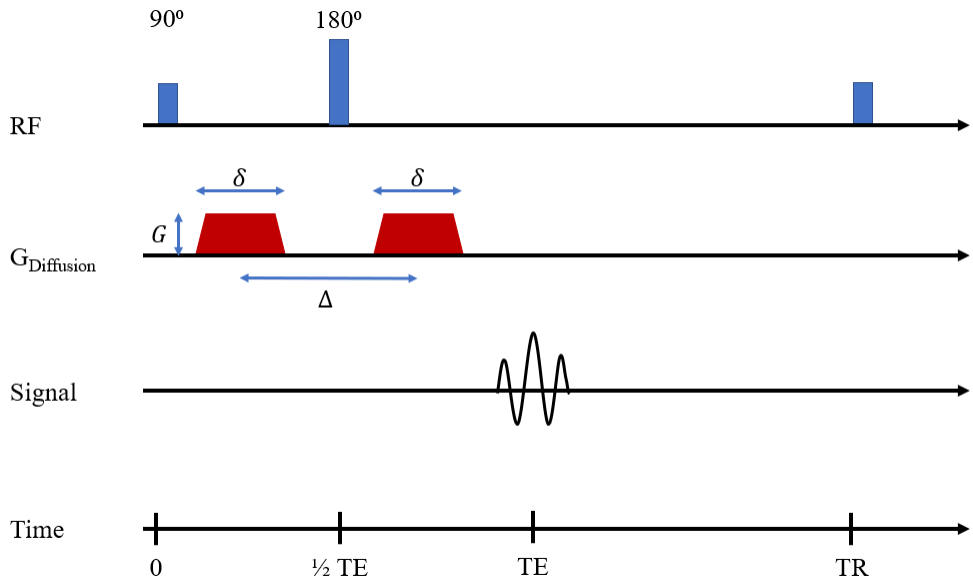

Fig. 10. Sequence diagram for a PGSE sequence.

2.2.2 Measurement with MR

The measurement of diffusion with MRI is dependent on the concept of phase. If we consider three sine waves oscillating at the same rate and at the same position along the axis, the waves have the same phase. However, if two waves are shifted in space relative to the other, the waves now have different phases, but retain the same frequency. This instantaneous position of a wave can be equated to an angle describing the position of protons relative to one another. Hahn was the first to recognize the potential of the SE sequence to measure the diffusion coefficient [63]. In 1965 Stejskal and Tanner proposed what would become the most commonly applied method for producing diffusion-weighted contrast, the Pulsed gradient spin echo (PGSE) method seen in Figure 10 [64].

The PGSE sequence adds two diffusion gradients, one before and one after the 180 degree pulse. The diffusion gradients allow differentiation between static and

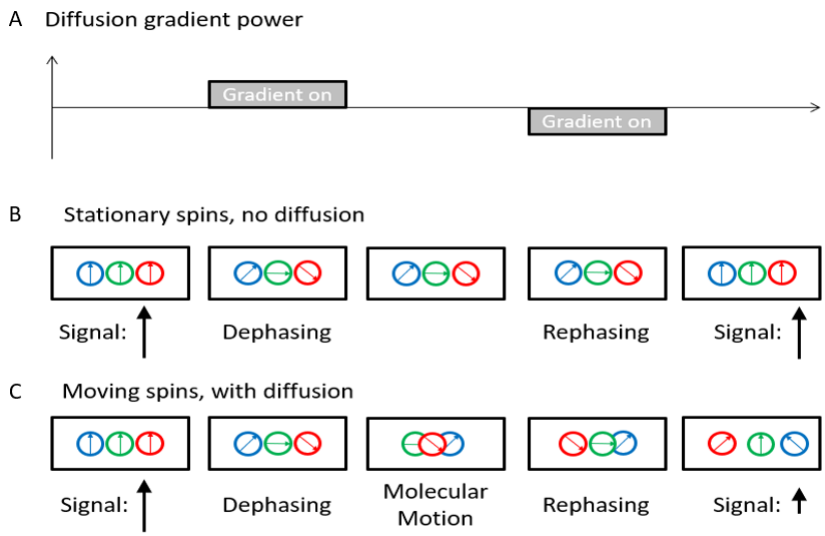

Fig. 11. A diagram of spin change during DWI when diffusion gradients are applied. (A) indicates when the diffusion gradient is powered on and in what direction. The first gradient pulse is applied, causing dephasing of spins depending on location within the slice. In the case of no diffusive motion (B) the dephased spins remain in position. When the rephrasing gradient is applied, the return to their original orientation, maintaining signal intensity. When diffusive motion is present (C) the dephased spins do not remain at a constant location between application of diffusion gradients. The change in location leads to a different magnetic field being applied during each diffusion gradient. The incomplete rephasing caused by different gradient strengths leads to reduced signal intensity.

moving spins in the voxel. The stationary spins will be completely rephased by the second gradient, while moving spins will not be. An illustration of this can be seen in Figure 11. Two other parameters are defined by the PGSE sequence: the pulse diffusion gradient duration, δ, and the time delay between the two diffusion encoding gradients, Δ. These parameters can be used to calculate the signal strength from a PGSE sequence.

$$S_{PGSE} = S_0 e^{-(\gamma\delta G)^2(\Delta - \frac{\delta}{3})D} \tag{2.28}$$

where G is the diffusion encoding gradient strength. Le Bihan proposed simplification of the exponential term by gathering parameters linked to the sequence or the type of nucleus into one parameter, b [65].

$$S_{PGSE} = S_0 e^{-bD} \tag{2.29}$$

where b is defined in equation (2.30) and is called the b-value.

$$b = (\gamma\delta G)^2(\Delta - \frac{\delta}{3} \tag{2.30}$$

The time that spins are allowed to diffuse is represented by the diffusion time $T_{Diff} = \Delta - \frac{\delta}{3}$. The factor D calculated from equation (2.29) is more commonly calculated using ADC.

$$ADC = \frac{ln(\frac{S_{PGSE}(b_2}{S_{PGSE}(b_1)}}{b_1 - b_2} \tag{2.31}$$

The descriptor "apparent" was added due to the presence of pure diffusion within tissue.

2.3 Perfusion MR imaging

Due to resolution limitations of MRI, direct imaging of microscopic phenomena is not possible. However, macroscopic manifestations of these phenomena can be imaged. The concept of diffusion imaging can be extended to the study of blood flow within the capillary network.

2.3.1 Biological origins

Incoherent motion is believed to arise from the micro-circulation of blood in the capillary network. A model describing this, called intravoxel incoherent motion was introduced in 1986 by Le Bihan et al. to explain the multi-exponential diffusion signal decay observed with acquisition of multiple b-values [66]. The IVIM model describes three parameters: the diffusion coefficient D, pseudo-diffusion or perfusion coefficient, D*, and the perfusion fraction (PF) Its magnitude is described by the volume fraction or PF. D, or D_{slow} describes the tissue water diffusion. D*, or D_{fast} describes perfusion in the tissue and is only visible at low b-values. Imaging of D_{fast} is limited to low b-values because blood flow is at least an order of magnitude greater than the water diffusion coefficient, and signal is very short lived [67]. The IVIM model considers perfusion as a form of incoherent motion, contributing towards the observed diffusion signal attenuation.

2.3.2 Measurement with MR

Measurement of IVIM parameters utilizes multi b-value DW-MRI and the fitting of the diffusion signal with IVIM models. Figure 12 shows that fitting with ADC is unable to account for the multi-exponential diffusion signal decay. This discrepancy between the mono-exponential decay model from equation (2.29) and what is seen in multi b-value imaging is due to the significant contribution of perfusion to the diffusion measurement because of the incoherent motion of blood in the pseudo-random capillary network at the macroscopic level [66, 68, 69, 70, 71].

Multiple studies have shown that the choice of IVIM model, fitting algorithms, and acquired b-values can have a strong impact on the post-processing calculation of IVIM parameters [72, 73, 74, 75, 76, 77].

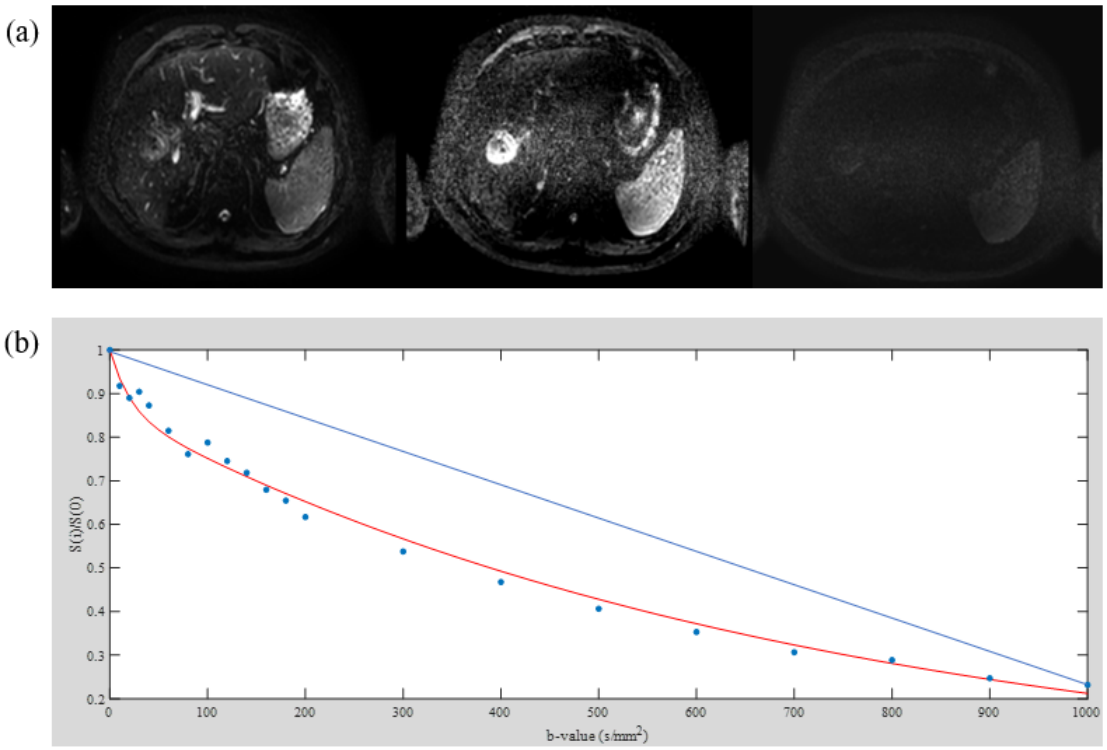

Fig. 12. Multi b-value diffusion-weighted MR imaging. (a) Shows multiple DW-MR images showing a decreased signal as b-value increases. (b) Shows a plot of relative signal intensities, with fit lines for ADC and IVIM calculation methods.

2.3.3 IVIM models

The first IVIM calculation model was proposed by Le Bihan et al in 1986, utilized only three b-values, and did not compute a value for D*. The model requires b-values of 0, 100-300, and greater than 800 s/mm^2 to be acquired [66, 69]. First, ADC is calculated using equation (2.31). The ADC equation is used a second time with the b = 0 image replaced by the b = 100-300 image; this removes the perfusion effects from calculation of the diffusion coefficient. Finally, the perfusion fraction is calculated using equation (2.32).

$$PF = 1 - e^{-b_1 \cdot (ADC - D_{slow})} \tag{2.32}$$

The conventional model was also produced by Le Bihan et al. and allows for calculation of all IVIM parameters using equation (2.33).

$$S(b) = S(0)[(1 - PF)e^{-b \cdot D_{slow}} + PFe^{-b \cdot D_{fast}}] \tag{2.33}$$

Recently, a simplified IVIM model has been studied which requires as few as two nonzero b-values in the regime where pseudodiffusion effects are negligible [78]. This method also only returns D and PF values, and is described by equation (2.34).

$$S(b) = S(0)e^{(-bD_{slow} + ln(1-PF))} \tag{2.34}$$

All of these models allow for calculation on a voxel-by-voxel basis, and creation of diffusion and perfusion quantitative parameter maps.

CHAPTER 3

MR TEXTURE ANALYSIS

Texture is an important property of objects, most commonly linked to the tactile response when touching a surface, but this feature is also present in two-dimensional pictures. Humans perceive objects as being coarse, fine, irregular, or smooth, but struggle in identifying and discriminating between complex textures [79, 80]. Quantitatively, texture can be defined and analyzed using many different methods of calculation [81]. The technique quantifies heterogeneity of a region of interest by analyzing the distribution of pixel gray levels, and their relationship between one another, in the image [82]. Texture analysis (TA) has been used as a means for qualitative and quantitative classification of images at least since the mid-1950's when Kaizer used auto-correlation for the inspection of aerial photographs [83]. Now, TA is used for machine vision in self driving cars, automated inspection for quality control, and in medicine for identification of anatomical and pathological structures.

3.1 First-order textures

First-order texture features are statistics calculated from the original image values, and do not consider pixel neighborhood relationships [84]. The simplest of these is the histogram of intensity levels in all or part of an image. These textures include: mean, standard deviation, entropy, and range. First-order texture analysis is limited in its utility because it provides no information about relative position of pixels to one another.

The mean of the histogram is the mean of the gray-levels in an image

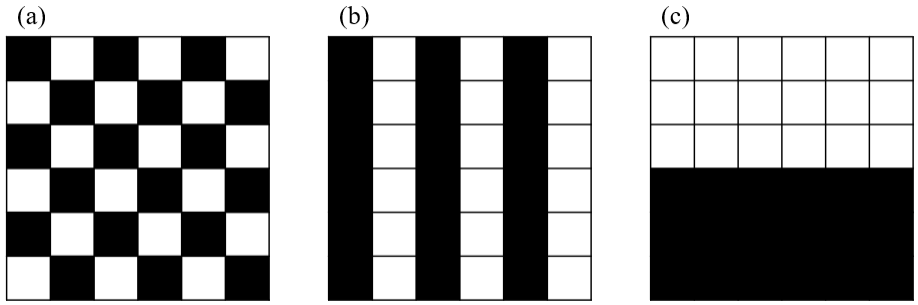

Fig. 13. The utility of first-order texture features is limited because it does not include information about pixel intensity relative to other pixels. These three "images" all have 50% black and 50% white pixels, producing the same gray level histogram.

$$\bar{x} = \frac{1}{n}\sum_{i=1}^{n} x_i \tag{3.1}$$

where x is the pixel gray level, and n is the number of gray levels. Standard deviation is the measure of how far from the mean the gray levels in the image are distributed.

$$s = \sqrt{\frac{1}{n}\sum_{i=1}^{n}(x_i - \bar{x})^2} \tag{3.2}$$

Entropy is the statistical measure of randomness, achieving its largest value when all elements in an image are equal.

$$Entropy = -\sum_{i=1}^{n} I(i) log I(i) \tag{3.3}$$

where I is the image. Range is the minimum and maximum value in a neighborhood of specified height and width around a pixel. This method generates an image where brightness represents texture or boundaries.

(a)

i	j

(b)

1	3	2
3	1	3
2	1	4

(c)

	1	**2**	**3**	**4**
1	0	0	2	1
2	1	0	0	0
3	1	0	0	0
4	0	1	0	0

Fig. 14. An example (a) template, (b) original image, and (c) co-occurrence matrix. The 2 in the co-occurrence matrix indicates that there are two instances of a pixel with gray level 3 immediately to the right of a pixel with gray level 1.

3.2 Second-order textures

Second-order texture features utilize a spatial gray level co-occurrence matrix to consider the relationship among pixels and groups of pixels. Haralick suggested the use of gray level co-occurrence matrices (GLCM), which have become one of the most well known texture features [85]. GLCM illustrate how often each gray level occurs at a pixel located at a fixed geometric position relative to each other pixel, as a function of gray level, shown in Figure 14.

The GLCM can be used to directly measure the texture of an image or region, but may also be converted into simpler scalar measures of texture. In an image where intensity varies gradually, most of the non-zero entries in the GLCM for right neighbors will be near the main diagonal because neighboring pixels will have nearly equal gray levels.

The following equations describe the GLCM-based second order texture features that are used in this dissertation. Homogeneity measures the distribution of elements in the GLCM and their closeness to the GLCM diagonal. A diagonal GLCM will have a high homogeneity index.

$$Homogeneity = \sum_{i,j} \frac{1}{1+|i-j|} G(i,j) \tag{3.4}$$

where G(i,j) is the probability of co-occurrence of the pixel gray-levels. Correlation measures the correlation between a reference pixel to its neighbor over the whole image, describing the joint probability occurrence of the specified pixel pairs. Correlation is 1 or -1 for a perfectly positively or negatively correlated image, respectively.

$$Correlation = -\sum_{i,j} \frac{(i-\mu)(j-\mu)G(i,j)}{\sigma^2} \tag{3.5}$$

where μ and σ are the mean and standard deviation respectively. Energy describes the uniformity of the image, measuring the sum of squared elements of the GLCM. It is also known as the angular second moment feature, and is the inverse of entropy.

$$Energy = -\sum_{i,j} G(i,j)^2 \tag{3.6}$$

Contrast is a measure of the intensity difference between a pixel and its neighbor over the whole image. Contrast is 0 for a constant image, and is also known as variance or inertia

$$Contrast = \sum_{i,j} |i-j|^2 G(i,j) \tag{3.7}$$

CHAPTER 4

DEVELOPMENT OF RESPIRATORY MOTION MANAGEMENT DEVICE

4.1 Current respiratory motion management devices

As previously mentioned, respiratory motion in the thoracoabdominal cavity is a major cause of organ motion and positional uncertainty in radiation therapy, imaging, treatment planning, and treatment delivery. Various methods have been proposed to reduce the positional uncertainty and motion, including: free breathing respiratory gating, breath-hold techniques, abdominal compression, surface monitoring, and real-time target tracking [56, 86, 87, 88, 89, 90]. The addition of the MR environment makes many techniques impractical or impossible, due to the presence of the strong, always on, magnetic field, and sensitivity of image acquisition to outside RF signals. The commonly used active breathing coordinator (ABC) device cannot be used in the MR suite due to the moving metallic parts and commercially available computer system. MR imaging also requires the presence of an RF coil as close to the body surface as possible for good image quality, and the enclosed space of the bore of the magnet to produce a uniform magnetic field. These qualities make other popular respiratory motion monitoring systems impractical. Optical surface tracking using cameras cannot be performed because the patients skin is not visible. Compression using the commercially available plates is not possible due to the confined spaces and no attachment points available on the table. Compression belts are the final form of respiratory motion management (RMM) systems available for use in the MR environment; however, these are simply elastic belts strapped around the patient

and require self-enforced breath holds without guidance. Gating methods using 1D trackers are also available in MR systems, but these are not available on the standard therapy linear accelerator, only specialized models equipped with integrated MRIs.

4.2 RMM device design

The design requirements for the RMM device designed for this dissertation included:

1. A device compatible with all environments in the radiotherapy treatment process, including MRI, CT, and the RT delivery system.
2. Biofeedback to the subject to guide their respiratory pattern.
3. Easy and reproducible setup with an absolute readout value.
4. Usable with limited coaching from treatment team to the patient, and patient comfort during use.

The motion management system consisted of a belt with an interior pocket sewn in to hold an air bladder (Vernier, Beaverton, OR, USA). The air bladder was connected using a Luer Lock set, sealed with glue, to a 25 ft section of PVC tubing. The tubing was connected to a gas pressure sensor (Vernier, Beaverton, OR, USA) placed at the MR room wall next to the RF wave guide pass-through and connected to a power data interface (PDI). The PDI then connected to a computer running the LoggerPro software V3.14 (Vernier Software and Technology, Beaverton, OR, USA). The LoggerPro screen was displayed to the subject using an in-room MR safe SensaVue Display System (Invivo, Gainesville, FL, USA), and the subject wore mirrored glasses so they could see the screen at the foot of the MR bore. A diagram of the device and component locations can be seen in Figure 15, an image of the device can

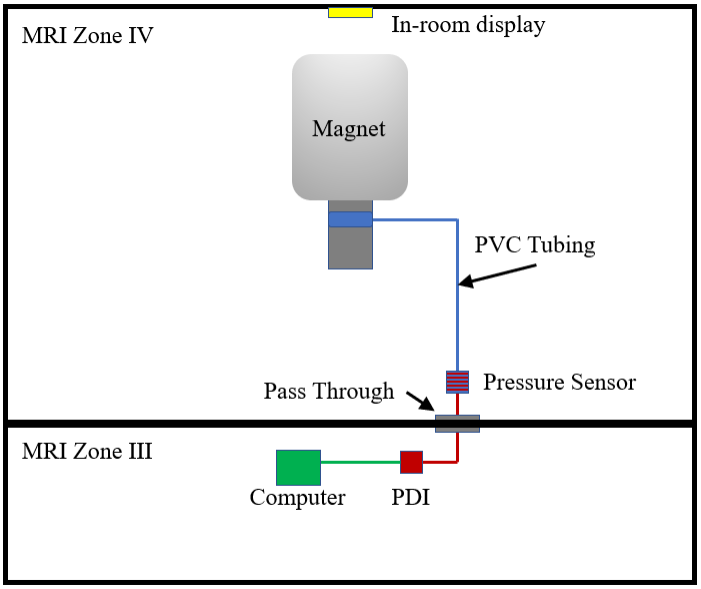

Fig. 15. A diagram of the device setup and placement of components within the MR suite.

be seen in Figure 16, and the device setup on a patient in the MR suite can be seen in Figure 17.

Figure 17 also displays a 110 second respiratory trace that would be visible to the imaging subject while in the MR bore. The red line indicates their real time respiratory trace, and the green and blue lines indicate a pre-positioned bounding box to guide breath holds or respiratory amplitude.

4.3 Image Acquisition

All images were acquired on a 3-T Philips Ingenia MRI (Ingenia; Philips Healthcase, Best, Netherlands). A 30 or 60 second balanced turbo field echo (BTFE) CINE acquisition was performed acquiring 250 frames of a single slice (TR: 2.12 ms; TE: 0.93 ms; Gradient echo train length: 47; Voxel size: 1.87 x 1.87 x 5 mm^3, image matrix: 160 x 160 pixels^2). Initial tests were completed with a set of two investigators.

Fig. 16. A photograph of the final respiratory motion management device, including the belt, pressure sensor, and power-data interface.

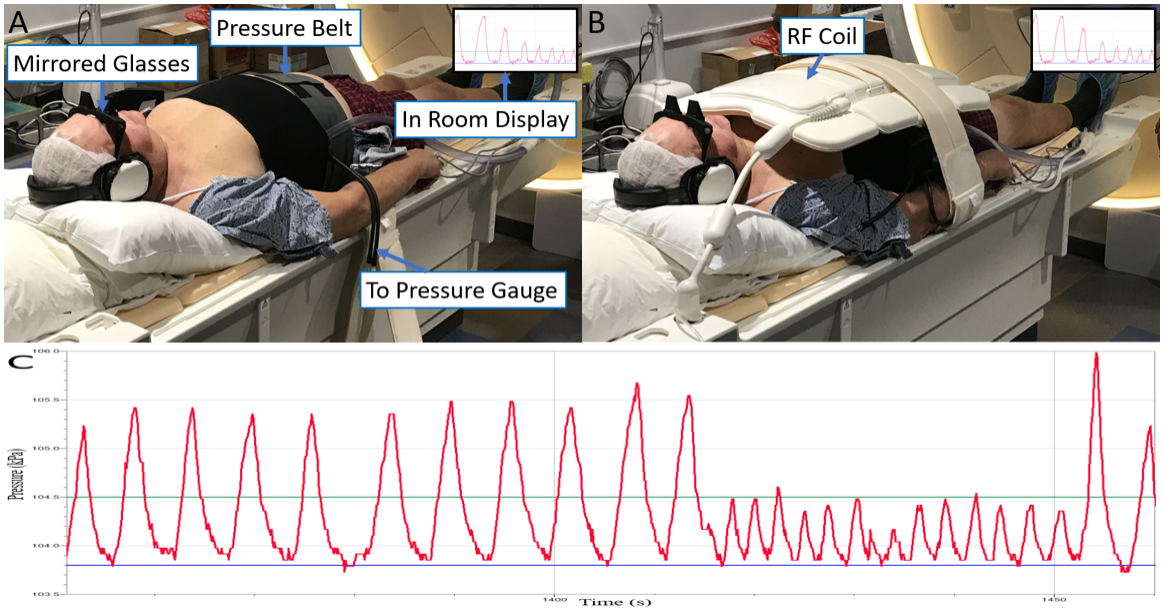

Fig. 17. A photograph of the device setup on a patient without and with the RF coil placed on the patient for imaging. Image C is an example respiratory trace displayed to the patient and operators in real time.

These tests were followed by a cohort of four healthy volunteers, and a second cohort of two liver cancer patients.

4.3.1 Investigator imaging

The two investigators underwent two imaging sessions each, with sessions separated by one week. During each imaging session, the investigators were first positioned on the MRI with the motion management belt around their abdomen, without visual guidance. A CINE MR acquisition was performed acquiring a single sagittal slice through the liver every 120ms for 250 frames, while the investigator was under free-breathing. Visual guidance was then set up for the investigators, allowing them to see their respiratory trace in real time, as well as two horizontal lines indicating a guidance window. Investigators were instructed to keep their respiratory trace between those lines during imaging. CINE MR acquisitions were again performed as described above while the investigator maintained their respiratory trace within a 1.0 kPa large window or a 0.5 kPa small window. The respiratory traces were recorded throughout imaging. Motion was defined as the peak liver dome position at exhale and inhale over the entire CINE acquisition, which has been shown to be a good surrogate for liver tumor motion [44]. Liver dome motion was measured using in-house software developed using MATLAB (MATLAB 2018a, Mathworks, Natick, MA, USA).

4.3.2 Volunteer and patient imaging

Four healthy volunteers with no prior knowledge of the system underwent multiple anatomical and functional image acquisitions while utilizing respiratory motion management including breath hold. Total imaging time was between 30 and 60 minutes, requiring 25 to 30 breath holds. CINE image sets were acquired for volunteers maintaining their respiratory trace as consistently as possible while viewing the trace,

but without a guiding window.

Two liver cancer patients were imaged pre-radiotherapy treatment and post-treatment, also undergoing multiple anatomical and multi-parametric image acquisitions while managing breath motion including breath hold. CINE image sets were acquired for patients under free breathing while being able to view their respiratory traces.

4.4 Trace Comparison

After image acquisition, the CINE images were analyzed to extract the liver dome position using a 10-pixel average of diaphragm position in each frame. Figure 18 shows a montage of ROIs used to extract the liver dome.

Belt traces were converted from pressure to distance using equation (4.1).

$$scaled\,belt\,signal\,[mm] = (\frac{x_{CINE,max} - x_{CINE,min}}{P_{belt,max} - P_{belt,min}}) \cdot (P_{belt} - P_{belt,min}) \tag{4.1}$$

Where x_{CINE} is the diaphragm position from CINE images, and P_{belt} is the pressure reading from the belt system. Normalized error between the scaled belt signal and the CINE liver dome position was calculated using equation (4.2) below.

$$normalized\,error = \frac{1}{A}\frac{\sum x_{CINE,i} - x_{belt,i}}{n} \tag{4.2}$$

Where $x_{CINE,i}$ is the position from CINE acquisition at time point i in mm, $x_{belt,i}$ is the position from the belt respiratory trace at time i in mm, n is the total number of points collected, and A is the amplitude of the respiratory traces from the CINE respiratory trace.

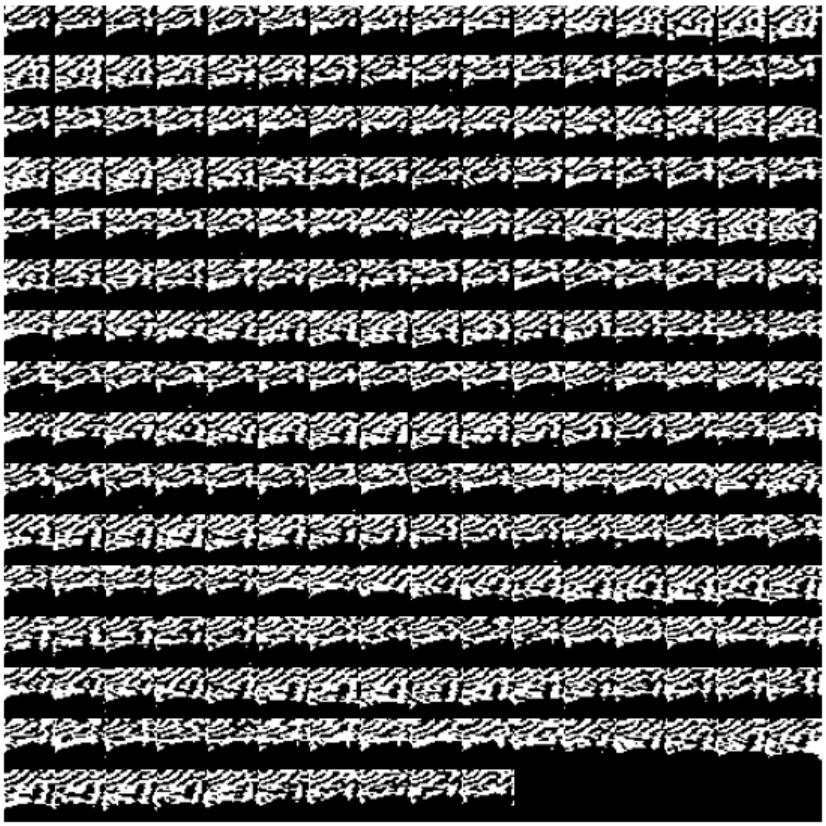

Fig. 18. A set of ROIs from a 250 frame CINE acquisition showing the dome of the liver and lung boundary. An average over ten pixels was used to calculate the position of this boundary in each frame.

4.5 Results

4.5.1 Investigator study

Investigators were able to successfully alter their respiratory traces to the confined windows during image acquisition, reducing the free breathing amplitude, measured using the belt signal, from 1.8kPa to 0.7 kPa, within the window boundary displayed to investigator 1, during the first imaging session. This reduction in amplitude corresponded to a peak to peak change in liver dome motion from 21.6 mm without a guiding box, to 4.3 mm with a guiding box. Table 4 shows the average peak-to-peak motion and standard deviations for CINE images acquired under free-breathing, with a large window guiding box, and a small window guiding box. The respiratory traces for one investigator in free breathing, large window, and small window guidance are shown in Figure 19.

4.5.2 Volunteer and patient study

Volunteers were able to follow the MR technologists instructions for breath hold and guided breathing throughout the imaging session. Figure 20 shows the respiratory traces from the belt signal and CINE acquisitions extracted and overlaid, each respiratory trace also includes five CINE frames from the indicated position in the trace. Table 5 shows the difference between CINE respiratory trace and scaled belt signal for volunteers and patients.

Liver cancer patients were also able to successfully follow the MR technologists instructions for breath hold and guided breathing. Figure 21 shows the respiratory traces from the belt signal and CINE acquisitions extracted and overlaid, with five CINE frames from the indicated position in the trace. In Figure 21G, the patient was instructed to breathe deeply twice before keeping their respiratory signal within

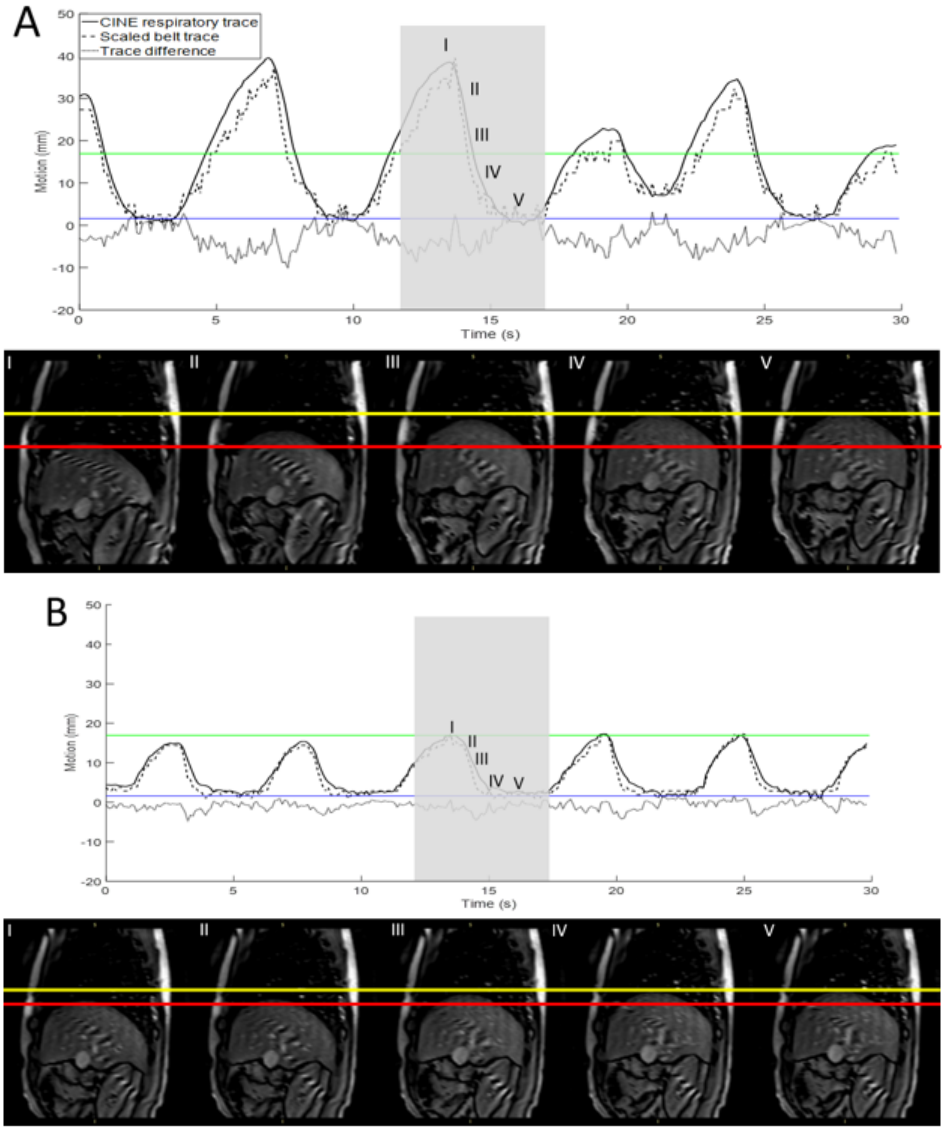
A
CINE respiratory trace
Scaled belt trace
Trace difference
Motion (mm)
Time (s)
I
II
III
IV
V
B
Motion (mm)
Time (s)
I
II
III
IV
V

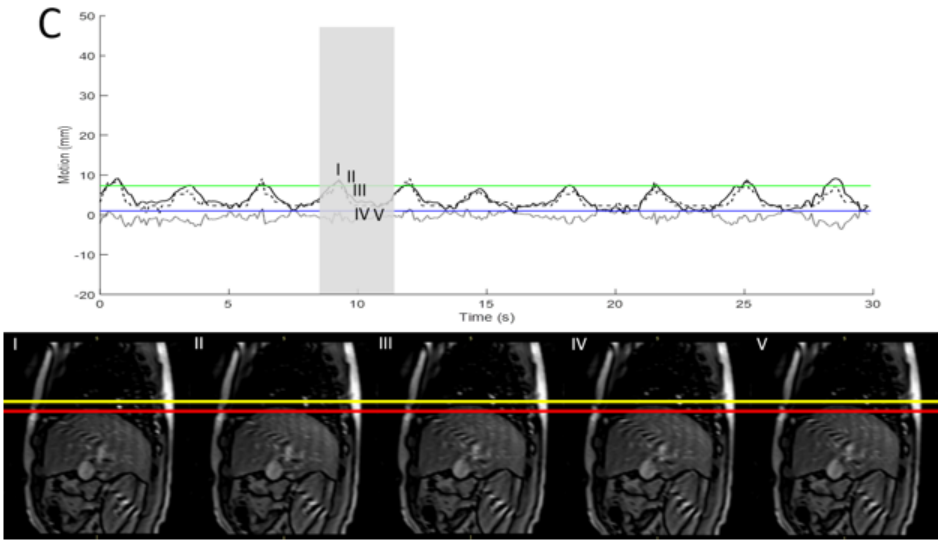

Fig. 19. A-C represent respiratory traces acquired for an investigator with unguided breathing, large window guidance, and small window guidance, respectively. The grey box indicates the respiratory trace corresponding to the CINE images, Roman numerals I-V indicate the image position in the trace, the red and yellow lines indicate minimum and maximum diaphragm position in the boxed trace. The blue and green lines indicate the displayed or desired respiratory boundary for each situation.

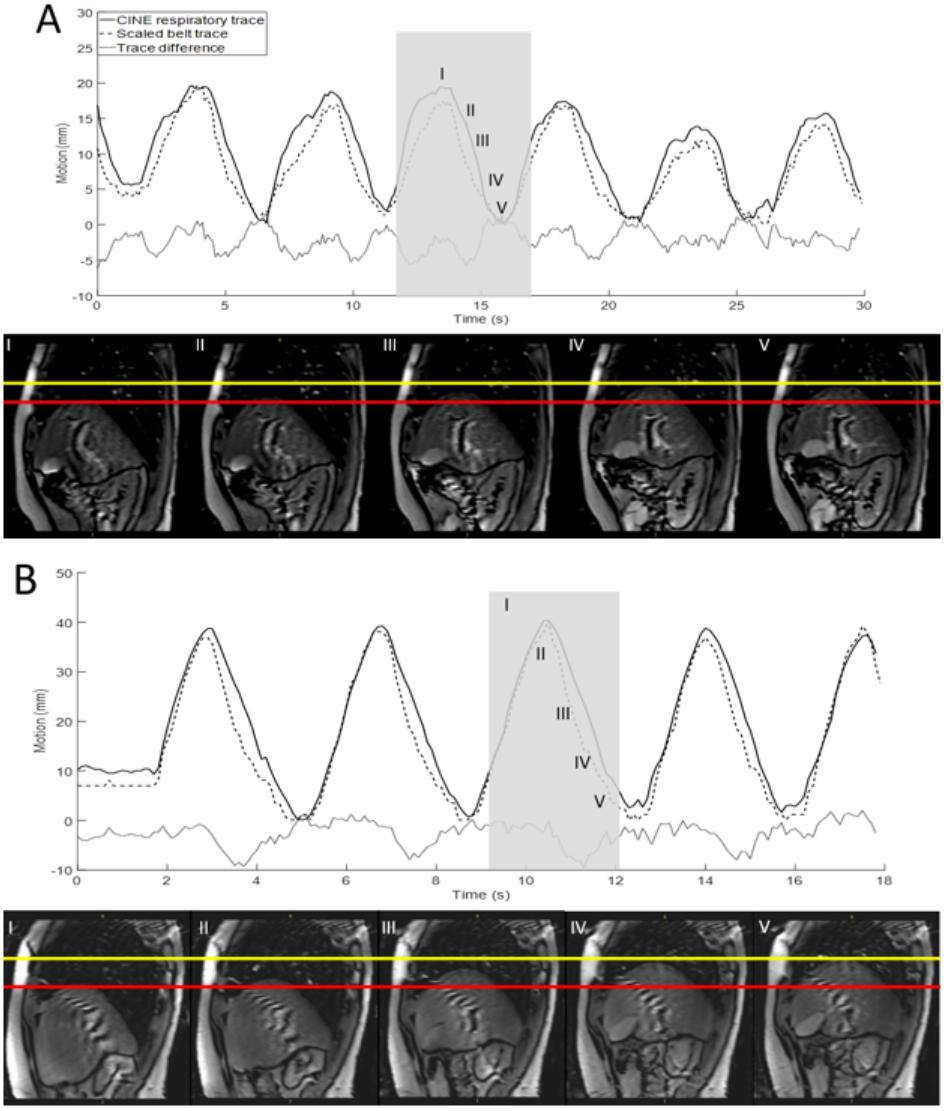
A
CINE respiratory trace
Scaled belt trace
Trace difference
Motion (mm)
Time (s)
I
II
III
IV
V
B
Motion (mm)
Time (s)
I
II
III
IV
V

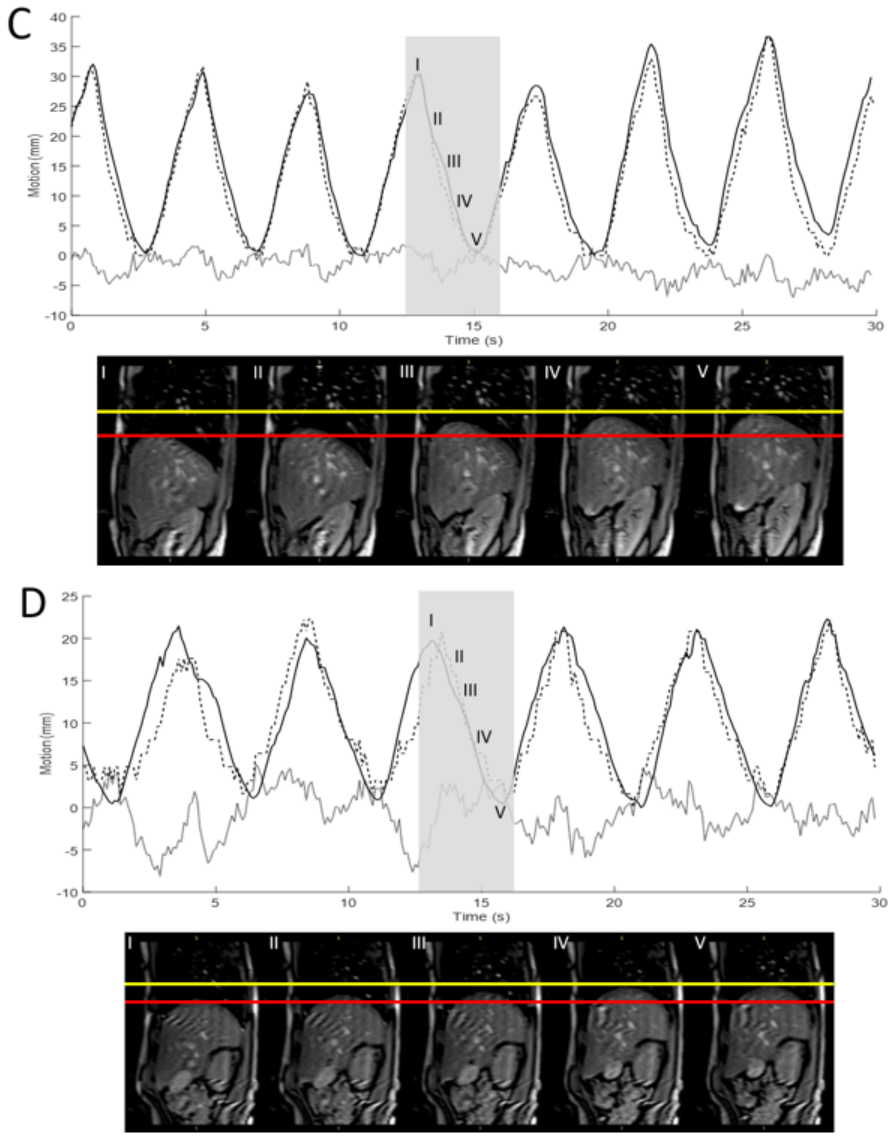

Fig. 20. Respiratory traces from four volunteers (A-D). The solid lines indicate the CINE respiratory trace, the dashed line indicates the belt signal scaled to distance, the dotted line is the difference between the two traces at each time point, and the dot-dash line is the average difference between traces. Roman numerals I-V in each graph are the matched positions to five frames taken from the CINE acquisitions. In CINE image sets, the red and yellow lines indicate the minimum and maximum diaphragm positions respectively.

Respiratory Monitoring	**Guiding Window**	**Peak-to-peak (mm)**	**Std Dev (mm)**	**Minimum inhale position (mm)**	**Maximum inhale position**	**Duty Cycle (%)**
Without Guidance	None	30.6	7.8	21.6	40	47.00
Guided	Large Window	11.5	3.7	7.2	15.6	97.67
Guided	Small Window	5.6	0.9	4.3	6.1	85.33

Table 4. Peak-to-peak motion from CINE images for investigator respiratory traces using three different motion management boundaries displayed by the motion management system with visual biofeedback. The duty cycle represents the percent time the belt signal remained within the boundary window; the window was set to the same scale for large window and without guidance.

a guiding window for the remainder of the image acquisition, which they did successfully. A positional drift can be observed in the respiratory trace for patient 1 pre-RT.

Table 5 shows the motion amplitude, average difference between belt and CINE signal, and the percent normalized error over the CINE acquisition.

4.6 Summary

This study found that SI motion of the liver could be greatly reduced using the proposed respiratory motion management system with visual biofeedback in MR simulation, reducing motion from 30.6mm to 5.6mm on average, over a 30s imaging time period with the investigator group. This 30s time period is longer than the single

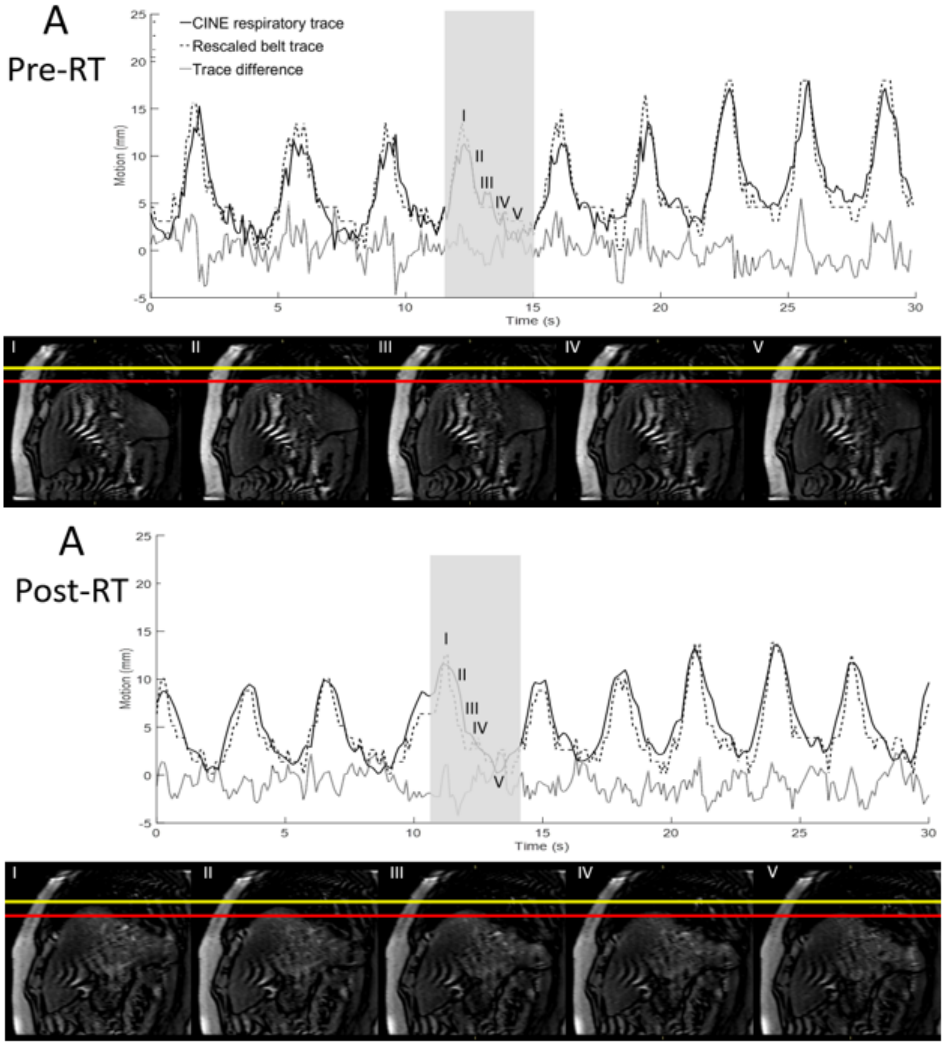
A
Pre-RT
CINE respiratory trace
Rescaled belt trace
Trace difference
Motion (mm)
Time (s)
I
II
III
IV
V
A
Post-RT
Motion (mm)
Time (s)
I
II
III
IV
V

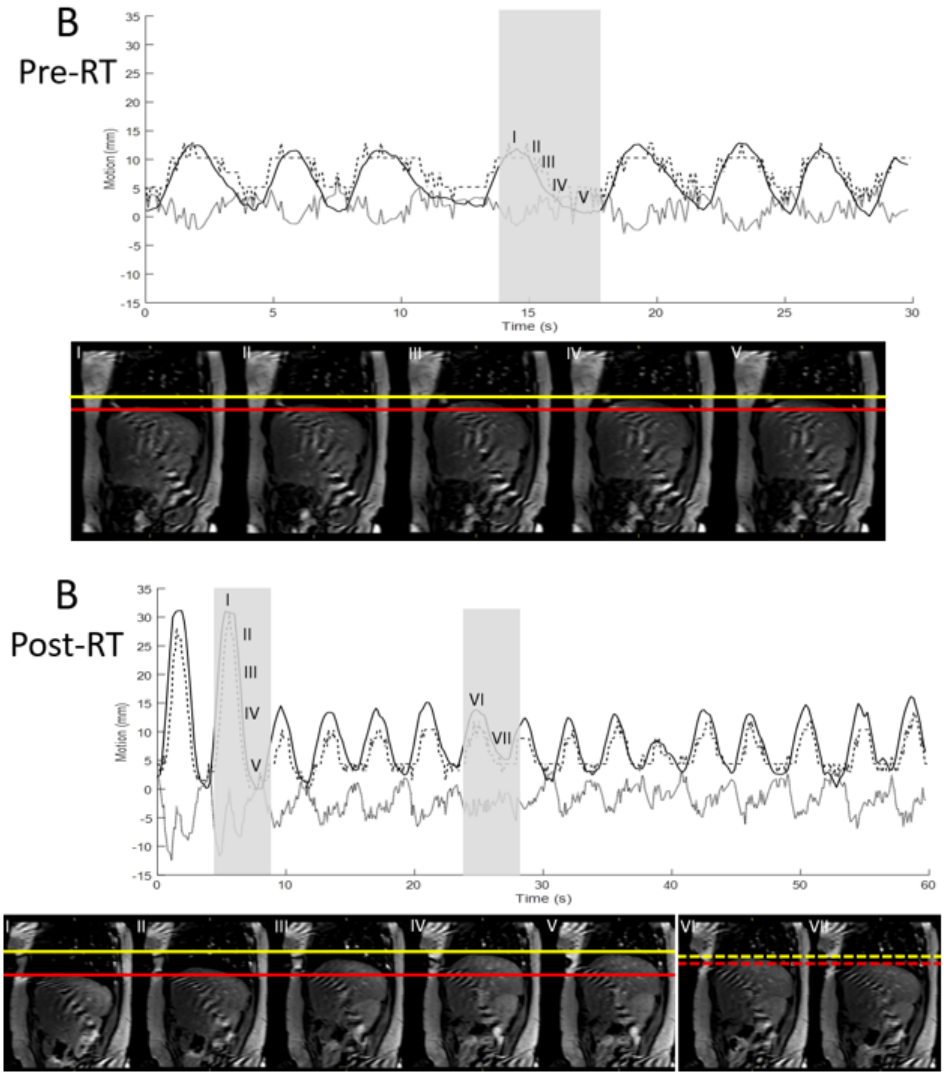

Fig. 21. Respiratory traces from two patients pre- and post- radiotherapy (RT). In image set B-Post-RT, the patient was instructed to breath deeply twice before maintaining their guidance signal within the displayed lines. The solid red and yellow lines indicate the minimum and maximum diaphragm positions. The red and yellow dashed lines indicate diaphragm position inhale and exhale during guided respiration.

Subject	**Motion amplitude (mm)**	**Average difference (mm)**	**Normalized error (%)**
Volunteer 1	19.22	2.31 ± 1.51	12.09
Volunteer 2	40.13	3.49 ± 1.93	8.70
Volunteer 3	30.64	1.82 ± 1.58	5.94
Volunteer 4	22.17	2.30 ± 1.69	10.37
Patient 1 Pre-RT	17.15	1.28 ± 1.07	7.49
Patient 1 Post-RT	16.26	2.18 ± 2.64	13.41
Patient 2 Pre-RT	12.69	2.06 ± 1.32	16.26
Patient 2 Post-RT	32.18	3.21 ± 2.17	9.98
Mean	23.81	2.33 ± 2.33	10.53

Table 5. Comparison of respiratory traces from motion management system and CINE acquisitions for investigators, volunteers, and patients pre- and post-treatment. Motion amplitude is the peak-to-peak motion of the diaphragm from CINE acquisitions. Average difference is the average difference between CINE motion and belt signal. Normalized error is average difference divided by motion amplitude.

breath hold delivery time for most arcs of an SBRT treatment in our clinic, and is more achievable than deep inspiration breath hold for the same amount of time based on volunteer and patient feedback. The volunteers, with no prior knowledge of the device, did not have difficulty maintaining their respiratory traces within the guiding windows and were able to continuously do so for 60s. Patients were also able to maintain consistent breath holds across acquisition time points. In some cases, where windowed guidance was not present, but the subjects could still see their respiratory trace, a drift in position was observed, such as with patient A pre-RT. This may be

because of the patient relaxing or changing their respiratory method over time. Use of a guiding window is able to prevent these changes. The belt was able to track liver dome motion with a simple linear conversion from pressure to distance when compared to CINE images with an average error of 2.3mm. This motion estimation could be improved by using a non-linear pressure conversion, but that was not investigated in this work. Unfortunately, tumor motion was not compared to the pressure data in this study due to poor tumor volume visibility in the CINE acquisitions; this would have allowed a full comparison of the system's ability to use respiratory amplitude as a surrogate for tumor motion.

Implementation of this device within the clinic would require more careful calibration of the device to each patient. This could be achieved by acquiring CINE images under FB to compare motion and pressure amplitudes, and a second acquisition under the desired respiratory motion management technique to assess the amount of motion over BH at different volumes, or during windowed breathing. A demarcation for indexing each patient's belt tightness would be required, but that may change over time due to patient weight loss or other physiological changes and would need to be accounted for. Use of the belt would also require some patient coaching; however, this required limited time during this study. Further, if windowed guidance was the desired method, multiple window sizes could be used depending on the patient's lung function and ability to perform the windowed breathing for the length of treatment delivery. During treatment, this device would provide better duty cycle than breath hold if windowed guidance is used because it removes the recovery and gantry re-positioning time required between BH.

Interfraction respiratory motion variability could be reduced by using a consistent pressure reading at set up and maintaining the same guiding window. In this study the pressure readings were converted to liver motion in mm; however, the device

is not intended for measuring the absolute displacement of objects in the body, or as a tumor position surrogate for target tracking or beam control with real time MR-guided RT. The proposed motion management system can provide continuity of device across pre-treatment imaging platforms including MRI and CT, and treatment delivery due to its lack of high Z material, or ferromagnetic parts. Utilizing the same device throughout the entire treatment process allows for more consistent setup of the patient and respiratory motion. The developed motion management belt is also a candidate for respiratory motion management during MR-LINAC treatments because of its transparency to the treatment beam.

CHAPTER 5

DEVELOPMENT OF IMAGING PROTOCOL

The second aim of this work is to develop a set of MR imaging sequences that provide anatomical and functional information for the liver. The framework of this imaging protocol is built around anatomical imaging, including T1 and T2 weighted images, and DWI, utilizing sufficient b-values for IVIM analysis. This imaging protocol must be acquired in under one hour due to limited MRI availability, with an ideal completion time of 30 minutes. Anatomical images will be used for comparison of conventional and quantitative data. The anatomical images may also be compared to the CTsim and CBCT data sets produced during the current protocol in place for treatment of liver lesions with SBRT at VCU Health. Due to the significant respiratory motion that occurs, these images must be acquired during breath hold. The MR safe visual feedback system developed for aim 1 will be used to provide guidance to the patient for breath holds.

All cohorts were imaged with anatomical images, including T1w turbo field echo (TFE) sequence (Repetition time = 10.0 ms, echo time = 2.3 ms, pixel size = 1 x 1 mm^2, slice thickness = 5 mm; matrix = 268 x 200) and T2w turbo spin echo (TSE) sequence (Repetition time = 1338.8 ms, echo time = 80.0 ms, pixel size = 0.9375 x 0.9375 mm^2, slice thickness = 3 mm; matrix = 376 x 319) image sets (Table 6), a CINE acquisition described in Chapter 4, and a quantitative susceptibility mapping sequence, containing three TE acquisitions. Example images are shown in Figure 22.

Sequence	**TR (ms)**	**TE (ms)**	**NSA**	**Matrix**	**Pixel size (mm^2)**	**T (mm)**	**No. of BH**
T1w TFE	10.0	2.3	1	268x200	1.00x1.00	5	FB
T2w TSE	1338.8	80.0	1	376x319	0.94x0.94	3	4

Table 6. Sequence parameters for anatomical images acquired for all imaging cohorts. TR - repetition time, TE - echo time, NSA - number of signal averages, T - slice thickness, No. of BH - number of breath holds to acquire image.

5.1 Design of IVIM protocols

The IVIM imaging protocols were developed using the investigator and volunteer cohorts. Total acquisition time and the number of breath holds required for completion of the scans were the main concern due to the physical and mental stress which may be caused by the MRI and breath hold conditions, as well as the limited availability of MRI scan time. The next concern for imaging was the number of b-values acquired and the quality of the images. IVIM analysis requires a range of b-values to be acquired, typically from 0-1000 s/mm^2; however, due to the liver having relatively higher perfusion fraction and pseudodiffusion values than other popular IVIM targets such as the brain, the low b-value region becomes more important for generating reproducible values [91, 92, 93, 94, 95, 96]. Multiple IVIM studies in normal liver have used different b-value distributions, resulting in varying IVIM parameter values [91, 92, 94, 97, 98]. For example, Patel et al. used b-values b = (0, 50, 100, 150, 200, 300, 500, 700, and 1000) s/mm^2 and found normal liver values of 32%, $1.2x10^{-3}$, and $40x10^{-3}$ mm^2/s for PF, D, and D* respectively [91]. Luciani et al. used b-values b = (0, 10, 20, 30, 50, 80, 100, 200, 400, and 800) s/mm^2 and obtained values of 26%, $1.2x10^{-3}$, and $85x10^{-3}$ mm^2/s for PF, D, and D* respectively, a D* value twice as

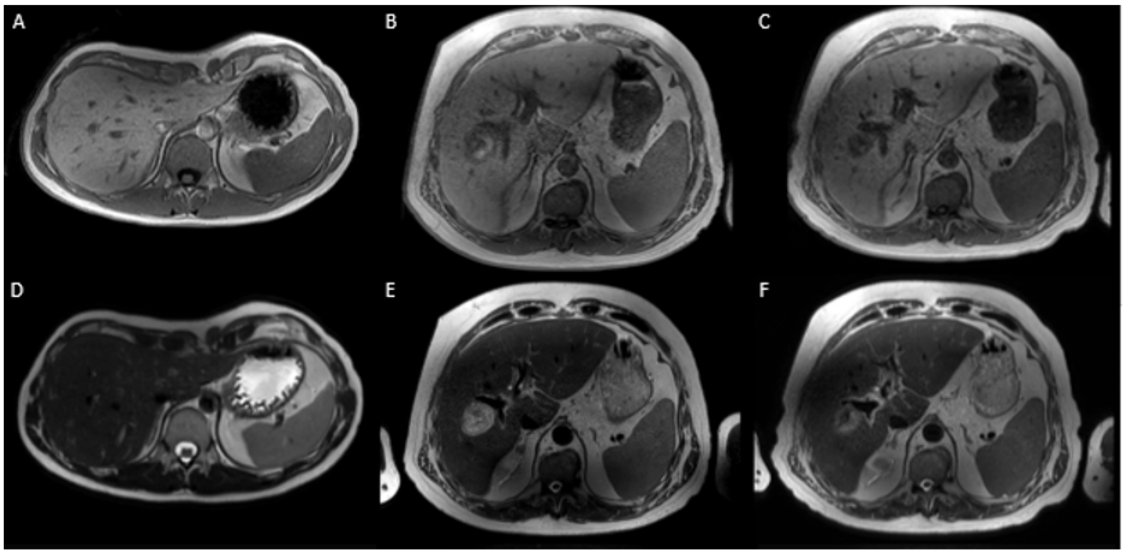

Fig. 22. Images acquired using the designed protocol for T1w (top row) and T2w (bottom row) acquisitions. The left column images are from a healthy volunteer, center column from a pre-treatment cancer patient, and right column from the same cancer patient post-treatment.

high as Patel et al. found [92]. Further, studies have shown that IVIM parameters have poor repeatability for PF and D*, with coefficients of variation ranging from 7.7-25% for PF, and 14.6-59% for D* [91, 99]. b-value distributions are shown in Table 7. Therefore, multiple b-value sets, acquisition types, and signal averages were used to develop the final IVIM imaging set (Table 8).

5.1.1 Investigator cohort

The first cohort to be imaged consisted of two investigators. Two different DW image sets were acquired. The first included 10 b-values b = (0, 10, 30, 60, 100, 150, 200, 400, 600, and 1000) s/mm^2, and required an average of 25 breath holds of 18 seconds, over the course of 20 minutes (Table 8 # 1). The second included 8 b-values b = (0, 20, 40, 80, 100, 300, 600, and 1000) s/mm^2, and required an average of 20 breath holds of 18 seconds, over 17 minutes (Table 8 # 2). Example images from the

Study	Field Strength (T)	**No. of b-values**	**b-values (s/mm^2)**	**NSA**	**RMM method**
Wurnig et al. 2016 [100]	3.0	16	0, 10, 20, 40, 90, 100, 170, 200, 210, 240, 390, 530, 620, 750, 970, 1000	1	FB
Leporq et al. 2015 [101]	3.0	4	0, 10, 80, 800	1	FB
Taimouri et al. 2015 [102]	1.5	7	5, 50, 100, 200, 400, 600, 800	1	FB
Patel et al. 2010 [91]	1.5	9	0, 50, 100, 150, 200, 300, 500, 700, 1000	3	FB
Luciani et al. 2008 [92]	1.5	10	0, 10, 20, 30, 50, 80, 100, 200, 400, 800	3	Gating

Table 7. b-value distributions, respiratory motion management method, and number of signal averages for previous studies. NSA - number of signal averages, RMM - respiratory motion management, FB - free breathing, BH - breath hold.

10 b-value acquisition are shown in Figure 23.

Severe motion artifact can be seen on the anterior surface of the abdomen, as well as the posterior of the liver and the stomach. These acquisitions were performed using inhalation. Significant pressure variation was also observed using the RMM

Study	Field Strength (T)	**No. of b-values**	**b-values (s/mm^2)**	**NSA**	**RMM method**
This work # 1	3.0	10	0, 10, 30, 60, 100, 150, 200, 400, 600, 1000	1	Inhale BH
This work # 2	3.0	8	0, 20, 40, 80, 100, 300, 600, 1000	2	Exhale BH
This work # 3	3.0	14	0, 10, 20, 30, 40, 80, 100, 150, 200, 250, 300, 600, 800, 1000	1	Navigator

Table 8. b-value distributions, respiratory motion management method, and number of signal averages for this study. NSA - number of signal averages, RMM - respiratory motion management, BH - breath hold.

device, with the pressure reading displayed in Figure 24.

Due to the severe motion artifacts, it was decided that all acquisitions would be performed using expiration breath hold. Expiration resulted in a much more steady RMM device signal, shown in Figure 25

5.1.2 Volunteer cohort

The investigator cohort was imaged using multiple acquisition types. DW image sets with 8 b-values b = (0, 20, 40, 80, 100, 300, 600, and 1000) s/mm^2 utilizing the native respiratory trigger, 1D navigator, and breath hold required 10, 5.5, and 15

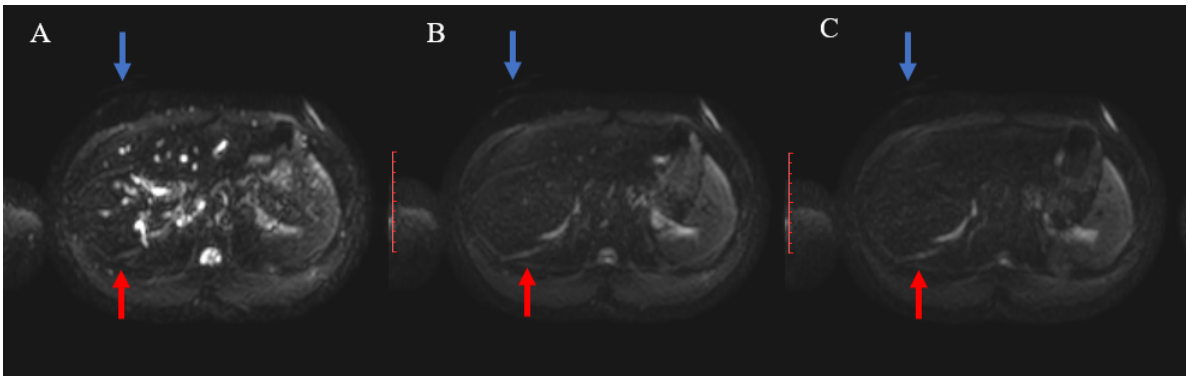

Fig. 23. Images acquired using the 10 b-value image set on a single investigator, showing b-values 0, 10, and 150 s/mm^2, from left to right, acquired during inhalation breath hold. Severe motion artifacts are seen on all images, indicated by blue arrows on the chest wall and red arrows on the posterior surface ghosting artifacts.

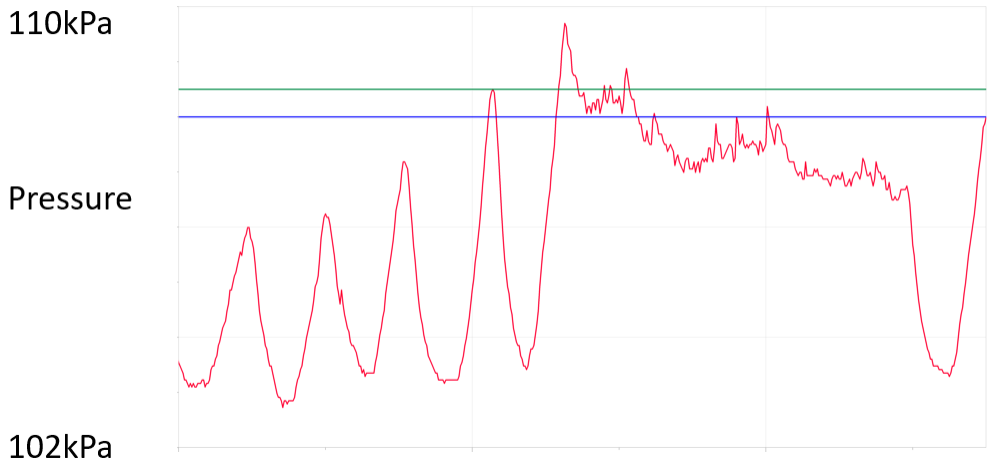

Fig. 24. Respiratory trace and bounding window for an investigator holding deep inspiration breath hold. Even without exhalation, the abdomen falls over time, reducing pressure on the belt and causing motion of the abdominal organs.

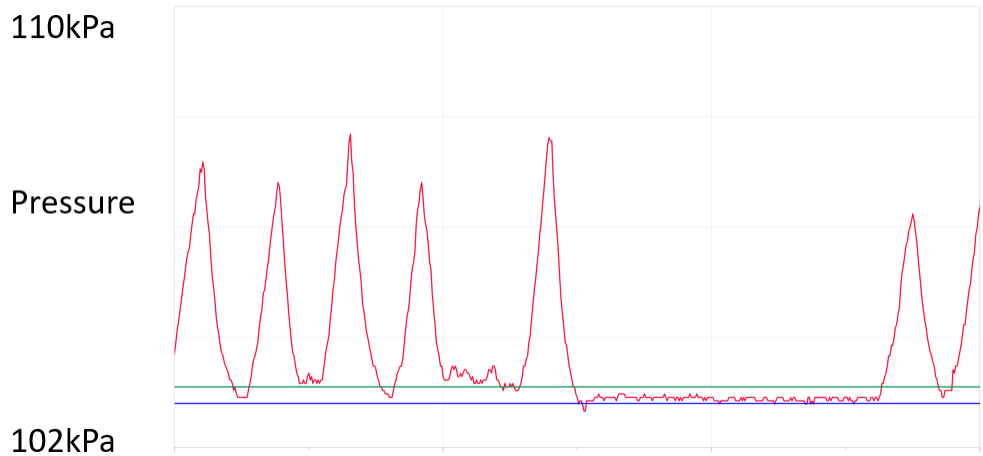

Fig. 25. Respiratory trace and bounding window for an investigator holding full expiration breath hold. Pressure on the abdomen remains considerably more consistent over time.

minutes with 15-20 breath holds of 20 seconds, respectively, and included two signal averages (NSA). Figure 26 shows three DW images from the breath hold acquisition. This was followed by a 14 b-value image set b = (0, 10, 20, 30, 40, 80, 100, 150, 200, 250, 300, 600, 800, and 1000 acquired under free breathing with a navigator, and NSA = 1, requiring 8 minutes to complete (Table 8 # 3). Figure 27 shows three DW images from the free breathing acquisition.

Utilizing the free breathing protocol, images had low signal to noise (SNR) due to NSA = 1, motion blurring near the periphery of the liver, and movement in and out of the imaging plane, causing slices to be mismatched along the SI axis. The images in Figure 28 show three consecutive slices, where the left kidney appears in the frame, is absent, and then re-appears, indicating SI motion in between slice acquisition. The 8 b-value acquisition with NSA = 2 was chosen for imaging with the patient cohort due to the limitations of the free breathing protocol.

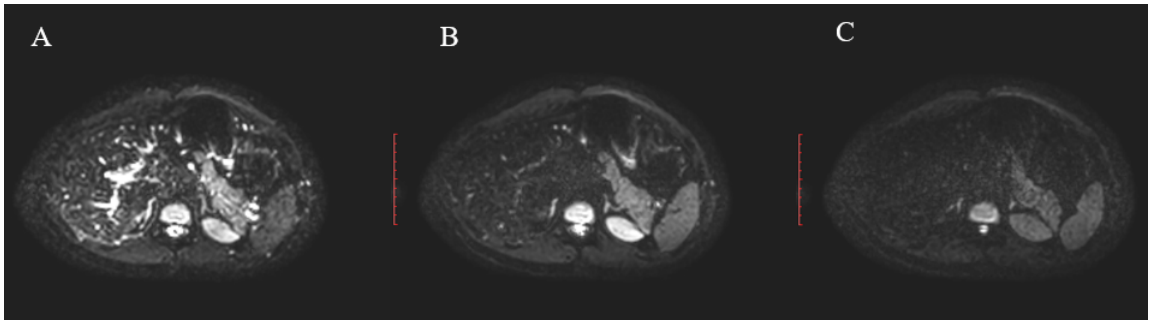

Fig. 26. Three DW images with b = 0 (A), 20 (B), and 300 (C) s/mm^2 for the 8 b-value acquisition under breath hold with NSA = 2. The selected b-values are different from previous figures because the same b-values were not acquired in this image series.

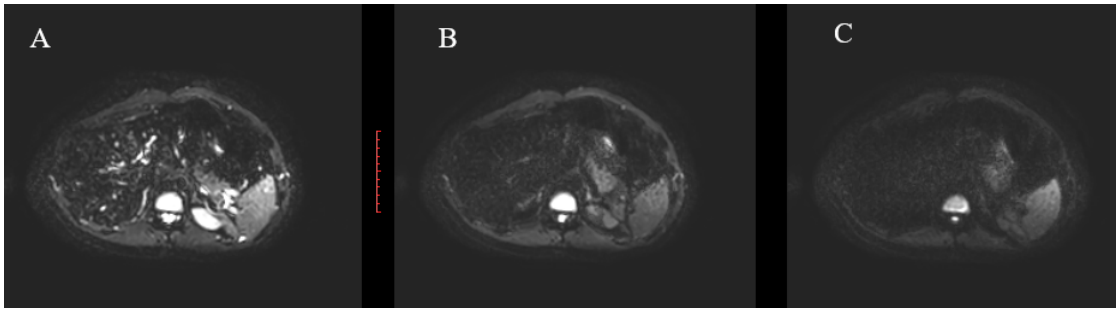

Fig. 27. Three DW images with b = 0 (A), 20 (B), and 300 (C) s/mm^2 for the 14 b-value acquisition under free breathing with NSA = 1.

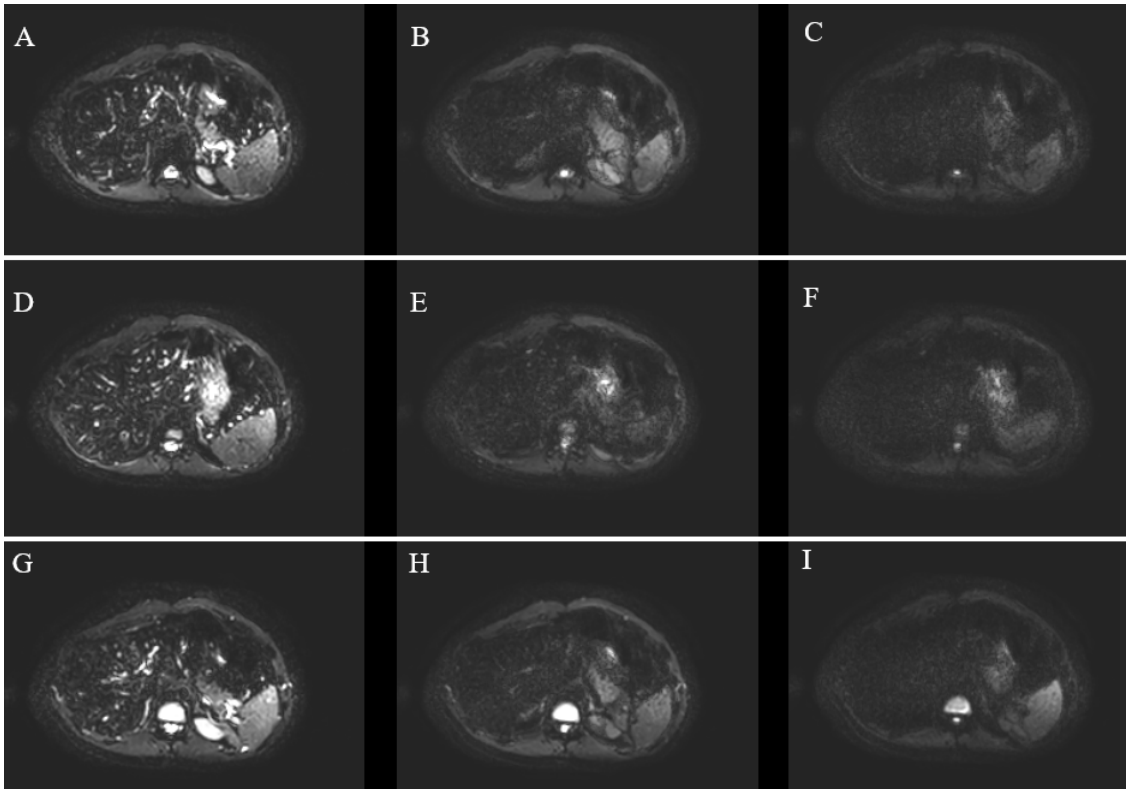

Fig. 28. Three DW images with b = 0 (A, D, G), 20 (B, E, H), and 300 (C, F, I) s/mm^2 for the 14 b-value acquisition under free breathing with NSA = 1 for three consecutive slices.

5.1.3 Patient cohort

The patient cohort was imaged with the 8 b-value DWI protocol, including b = (0, 20, 40, 80, 100, 300, 600, and 1000) s/mm^2, and NSA = 2. The acquisition required 16-22 breath holds, lasting 19-22 seconds each, and totaling 15-18 minutes of acquisition time (Repetition time = 806.1 ms, echo time = 59.3 ms, field of view = 450 mm, slice thickness = 3 mm; matrix = 256 x 256).

5.2 Summary

The final imaging protocol provides high resolution T1w and T2w images with limited motion artifacts and no artifact from the RMM device. The IVIM DWI acquisition was completed within an acceptable amount of time with number and length of breath holds achievable by all volunteers and the two patients in the initial imaging cohort. The total number of breath holds required for full acquisition was 26-34, and required 30-60 minutes from patient laying down on the table to coming off the table. This range in number of breath holds and imaging time was dependent on the number of slices required to gain imaging coverage of the entire liver, and amount of time for the subject to recover after each breath hold. Patients undergoing SBRT of the liver are treated under breath hold and the cancer patients from this study were able to perform the requested breathing pattern in two of three cases, with the third case requiring a small guiding window instead. The current clinical protocol requires approximately 45 minutes to complete, and the duration would be increased with additional DWI acquisitions, however the time required would most likely still be acceptable.

CHAPTER 6

IVIM AND TEXTURE ANALYSIS OF THE LIVER AND LIVER LESIONS

6.1 Introduction

Accurate measurement of normative IVIM parameters for the liver is vital to the translation of IVIM to the clinical environment. Variation occurs due to magnetic field strength, number of b-values, fitting algorithm, respiratory motion, and fitting model [68]. Currently, only a single liver IVIM study other than this work uses breath hold for DWI acquisition. Li et al. found that there was no significant advantage to respiratory triggering versus free breathing for IVIM acquisition when comparing coefficient of variations (CoV) for D, D*, and PF [68]. Multiple studies have been performed to determine the optimal number of b-values to acquire for the best parameter fitting, with the number of b-values acquired reaching as many as 25 [103, 104, 105, 106]. There is no consensus on the correct distribution, but a general rule follows, that the most b-values should be in the range 0 to 100 s/mm^2, fewer in the range of 450 to 800 s/mm^2, and a maximum value of 1,000 s/mm^2 [103]. Table 9 presents a summary of results from published studies for normal liver parenchyma. These studies used various fitting algorithms including asymptotic fitting [91, 92, 100, 101, 102, 105, 107, 108, 109, 110, 111, 112, 113], nonlinear least square fitting [114, 115, 116, 117, 118, 119], and Bayesian fitting [94, 114, 120, 121, 122]. This work has selected least squares fitting with a Levenberg-Marquardt algorithm for fitting. Multiple studies have also suggested that IVIM parameters may be improved using denoising methods, including non-local means (NLM) filtering, local principal com-

ponent analysis (LPCA) and joint rank and edge constraints (JREC) [123, 124, 125, 126].

Result	**D** ($x10^{-3}mm^2/s$)	**D*** ($x10^{-3}mm^2/s$)	**PF** (%)
Median	1.09	70.6	22.40
Range	0.66-1.50	13.60-136.00	5.50-47.07
Mean	1.09	70.02	23.05
SD	0.17	31.01	8.48
CoV	0.16	0.44	0.37

Table 9. A summary of results reported in literature for PF, D, and D* using biexponential fitting.

6.2 Retrospective studies with clinical scans

This section describes a study based on retrospective analysis of consecutive liver SBRT patients treated at our clinic who had pre-treatment and post-treatment DW MRI scans available. Retrospective studies were investigated to determine if the available data was sufficient to apply a simplified IVIM model and if ADC could differentiate normal and diseased tissue, as well as pre- and post-treatment changes.

6.2.1 Images and data processing

The retrospective clinical data set included ten liver cancer patients who had undergone SBRT and received DW MRI scans pre- and post-treatment. All patients had b-values of 50, 400, and 800 s/mm^2, T1w and T2w acquisitions, acquired during respiratory triggering. The images were acquired on a 1.5T MRI (repetition time = 6347 ms, echo time = 79.0 ms, pixel size = 1.82x1.82 mm^2, slice thickness = 6 mm,

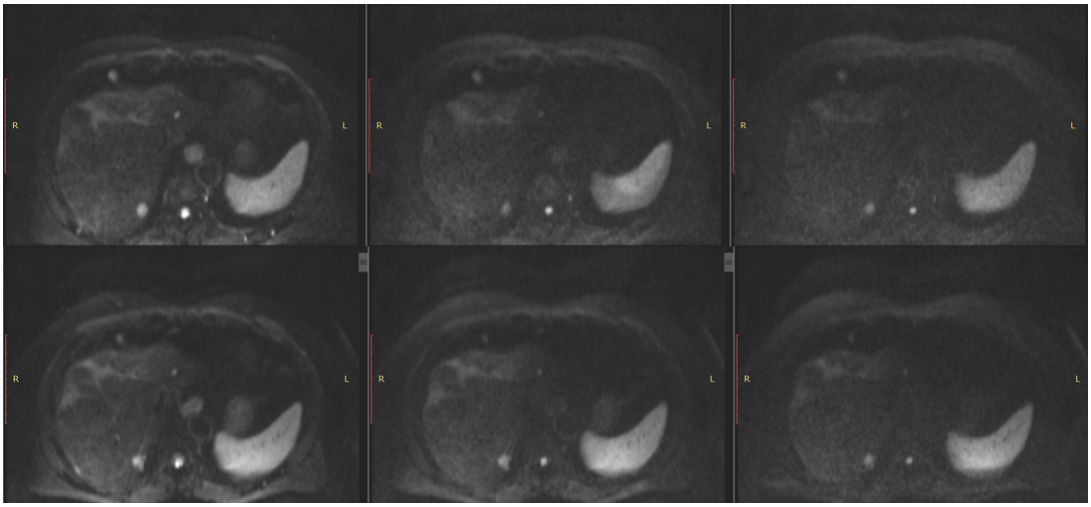

Fig. 29. Three DW images with b = 50, 400, and 800 s/mm^2 acquired for a previously treated patient. The top row shows pre-treatment and the bottom row shows post-treatment images. The hyper-intense region near the posterior wall of the liver shows the position of the tumor in these images.

number of sample averages = 4). An example of pre- and post-treatment DW images can be seen in Figure 29.

Due to only three b-values being imaged in the clinical data, equations (2.32) and (2.34) were used to calculate f and D. ADC values were calculated using b-value images b = 50 and 800 s/mm^2 and b = 50 and 400 s/mm^2.

6.2.2 Results

The Wilcoxon Rank Sum Test was used to compare parameter values acquired from ADC calculation and fitting of DW image values to the LeBihan model. There was a statistically significant difference between healthy tissue pre- and post-treatment, and between diseased tissue pre- and post-treatment for ADC (p = 0.0001, 0.003). There was also a near significant difference between healthy and diseased tissue pre-treatment for ADC (p = 0.081). This indicates that the parameters derived from the LeBihan method were not sufficient to distinguish between healthy and diseased

tissue, or to differentiate treatment changes.

Parameter	**ADC** ($x10^{-3}mm^2/s$)	**D** ($x10^{-3}mm^2/s$)	**f** ($x10^{-3}mm^2/s$)
Normal Tissue Pre.	0.77±0.24	0.60±0.33	0.48±2.72
Normal Tissue Post.	0.88±0.34	0.52±0.34	1.92±4.32
Tumor Pre.	0.62±0.32	0.31±0.30	3.12±5.10
Tumor Post.	0.65±0.60	0.34±0.41	4.10±7.16

Table 10. A summary of mean ± standard deviation for retrospectively sampled patients, with three b-value DWI images, and values calculated using LeBihan's method.

6.2.3 Summary

The absence of statistically significant differences for IVIM parameters calculated using LeBihan's method for diseased and normal tissue in the liver suggests that this method may not be sufficient for IVIM analysis. ADC was also not significantly different between diseased and healthy tissue, indicating that ADC alone may not be sufficient for distinguishing diseased tissue from healthy liver parenchyma. Further, these images were acquired on a different imaging system, with a lower field strength, and without breath hold, than the other images used for this work. The low field strength could increase the amount of noise present in the image, degrading the quality of the calculated IVIM parameters, and respiratory motion could cause further reduction in quality. This section shows the utility of DWI for identifying treatment induced changes in tissue and its limitation for tissue identification when using limited b-values and ADC.

6.3 Volunteer cohort

This section describes the image acquisition, post-processing, analysis, and results for the volunteer cohort study performed in this work. The values obtained from the volunteer cohort also provide a baseline value for healthy liver tissue to compare with diseased livers from the patient cohort.

6.3.1 Images and data processing

The volunteer cohort data set included five volunteers imaged twice, with imaging sessions separated by one week. Images were acquired under expiration breath hold, with guidance from the RMM device developed in Chapter 4. Eight b-value images were acquired, with b = (0, 20, 40, 80, 100, 300, 600, and 1000) s/mm^2 (Repetition time = 806.1 ms, echo time = 59.3 ms, field of view = 450 mm, slice thickness = 3 mm; matrix = 256 x 256).

Before IVIM analysis, images were processed using a custom MATLAB script. DW images were registered for each slice, using a rigid 2D registration, based on mutual information (MI). MI was chosen for the fitting metric because it is not sensitive to extreme contrast changes between images, such as those seen in DW images with low and high b-values. Second, a non-local means filter was applied for denoising. Equation (2.33) was then used for the model, and PF, D, and D* values were generated using a Levenberg-Marquardt algorithm. This generated quantitative maps of all parameters, and ADC maps using b = 0 and 1000 s/mm^2. ROIs were drawn manually in a selection of slices throughout the liver. Poorly fitted data were removed, using the 90th percentile normalized residual as the cutoff point. Texture analysis was then performed for texture described in Chapter 3 using custom built MATLAB code, in the same ROIs as those used for IVIM parameters.

6.3.2 Results

The Wilcoxon Rank Sum Test was used to compare IVIM parameters acquired during the initial and second imaging sessions. There was a statistically significant difference between ADC values for volunteers 1, 2, and 5 (p = 0.0007, 0.0009, <0.0001), and between D values for volunteer 2 (p = 0.0447). No significant difference between first and second imaging session values were found for D* or f in any of the five volunteers. The values for both scans of each volunteer are displayed in Table 11. Figure 30 shows box and whisker plots for IVIM parameters of one volunteer's two imaging sessions, where the blue box indicates the 25th to 75th percentile.

Volunteer	**ADC** ($x10^{-3}mm^2/s$)	**D** ($x10^{-3}mm^2/s$)	**D*** ($x10^{-3}mm^2/s$)	**PF** (%)
V1A	0.95±0.72	0.85±0.30	53.41±31.41	28.24±12.43
V1B	1.06±0.59	0.89±0.26	60.57±34.76	31.28±11.41
V2A	0.76±0.62	0.76±0.19	61.91±31.05	23.67±12.08
V2B	0.90±0.41	0.88±0.22	63.51±30.76	27.11±12.49
V3A	1.33±0.68	0.96±0.29	53.42±33.42	32.06±13.22
V3B	1.17±0.59	0.96±0.29	52.65±32.46	33.75±11.74
V4A	1.18±0.77	0.94±0.29	46.15±33.71	25.91±11.43
V4B	1.39±0.63	1.01±0.30	48.53±30.98	23.24±12.77
V5A	1.17±0.66	0.90±0.18	61.89±21.64	19.27±8.84
V5B	1.39±0.56	0.94±0.31	70.08±38.26	23.28±11.48
Average	0.95±0.59	0.89±0.28	54.45±33.19	28.41±12.53

Table 11. A summary of mean ± standard deviation for all volunteer scans for PF, D, and D* calculated in ROIs, with a total of 1200 voxels for each imaging session.

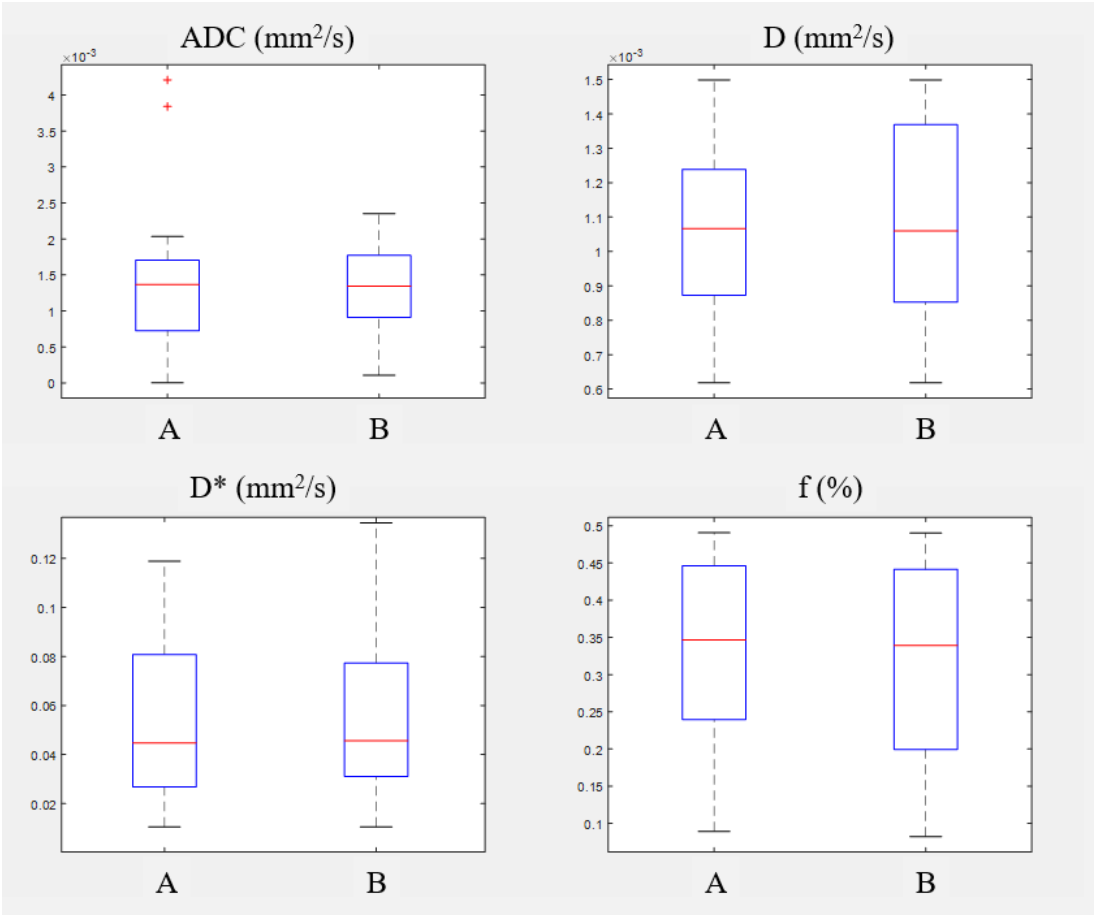

Fig. 30. Box and whisker plot showing the median as the central lines, the 25th to 75th percentiles within the box, and the whiskers extending to the most extreme outlier, for one volunteer, with both first (A) and second (B) imaging sessions.

The texture features for all volunteers in aggregate for b-value 0 images is shown in Table 12. Texture features were extracted from the same ROIs used for IVIM parameter assessment. These values provide a baseline of the statistical variations that were assessed using texture analysis for comparison with values derived from cancer patient images.

Texture Features	**Mean**	**STD**
Entropy	0.179	0.287
Range	11.286	7.681
Standard Deviation	4.001	2.611
Contrast	0.276	0.625
Correlation	0.0174	0.013
Energy	0.989	0.025
Homogeneity	0.995	0.011

Table 12. A summary of mean ± standard deviation for volunteer scans for first- and second-order texture features calculated in ROIs of b0 images, with a total of 1200 voxels for each imaging session.

6.3.3 Summary

The low reproducibility of IVIM parameters experienced in previous works is not seen to a high degree in the volunteer study. It is encouraging that there was not a statistically significant change in IVIM parameters between the first and second scan for volunteers, especially in D* and f parameters, which are more susceptible to noise, organ motion, and imaging parameters. However, relatively large standard deviations

are apparent, and the variation in all parameters across all volunteers is large. This variation may represent an impediment to comparing IVIM parameters across imaging subjects. Separation of parameters by demographics may be necessary to generate a better picture of healthy liver IVIM parameter values. These differences may also be compounded by alcohol or tobacco use, diet, and iron content of the blood. This section has shown the feasibility of IVIM in the liver, with breath hold guided by visual biofeedback.

6.4 Patient cohort

6.4.1 Images and data processing

The patient cohort included two patients, out of five recruited for this study between November 2017 and February 2019. Two patients were ineligible for imaging on a 3T MRI due to the presence of metallic objects within their bodies, and the third was unable to complete the imaging study due to a deterioration in health, leading to in-patient status. Patients were imaged three times, once a week pre-treatment, and twice post-treatment, within one week, and a month after the completion of treatment delivery. Image acquisition parameters are described in Table 13. Each imaging session required 30 to 60 minutes to complete, and 20 to 30 breath holds. Scan length depended on the size of the liver, with larger livers requiring more slices for complete coverage, the patient's ability to perform breath hold, and their recovery time after breath hold.

Image post-processing was performed in the same way as described for the volunteer cohort. Image registration and denoising were performed, prior to non-linear least squares fitting of all b-values to the biexponential IVIM model. After fitting to the IVIM model, ROIs were extracted that corresponded to specific regions of

Sequence	T1W TFE	T2W TSE	IVIM DWI 1	IVIM DWI 2
TR (ms)	10	1338.8	806.1	806.1
TE (ms)	2.3	80.0	59.3	59.3
No. of b-values	NA	NA	5*	4^+
NSA	1	1	2	2
Matrix	268x200	376x319	256x256	256x256
Pixel size (mm^2)	1x1	0.94x0.94	1.76x1.76	1.76x1.76
Slice thickness (mm)	5	3	3	3
No. of BH	FB	4	10	10

Table 13. A summary of MRI sequence parameters used for in vivo liver studies of SBRT patients. NSA: Number of signal averages; *5 b-values: 0, 20, 40, 80, 100 s/mm^2; $^+$4 b-values: 0, 300, 600, 1000 s/mm^2; BH: Breath holds; FB: Free breathing.

accumulated dose from radiotherapy treatment.

6.4.2 Dose Information

Radiotherapy planning included simulation (MRI and 4DCT) to evaluate liver motion and screen patients for eligibility for SBRT, with repeat inhalation breath hold using an Active Breathing Coordinator (Elekta). All treatment planning was performed using the Pinnacle Treatment Planning System on CT imaging with patients treated in inhalation breath hold with a uniform planning target volume (PTV) margin of 5mm. The prescription dose (D_{Rx}), was 50 Gy, in 5 fractions, delivered over two weeks. RT was delivered under daily image guidance on a Varian Truebeam.

Planning CT and DW images were fused by a physician in Radiation Oncology, and dose contours were transferred to the DW images. ROIs were generated for tumor, normal tissue, and at isodose contours of 50 to 80% (I_{25-40}) of D_{Rx} and greater than 95% ($I_{47.5}$) of D_{Rx}

6.4.3 Results

IVIM parameters and texture features were calculated for three ROIs at each imaging time point. IVIM values, as mean ± standard deviation are gathered in Table 14 for each ROI and time point. Tables 15-17 show the IVIM parameter values separated by patient. When tabulated by patient, it is apparent that the changes differed between the two patients, with patient 1 having a decrease in ADC and D, while patient 2 displayed an increase in ADC and D between pre-treatment and post-treatment 1. The tumor volume of patient 2 also experienced a large increase in D* and f between pre-treatment and post-treatment 1 imaging sessions. Color maps for both patients are shown in Figures 31 and 32; the field of view is identical in these image sets, the apparent size difference is due to the difference in tumor location. In patient 1, the lesion is near the center of liver mass, while the tumor is located at the inferior tail of the liver for patient 2.

Comparison of ROI values of the tumor volume showed a significant difference in ADC, D, and f between pre- and post-1 ($p = <0.0001, <0.0001, <0.0001$), as well as for ADC and D for pre- and post-2 ($p = <0.0001, <0.0001$), but not for D* and f ($p = 0.059, 0.102$). Within the dose regions, significant changes were observed for the I_{25-40} pre-treatment and post-1 for ADC ($p <0.0001$), and pre-treatment and post-2 for ADC, D, and f ($p = <0.0001, <0.0001, <0.0001$). For the dose region $I_{47.5}$, pre-treatment and post-1 values were significantly different for ADC, D, D*, and f ($p = <0.0001, <0.0001, 0.011, 0.046$) as well as for pre-treatment and post-2 values (p

ROI	**Time Point**	**ADC** ($x10^{-3}mm^2/s$)	**D** ($x10^{-3}mm^2/s$)	**D*** ($x10^{-3}mm^2/s$)	**PF** (%)
I_{25-40}	Pre	1.35±0.49	1.04±0.54	61.37±59.50	34.73±16.31
	Post-1	1.30±0.55	1.03±0.54	62.95±59.67	33.47±16.48
	Post-2	0.79±0.55	0.66±0.42	62.79±60.92	23.40±18.36
$I_{47.5}$	Pre	1.49±0.49	1.20±0.59	60.93±60.14	33.70±17.54
	Post-1	1.49±0.57	1.20±0.60	67.95±59.66	36.1±15.82
	Post-2	0.86±0.54	0.74±0.45	65.96±61.32	23.91±18.49
Tumor	Pre	1.57±0.50	1.34±0.54	52.47±58.17	27.70±18.41
	Post-1	1.55±0.65	1.3±0.54	70.18±55.06	34.99±14.39
	Post-2	0.98±0.56	0.83±0.49	63.73±60.31	24.69±19.41

Table 14. Mean ± standard deviation for patient scans for PF, D, and D* calculated in ROIs, with a total of 1000 voxels for each ROI. Post-1 indicates the first post-treatment scan, post-2 indicates the second post-treatment scan.

= <0.0001, 0.0002, 0.037, <0.0001).

Texture feature values for the previously described ROIs are shown in Table 18, for b0 DW images. At high b-values, the standard deviation of texture features increased substantially due to the low SNR inherent of these DW images. Texture features showed statistically significant differences between healthy liver and diseased tissue, including standard deviation, correlation, energy, and homogeneity (p = 0.0001, 0.007, 0.0001, <0.0001). Correlation between texture features and IVIM parameters was investigated using the Pearson Correlation Coefficient. However, there was no consistently strong correlation between IVIM parameters and any of the measured texture features across imaging sessions for diseased tissue, patient liver, or volunteer liver.

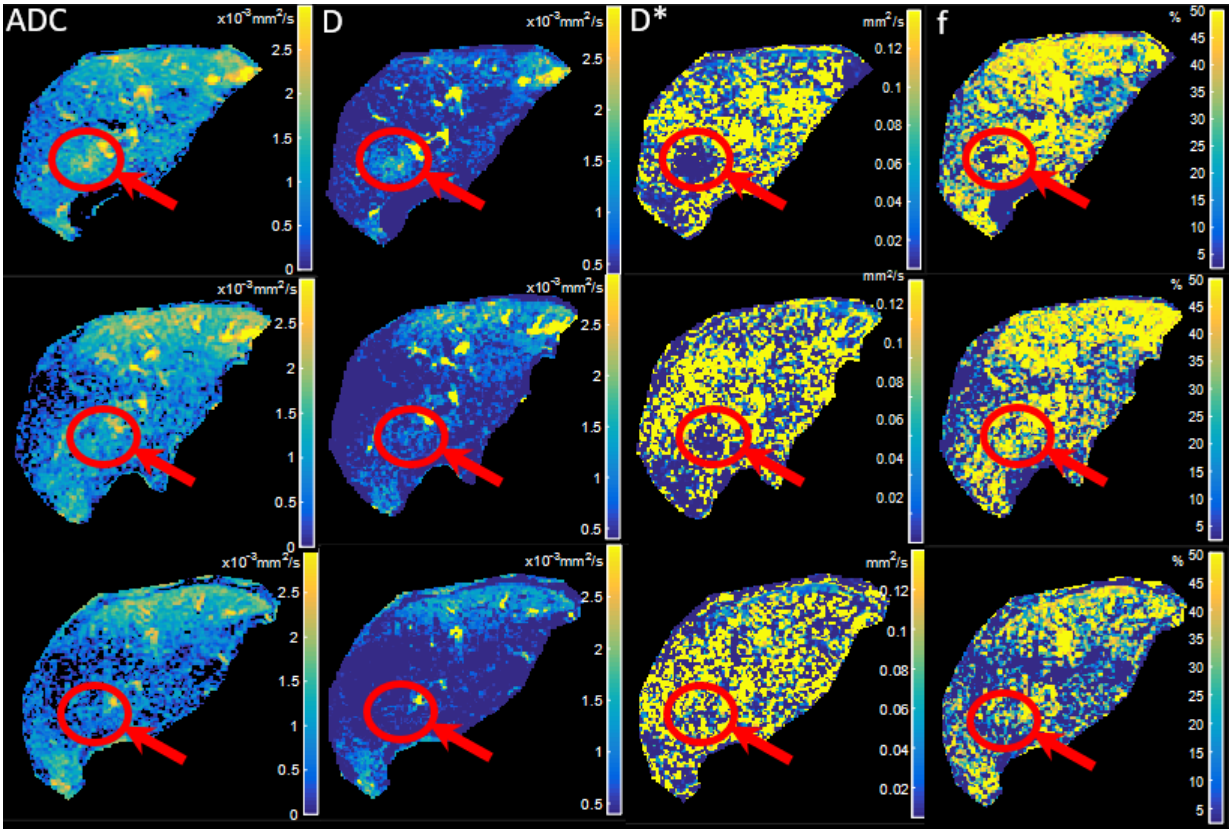

Fig. 31. The top row displays images from a liver cancer patient pre-treatment, the center row from post-1 acquisition, and the bottom row from the post-2 acquisition, with the slice selected from approximately the same location within the liver. The red circle and arrow indicate the tumor position.

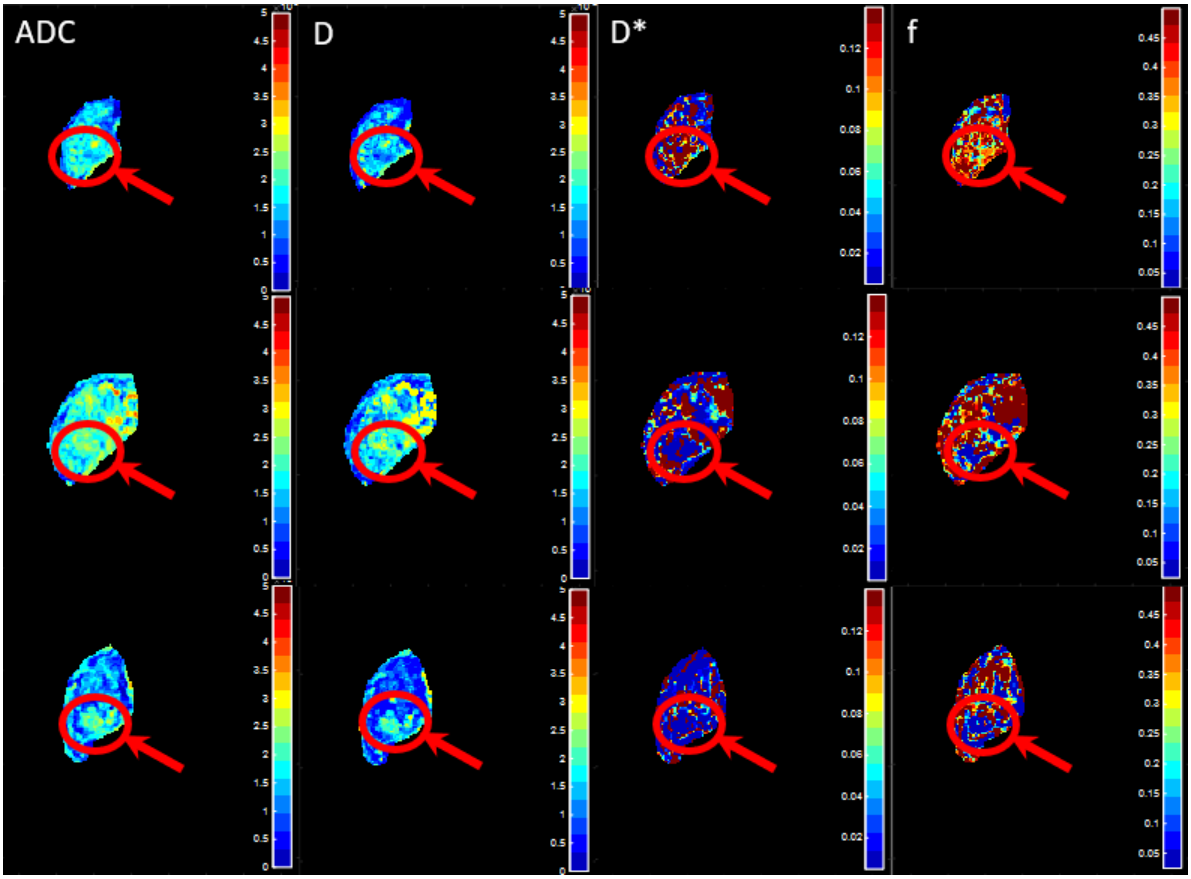

Fig. 32. The top row displays images from a liver cancer patient pre-treatment, the center row from post-1 acquisition, and the bottom row from the post-2 acquisition, with the slice selected from approximately the same location within the liver. The red circle and arrow indicate the tumor position.

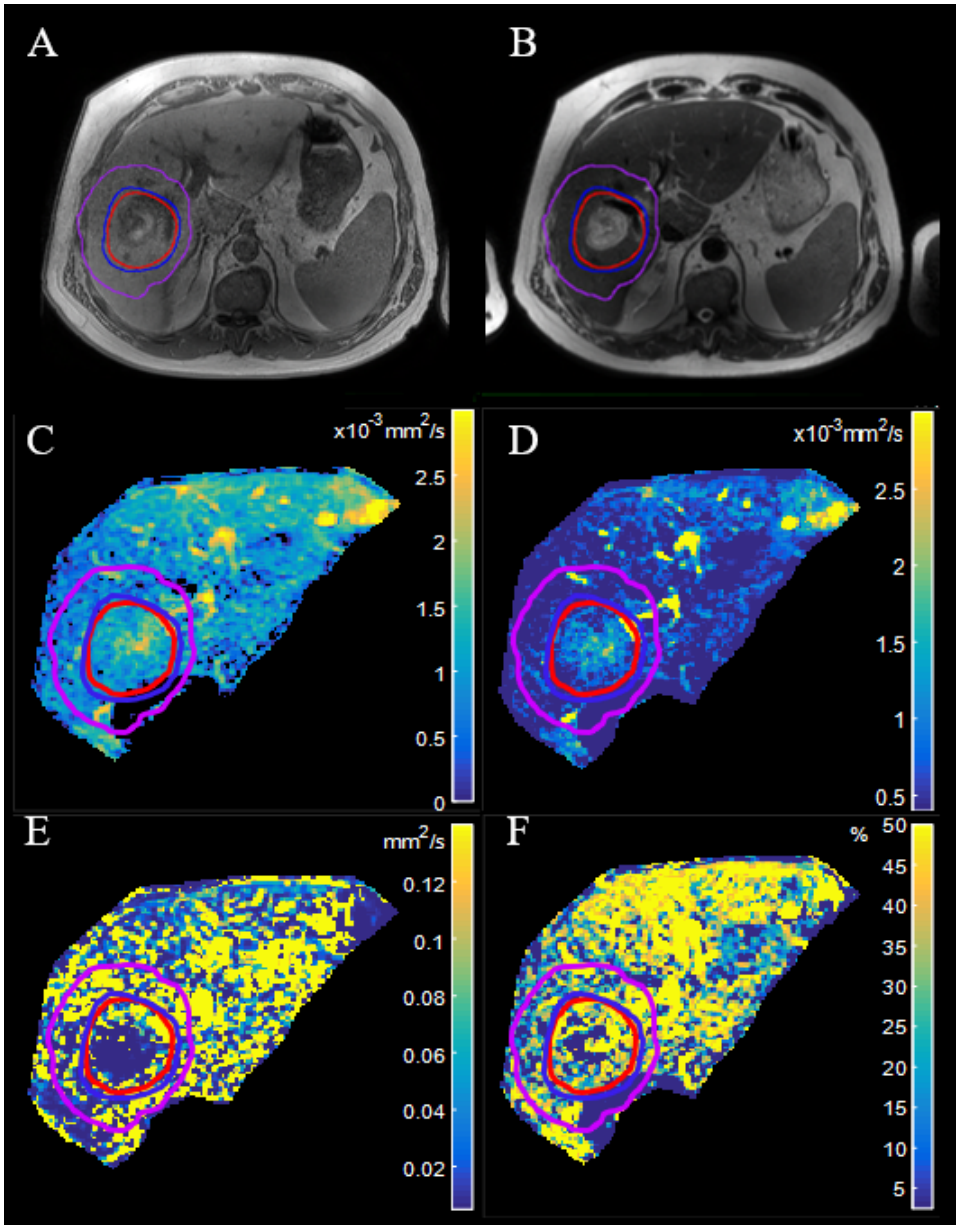

Fig. 33. Pre-treatment T1w (A) and T2w (B) images, and ADC (C), D (D), D* (E), and f (F) parameter maps for patient 1, with registered isodose lines shown for 47.5 Gy (red), 40 Gy (blue), and 25 Gy (purple).

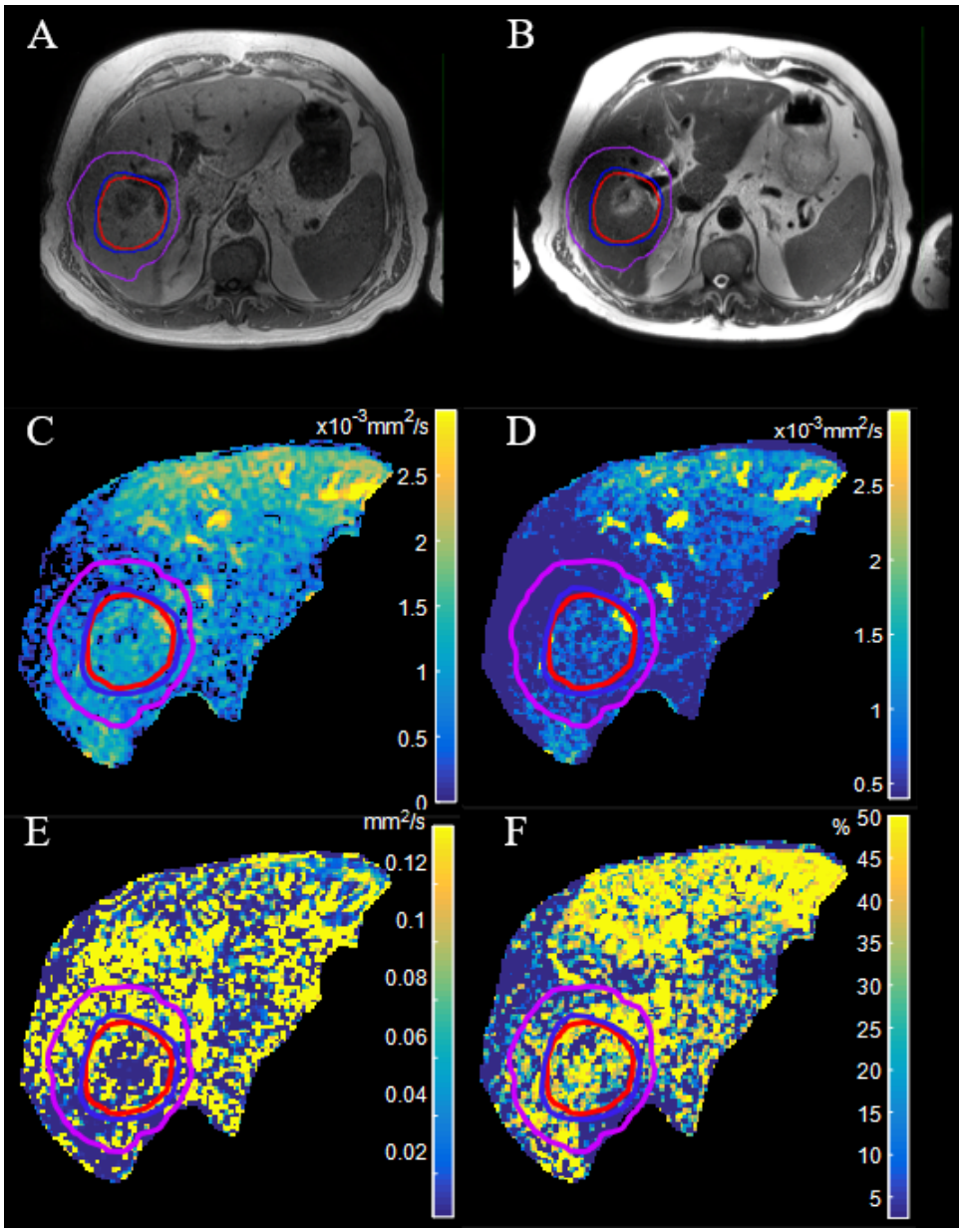

Fig. 34. Post-treatment 1 T1w (A) and T2w (B) images, and ADC (C), D (D), D* (E), and f (F) parameter maps for patient 1, with registered isodose lines shown for 47.5 Gy (red), 40 Gy (blue), and 25 Gy (purple).

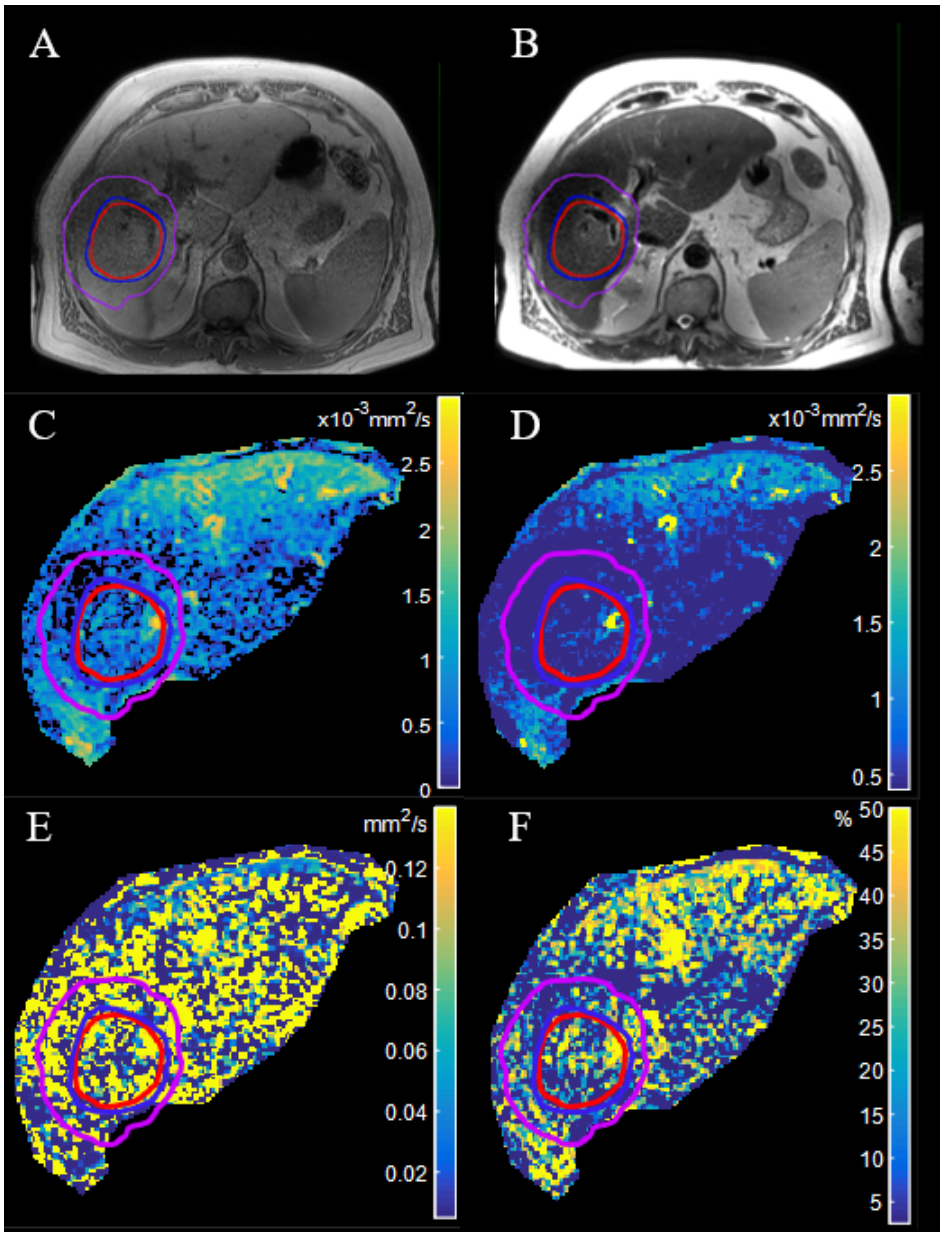

Fig. 35. Post-treatment 2 T1w (A) and T2w (B) images, and ADC (C), D (D), D* (E), and f (F) parameter maps for patient 1, with registered isodose lines shown for 47.5 Gy (red), 40 Gy (blue), and 25 Gy (purple).

Pre						
	I_{25-40}		$I_{47.5}$		Tumor	
	P1	P2	P1	P2	P1	P2
ADC ($x10^{-3}mm^2/s$)	1.01 ± 0.47	1.69 ± 0.51	1.17 ± 0.44	1.95 ± 0.62	1.19 ± 0.38	1.95 ± 0.62
D ($x10^{-3}mm^2/s$)	0.73 ± 0.44	1.35 ± 0.63	0.89 ± 0.51	1.52 ± 0.67	0.98 ± 0.40	1.71 ± 0.68
D* ($x10^{-3}mm^2/s$)	63.98 ± 60.55	58.75 ± 58.45	59.96 ± 60.86	61.89 ± 59.42	40.26 ± 55.44	64.69 ± 60.90
f (%)	30.15 ± 17.37	39.32 ± 15.25	29.74 ± 18.09	37.67 ± 16.99	20.46 ± 17.87	34.94 ± 18.95

Table 15. Mean ± standard deviation for pre-treatment patient scans for PF, D, and D* calculated in ROIs, with a total of 1000 voxels for each ROI.

Texture features were significantly different between healthy tissue and diseased tissue pre-treatment, for entropy, standard deviation, correlation, energy, and homogeneity (p = 0.0001, 0.0001, 0.007, 0.0001, and <0.0001). When comparing pre- and post-treatment disease, contrast, correlation, energy, and homogeneity all showed statistically significant differences (p = <0.0001, <0.0001, 0.0001, 0.0001).

6.5 Summary

These results indicate that IVIM is sensitive to diffusion and perfusion changes in the liver, which occur due to dose deposition during SBRT. Further, this work found significant changes in texture features in the liver and tumor pre- and post-SBRT. This demonstrates the utility of IVIM and texture analysis for observing post-treatment changes in liver cancer, as well as in surrounding healthy tissue that receives

Post-1						
	I_{25-40}		$I_{47.5}$		Tumor	
	P1	P2	P1	P2	P1	P2
ADC ($x10^{-3}mm^2/s$)	0.83 ± 0.52	1.78 ± 0.58	0.97 ± 0.45	2.02 ± 0.69	0.83 ± 0.39	2.27 ± 0.91
D ($x10^{-3}mm^2/s$)	0.63 ± 0.41	1.43 ± 0.67	0.68 ± 0.43	1.71 ± 0.78	0.60 ± 0.24	1.99 ± 0.95
D* ($x10^{-3}mm^2/s$)	66.62 ± 60.49	59.28 ± 58.85	62.40 ± 59.45	73.49 ± 59.87	41.43 ± 53.97	98.92 ± 56.16
f (%)	26.60 ± 18.37	40.33 ± 14.60	30.67 ± 17.42	41.64 ± 14.22	24.02 ± 17.85	45.97 ± 10.92

Table 16. Mean ± standard deviation for the first post-treatment patient scans for PF, D, and D* calculated in ROIs, with a total of 1000 voxels for each ROI.

dose due to imperfect dose conformity.

In this study, values of D* and f had standard deviations greater than half their mean. This indicates that their values have large variations, especially within the inhomogeneous tumor volumes. Further analysis showed that ADC had statistically significant differences between more tissue types and treatment time points than IVIM-derived parameters. Across all parameters, ADC had the greatest ability to distinguish analysis groups, while D* had the worst performance. These findings are contrary to what is expected from IVIM theory, which allows for molecular diffusion and blood perfusion to be distinguished, compared to ADC measurement where these two parameters are combined. Previous studies have attempted to use IVIM as a diagnostic tool for liver lesion characterization. Yoon et al. and Penner et al. found that IVIM parameters performed better than ADC and D values for characterizing

Post-2						
	I_{25-40}		$I_{47.5}$		Tumor	
	P1	P2	P1	P2	P1	P2
ADC ($x10^{-3}mm^2/s$)	0.56 ± 0.49	1.04 ± 0.60	0.47 ± 0.52	1.26 ± 0.57	0.56 ± 0.52	1.41 ± 0.60
D ($x10^{-3}mm^2/s$)	0.50 ± 0.29	0.83 ± 0.54	0.48 ± 0.29	0.99 ± 0.60	0.51 ± 0.33	1.15 ± 0.66
D* ($x10^{-3}mm^2/s$)	68.86 ± 61.68	56.72 ± 60.16	73.61 ± 62.59	58.31 ± 60.05	75.33 ± 62.72	52.13 ± 57.90
f (%)	19.21 ± 17.19	27.59 ± 19.53	18.17 ± 17.41	29.66 ± 19.56	20.49 ± 18.24	28.90 ± 20.59

Table 17. Mean ± standard deviation for the second post-treatment patient scans for PF, D, and D* calculated in ROIs, with a total of 1000 voxels for each ROI.

liver lesions[127, 128]. In contrast, Colagrande et al. and Zhu et al. found that ADC and D values had the better chance of characterizing liver lesions [129, 115]. This work found that ADC and D values had a greater probability for correctly characterizing liver lesions, while f did not have a significant difference between tumor and healthy tissue. These discrepancies highlight the difficulty of producing repeatable IVIM parameter maps and validation of results across centers.

As mentioned previously, multiple factors can influence the calculated values, depending on factors related to anatomy, imaging, and analysis methodology. A study by Fan et al. showed that HCC tumor size had a major impact on tissue structure, with tumors larger than 3cm in diameter being poorly differentiated, and having more necrosis and liquefaction of tissue than those smaller than 3cm [130]. Fan et al. also reported that highly differentiated tumors receive their blood supply from multiple

	I_{25-40}		$I_{47.5}$		Tumor	
	Pre	Post-1	Pre	Post-1	Pre	Post-1
Entropy	2.74 ± 0.36	49.51 ± 69.85	1.39 ± 1.62	131.04 ± 182.82	1.78 ± 1.81	48.10 ± 67.39
Standard Deviation	1.01 ± 0.02	16.86 ± 23.77	0.52 ± 0.63	52.39 ± 73.24	0.61 ± 0.63	15.37 ± 21.54
Contrast	0.47 ± 0.33	0.25 ± 0.02	0.39 ± 0.27	0.22 ± 0.04	0.24 ± 0.17	0.11 ± 0.01
Energy	0.19 ± 0.01	0.18 ± 0.01	0.16 ± 0.01	0.16 ± 0.02	0.09 ± 0.01	0.09 ± 0.01
Homogeneity	0.37 ± 0.01	0.35 ± 0.02	0.32 ± 0.01	0.31 ± 0.03	0.19 ± 0.01	0.17 ± 0.02

Table 18. Mean ± standard deviation for texture features calculated for the specified ROIs.

sources, while less differentiated tumors receive blood mainly from the hepatic artery. In addition to this, Yin et al. presented that location has a significant effect on the blood supply [131]. Classification by blood supply location may reduce the fluctuation of D* and f values. The choice of b-values can significantly impact IVIM parameters, with multiple studies performed attempting to determine the optimal b-value distribution which would lead to reduced errors in IVIM parameter calculation [72, 73, 91, 103, 104, 105, 121, 132, 133, 134]. Optimization of acquisition protocol and post-processing algorithms may also minimize errors in parameter estimation, and are required for a robust clinical application [74, 99, 112, 135, 136].

CHAPTER 7

DEVELOPMENT OF AN IVIM AND TEXTURE ANALYSIS TOOLBOX

This Chapter describes a GUI, controlling a set of scripts and functions, developed in MATLAB for streamlining the calculation of IVIM parameters and texture features.

7.1 Toolbox program

The toolbox program developed for this work incorporates multiple modules, and is compatible with input data of multiple types. A screen capture of the GUI used for this program is shown in Figure 36. The first set of radial buttons allows the user to select the number of folders that contain the DW image set that is set to be analyzed, and will prompt the user to select the enclosing folder(s) when executed. The single folder option will read in all images, and their associated b-values and slice position. Slices are then sorted by b-value and slice position into a 4D matrix. The two folder option reads image files in from two enclosing folders; this was added because IVIM image sets were acquired in two separate protocols in this work. The images are again sorted by b-value and slice location, and duplicate b-value images for the same slice position are averaged. The resultant 4D matrix is then passed to the next selected option. Users have the option to define their calculation volume, using either "No ROI", "Load ROI from .mat file" and "Draw custom ROI." The "No ROI" option will perform the selected calculations on the entire image volume, and may require a significant amount of computation time. If "Load ROI from .mat file" is selected, the program prompts the user to select a binary .mat file of the same size

as the image volume to constrain the calculation volume. The "Draw custom ROI" option will prompt the user to draw custom ROIs on each slice of the image volume using an ROI tool in MATLAB. The third set of radial buttons allows for image denoising to be selected. The program removes intensity outliers greater than 10 times the mean tissue value, and uses a non-local means filtering algorithm described by Buades et al [137]. The "Perform Texture Analysis" check box selects for texture analysis values and maps to be calculated within the desired calculation volume, and includes the texture features described in Chapter 3. The "Perform ADC calculation" check box selects for calculation of ADC in the designated calculation volume. ADC calculation uses equation (2.31), and selects the minimum and maximum b-value images. The fourth radial button selection, "Perform image registration" designates if registration should be performed. The program utilizes a mutual information based rigid registration algorithm. Mutual information was chosen for its performance with DW images, where contrast varies significantly between moving and fixed images, but the structure remains constant. The images associated with the lowest b-value are used as the fixed images, and the remaining b-value images at each slice location are designated as the moving images. The final radial button box allows the user to select what model to use for calculation of IVIM parameters. The mono-exponential method uses Equation (2.34), requires at least two b-values, and does not provide D* maps. The LeBihan method uses Equation (2.32), requires at least three b-values, and does not provide D* maps. The bi-exponential method uses Equation (2.33), requires at least three b-values, and provides D, D*, and f values. However, the bi-exponential method is significantly more computationally expensive than the other options. Once the operator has selected their desired options, they click "Done" and will be prompted to select their desired input folders and files before the program will continue. The toolbox was tested with three different data sets, of different

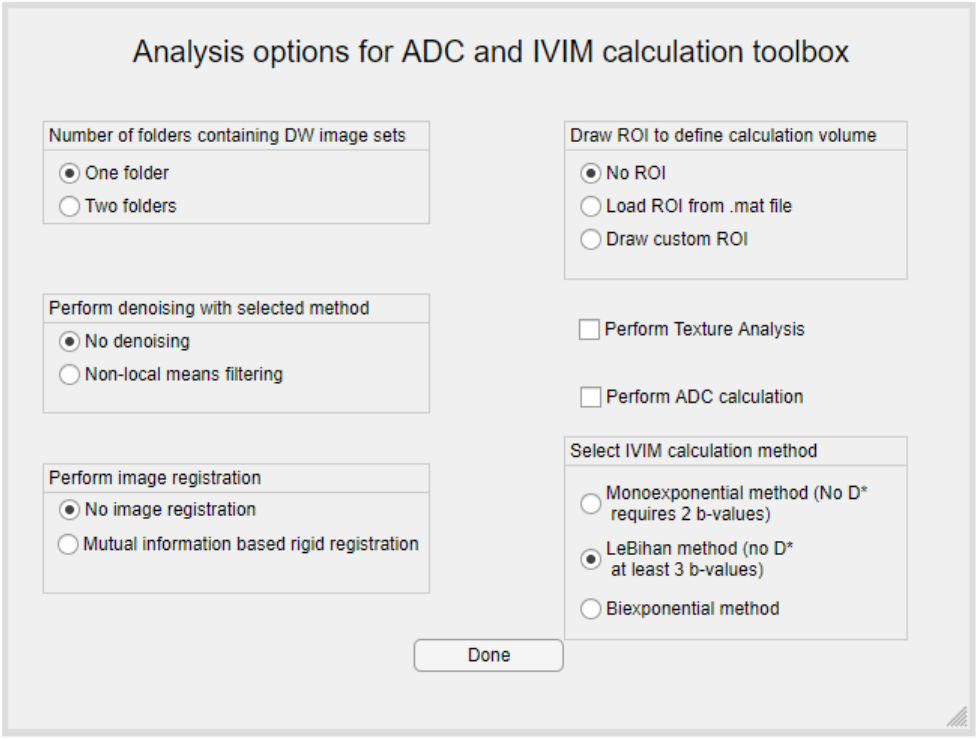

Fig. 36. A screen shot of the GUI developed for this work. Radial buttons and check boxes can be selected in each category to select data input type and desired output.

image sizes, number of b-values, and anatomical sites, which will be discussed in the following sections.

7.2 Testing with brain data

The first data set used for testing with the toolbox was a 21 b-value brain data set from the diffusion imaging in Python (DIPY) project by Garyfallidis et al [138]. An example slice with all b-values is shown in Figure 37, with b-values of: 0, 10, 20, 30, 40, 60, 80, 100, 120, 140, 160, 180, 200, 300, 400, 500, 600, 700, 800, 900, and 1000 s/mm^2. Data was initially in DICOM format.

To test the b-value and slice location sorting ability of the program, DICOM files were opened at random from the folder by selecting a random number between 1 and

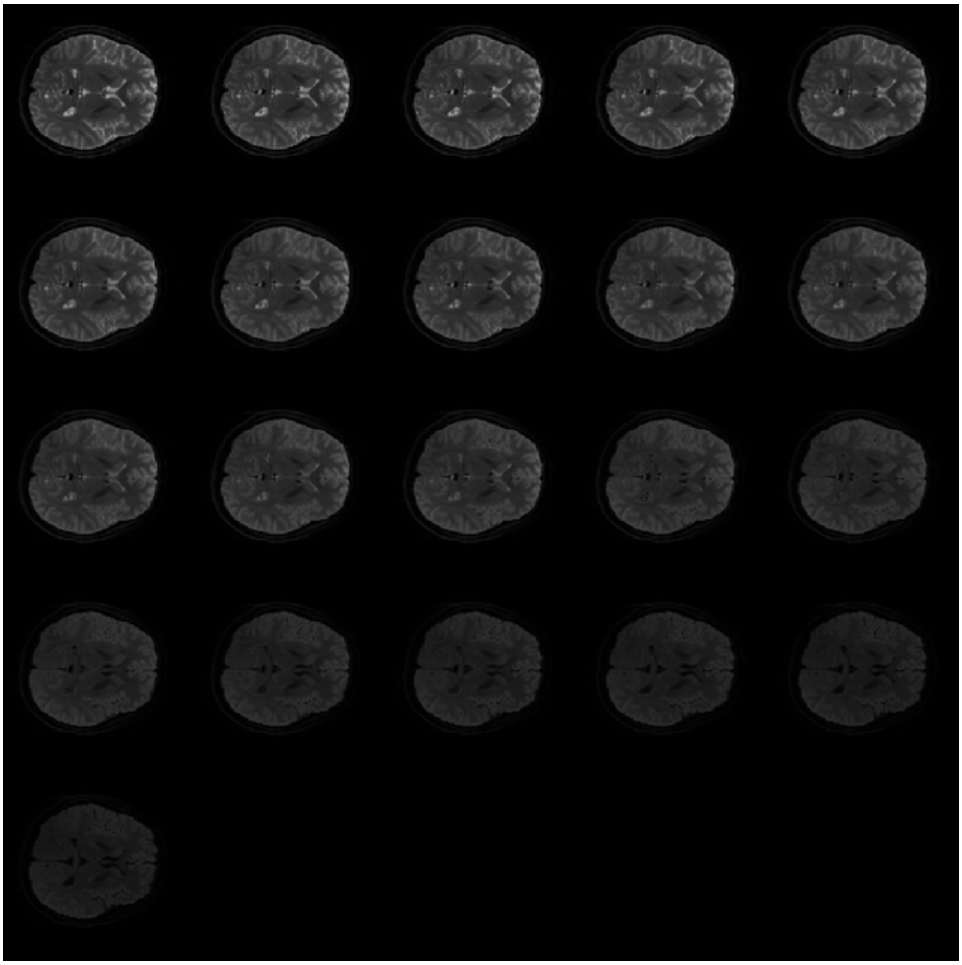

Fig. 37. A montage of all b-value images from a single slice in brain. The data set is from the DIPY project by Garyfallidis et al [138].

the total number of image files. Images were properly sorted into the final 4D image volume.

The image denoising ability was then tested by adding noise at six different levels, corresponding to SNR_{dB} of 30, 25, 20, 15, 10, and 5, where an SNR_{dB} of 30 would correspond to excellent image quality and 20 corresponds to acceptable image quality. The original SNR_{dB} of the images ranged from 34.17 to 31.14 dB in the b-value = 0 and 1000 s/mm^2 images respectively. SNR is related to SNR_{dB} by the following equation:

$$SNR = 10^{\frac{SNR_{dB}}{10}} \tag{7.1}$$

An example slice with added noise at each level is shown in Figure 38. These noisier images resulted in a poor fitting of data compared to the original image. The IVIM biexponential fit for original and added noise images is shown in Figure 39

After the addition of noise, IVIM parameters were calculated at hand drawn ROIs in the white matter of the brain. Increased noise resulted in a larger standard deviation value, and a change in the mean parameter values. When denoising was applied before IVIM analysis, the standard deviations decreased across all added noise levels, and for the values calculated for the original image. The values for IVIM parameters and their standard deviations with and without denoising are shown in Table 19.

This demonstrates that the denoising used in this project is able to remove noise from images without altering the resulting parameter values from their original values. The preservation of original, or true, parameter value with denoising is highly important due to the sensitivity of IVIM values to noise and voxel intensity fluctuations.

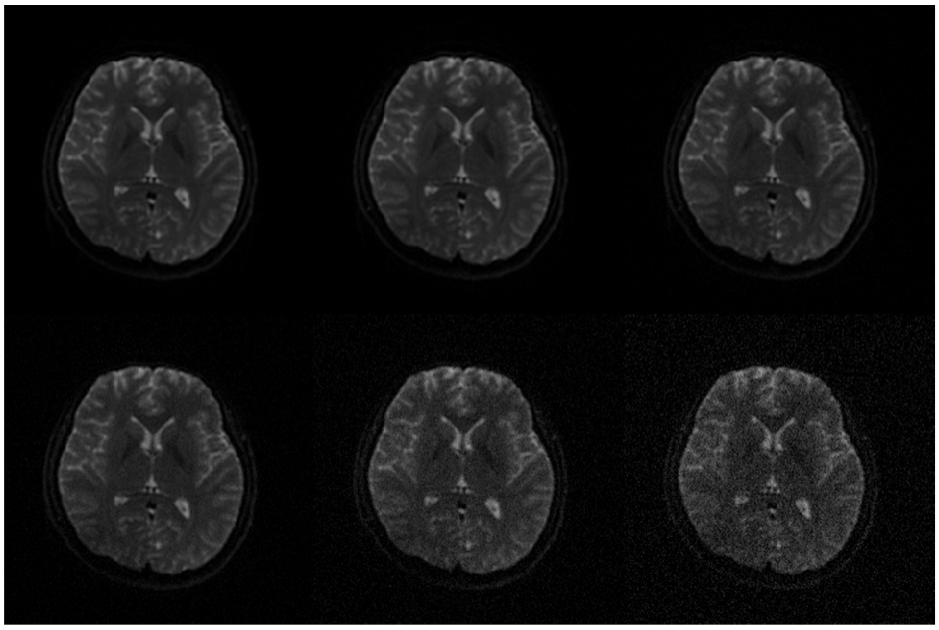

Fig. 38. A slice of the brain from the DIPY image set with added noise at 30, 25, 20 dB in the first row, and 15, 10, and 5dB in the second row. The original image had a noise level of 32dB

7.3 Testing with liver data

The toolbox was then tested with volunteer and patient data collected by this study. LeBihan's method and the biexponential model were applied to the volunteer liver, and to patient liver outside of the treatment area, and within the tumor volume. Parameter values are displayed in Table 20, and were calculated for 1200 voxels from ROIs placed on multiple slices.

The parameter calculation modules performed the correct calculations on the desired ROIs, which were placed in the same location across multiple slices for each of the 3 ROIs used, with 400 voxels within each ROI, for each volume investigated. It is noted that the biexponential model and LeBihan's method produce similar values for D, but have significantly different values for perfusion fraction. This is due to the direct fitting of the perfusion fraction with the biexponential model, while LeBihan's

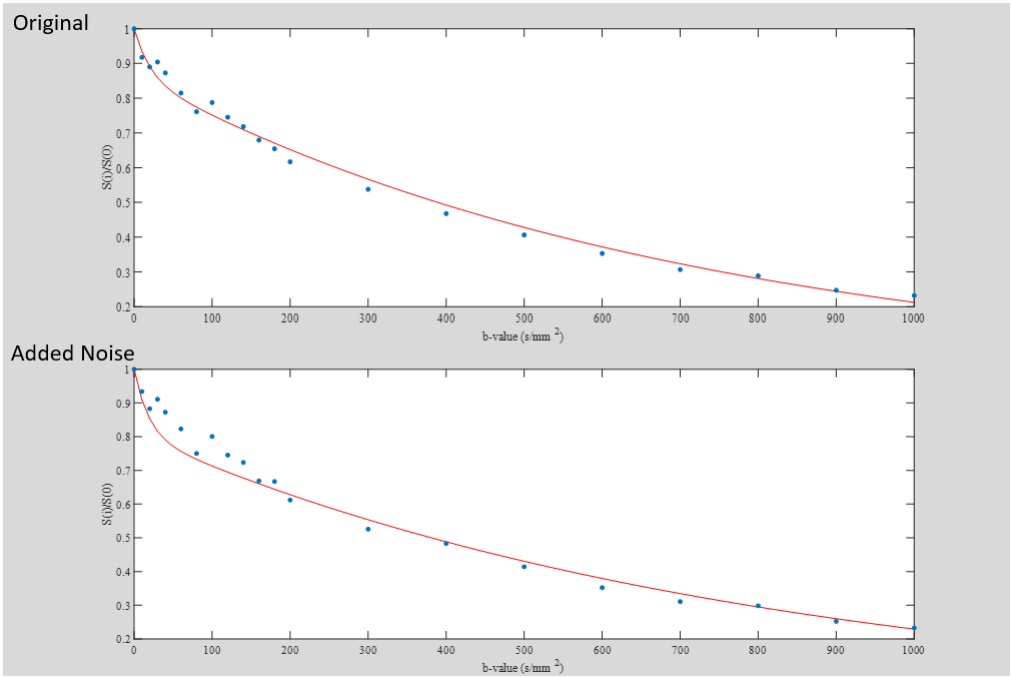

Fig. 39. A plot of relative signal intensity versus b-value, with a biexponential fit line of IVIM parameters for an ROI of the original image, and of an ROI with noise added to produce $\mathrm{SNR}_{dB} = 5$.

	SNR (dB)	ADC ($x10^{-3}$ mm^2/s)	D ($x10^{-3}$ mm^2/s)	D* ($x10^{-3}$ mm^2/s)	f (%)
No Denoising	Original	1.447 ± 0.807	1.403 ± 0.721	49.06 ± 53.54	13.67 ± 10.87
	30	1.410 ± 1.429	1.402 ± 0.723	51.27 ± 54.94	13.35 ± 10.70
	5	2.289 ± 5.943	1.259 ± 0.785	54.01 ± 58.91	19.20 ± 17.46
NLM Denoising	Original	1.533 ± 0.609	1.471 ± 0.656	46.21 ± 51.31	13.55 ± 9.16
	30	1.526 ± 0.614	1.467 ± 0.655	45.15 ± 51.29	13.33 ± 9.15
	5	1.522 ± 0.668	1.352 ± 0.641	56.90 ± 56.97	16.82 ± 11.93

Table 19. Mean ± standard deviation of IVIM parameters for the DIPY brain data set, calculated after noise was added, and after denoising to compare the results of denoising on the parameter values. The original noise values ranged from 34.17 dB to 31.14 dB in the 0 s/mm^2 and 1000 s/mm^2 images.

method attempts to do this calculation without input data which gives information on the perfusion region of the signal decay curve.

7.4 Summary

For application of IVIM analysis in the clinical setting, the ability to perform parameter calculation must be made accessible, reliable, and be presented in a straight forward manner. The developed toolbox generates a simple interface for selecting

Parameter	Volunteer	Pat. Liver	Pat. Tumor Pre	Pat. Tumor Post
ADC ($x10^{-3}mm^2/s$)	1.04 ± 0.30	1.09 ± 0.39	1.77 ± 1.92	1.28 ± 0.47
D Biexp. ($x10^{-3}mm^2/s$)	0.71 ± 0.14	0.75 ± 0.27	0.66 ± 0.08	0.92 ± 0.37
D LeBihan ($x10^{-3}mm^2/s$)	0.72 ± 0.31	0.81 ± 0.33	0.67 ± 0.42	1.10 ± 0.45
D* Biexp. ($x10^{-3}mm^2/s$)	62.59 ± 46.29	45.99 ± 49.45	55.63 ± 65.44	43.88 ± 58.12
D* LeBihan ($x10^{-3}mm^2/s$)	-	-	-	-
f Biexp. ($x10^{-3}mm^2/s$)	30.70 ± 13.66	35.01 ± 12.34	30.87 ± 18.57	37.19 ± 11.73
f LeBihan ($x10^{-3}mm^2/s$)	24.41 ± 15.43	23.24 ± 14.67	20.02 ± 3.96	18.49 ± 12.91

Table 20. Mean ± standard deviation for IVIM parameters, calculated using the bi-exponential and LeBihan methods, for healthy volunteer liver, patient liver outside of the treatment field, and liver tumor pre- and post-treatment.

image sets, drawing ROIs, and selecting what calculations to perform. The toolbox provides output data including the post-processed image volume with the selected post-processing methods applied, ADC and IVIM parameter maps for the method requested by the user, and texture feature maps and values for some of the most popular texture features in MRTA. This toolbox may also be used as a research tool for collection and analysis of data acquired in a larger study. The inclusion of less

accurate but also less computationally expensive models, could allow for an initial viewing of parameter maps prior to full computation if desired.

CHAPTER 8

SUMMARY AND CONCLUSIONS

The final Chapter of this dissertation gives a summary, discussion of some of the limitations of this work, possible improvements leading to future work, and a general conclusion to this body of work.

8.1 Summary

The work presented in this dissertation has demonstrated the feasibility of implementing an IVIM imaging protocol for use with SBRT of the liver. This research sought to accomplish three specific aims: The development, production, and evaluation of an MR safe respiratory motion management device with patient biofeedback, the development and implementation of an anatomical and functional imaging protocol, focusing on DWI and IVIM, for use with patients undergoing SBRT of the liver, and finally, the use of the developed motion management device and imaging protocol to develop a workflow for IVIM analysis and investigation of liver tumors treated with SBRT.

Fulfillment of the first specific aim was completed by design and production of the motion management device described in Chapter 4. Using CINE acquisition, belt signal was correlated with internal motion and shown to have small deviations from true internal motion. The belt was specifically designed to be usable across the entire radiotherapy workflow and is highly radiotransparent to kV and MV photons. Once testing was completed, and the motion management device was deemed to be fully-functioning, the second specific aim was undertaken. This aim was completed utilizing

imaging resources available at the CARI institute, and the device developed in aim 1. With the establishment of an imaging protocol with healthy volunteers, patients were recruited and imaged under the protocol. With patient data, this work moved to aim 3, and developing a workflow for IVIM analysis. The developed workflow allowed for image post-processing and analysis with minimal input from the operator using the custom designed GUI. With IVIM and texture analysis parameters acquired from the workflow, statistically significant differences in tissue were observed both between healthy and diseased tissue, and between pre-treatment and post-treatment volumes at various dose levels. This work shows the ability for IVIM to be used in the liver, and as an indicator of anatomical change due to radiotherapy, without the need to significantly impact the clinical workflow.

8.2 Limitations

This work is subject to several limitations. Some of these limitations are detailed in this section.

8.2.1 Limited patient number

The major limitation to this study is the limited patient cohort size. A total of five patients were recruited to the study, however only two completed the imaging protocol due to various reasons described in Chapter 6. Further validation with a larger data set in a clinical setting must be performed to verify statistical significance and investigate changes with different histopathologies, liver locations, and demographics. However, initial results from this cohort were promising and suggest that discrimination between tissue types and dose deposited is possible.

8.2.2 Volunteers and patients

A second limitation to this study is the demographic difference between the volunteer cohort, and the difference between the two patients. Diseases and characteristics of the liver are highly dependent on race, age, country, lifestyle, and liver function. The volunteer cohort in this study was much younger on average than the patients recruited from the radiation oncology clinic. This may skew data based on age, rather than true differences between liver IVIM parameters and texture features. Further, the two patients were different in many ways, including gender, race, age, and presence of liver cirrhosis. Liver cirrhosis may have a serious impact on values, especially those in the low dose region of the liver. The two patients also had primary versus metastatic lesions, and different responses to treatment. Patient 1 had a primary liver cancer and responded well to treatment, while patient 2 had metastatic HCC, and was showing limited response to treatment at the latest follow-up imaging session.

8.3 Future work

With the development of a robust toolbox for image evaluation, future efforts will be focused on expanding the patient cohort size and investigating parameter dependence on a variety of variables.

A vital component for continuation of work in this field is to accrue a larger patient data set. Currently, with only two clinical patient data sets the applicability of findings in this work to the clinical setting is limited. While a larger clinical study is needed, it represents another area of future work, for the study of IVIM parameter consistency between magnetic field strength, respiratory motion management styles, b-value selection, and even individual MRI machines. Due to the reliance of IVIM

parameters on signal decay, magnetic field inhomogeneities and strength will impact the computed values, and this change must be quantified or a method of correction needs to be produced for multi-center trials. In addition to parameter reproducibility, calculation time and operator input time can be significant factors in the application of IVIM to the clinical environment. Currently, liver segmentation must be performed by hand to create calculation ROIs. This is a time consuming task, even when contours do not need to be highly detailed. The development of a liver auto-segmentation tool would be valuable to the deployment of the protocol and workflow developed in this work to the clinic.

8.4 General conclusions

This dissertation investigated the development of an MR safe respiratory motion management device and explored IVIM and texture analysis parameters in the liver, including for patients receiving SBRT for liver cancer. This research was driven by three specific aims.

The first, to develop an MR safe respiratory motion management device, was necessary due to the lack of a device which is both MR compatible and can be used in the radiotherapy environment. A device was developed, constructed, and tested during MR acquisition to evaluate its impact on image quality, ease of use, and reduction of respiratory motion of the liver. The evaluation with an investigator cohort showed significantly reduced motion with CINE imaging, and both volunteer and patient cohorts were able to successfully learn proper use of the device and use it during image acquisition without significant time required for training. This novel approach to respiratory motion management with biofeedback allowed for implementing guided breath holds during image acquisition required for the next aim.

The second aim required the development of an MRI protocol, combining anatom-

ical and DWI sequences for IVIM analysis. Multiple DWI acquisitions were evaluated using different sets of b-values, motion management techniques, and signal averages. It was determined that exhalation breath hold was required during image acquisition to reduce motion, and eight b-values provided sufficient data sampling while not requiring an excessive number of breath holds or scan time. Consistent imaging parameters for DWI acquisition to be used with IVIM analysis were used for cohorts of volunteers and liver cancer patients, providing the required raw data for the third aim.

The third aim included the development of an IVIM analysis workflow, incorporating image post-processing methods to improve IVIM parameter quality, and applying the workflow to healthy volunteers and liver cancer patients pre- and post-treatment with SBRT. This was extended to include texture analysis and a comparison of values based on isodose lines. Significant differences were found between pre- and post-treatment tumors for IVIM parameters and texture features. It was also found that significant changes in IVIM parameters may occur outside of the treatment volume in the lower dose region over time. The data collected in this study represents the first attempt to quantify IVIM and texture analysis parameter changes due to radiotherapy for liver cancer. The results, while representing a small cohort, are promising for the use of IVIM and texture analysis in assessing treatment response to SBRT, and possibly as a pre-treatment indicator for efficacy of radiotherapy for individuals. As stated above, further investigation is required utilizing a larger cohort before the implementation of IVIM as an imaging biomarker, and the workflow and toolbox developed in this dissertation provide a means for expansion of this study.

REFERENCES

[1] F X Bosch et al. "Primary liver cancer: worldwide incidence and trends". In: *Gastroenterology* 127 (2004), S5–S16.

[2] Center for Disease Control Prevention. "Hepatocellular carcinoma-United States 2001-2006". In: *MMWR Morb Mortal Weekly Report* 59.17 (2010), pp. 517–520.

[3] A M Crissien and C Frenette. "Current management of hepatocellular carcinoma". In: *Gastroenterology and hepatology* 10.3 (2014), pp. 153–161.

[4] International agency for research on cancer. "Monographs on the evaluation of carcinogenic risks to humans". In: *Hepatitis Viruses* 59 (1994), pp. 182–221.

[5] C Gao et al. "Potential role of diabetes mellitus in the progression of cirrhosis to hepatocellular carcinoma: a crosssectional case-control study from Chinese patients with HBV infection". In: *Hepatobiliary Pancreas Distribution International* 12.4 (2013), pp. 385–393.

[6] C Wang, X Wang, and G Gong. "Increased risk of hepatocellular carcinoma in patients with diabetes mellitus: a systematic review and meta-analysis of cohort studies". In: *International journal of Cancer* 130.7 (2012), pp. 1639–1648.

[7] J Balogh et al. "Hepatocellular carcinoma: a review". In: *Journal of Hepatocellular carcinoma* 3 (2016), pp. 41–53.

[8] T Takashima et al. “Diagnosis and screening of small hepatocellular carcinomas. Comparison of radionuclide imagin, ultrasound, computed tomography, hepatic angiography, and alpha1-fetoprotein assay”. In: *Radiology* 145 (1982), pp. 635–638.

[9] D D Brahee, C Ogedegbe, and C Hassler. “Body mass index and abdominal ultrasound image quality: a pilot survey of sonographers”. In: *Journal of Diagnostic Medical Sonography* 29.2 (2013), pp. 66–72.

[10] P Allemann et al. “Longterm outcome after liver resection for hepatocellular carcinoma larger than 10cm”. In: *World Journal of Surgery* 37.2 (2013), pp. 452–458.

[11] R Baskar, K A Lee, and K W Yeoh. “Cancer and radiation therapy: current advances and future directions”. In: *International journal of medical sciences* 9.3 (2012), pp. 193–199.

[12] M Gamulin, V Garaj-Vrhovac, and N Kopkar. “Evaluation of DNA damage in radiotherapy-treated cancer patients using the alkaline comet assay”. In: *Collegium Antropologicum* 31.3 (2007), pp. 837–845.

[13] R Lenhard, R T Osteen, and T Gansler. *Clinical Oncology*. Blackwell Publishing, INC, 2001.

[14] A M DiBisceglie. *Malignant neoplasms of the liver. IN: Schiff’s Diseases of the Liver. 8th Ed.* Lippincott Raven, 1999.

[15] J P Ayoub et al. “Unknown primary tumors metastatic to liver”. In: *Journal of Clinical Oncology* 16 (1998), pp. 2105–2112.

[16] M C Kew et al. *Gastrointestinal and liver disease: pathophysiology/diagnosis/management. 7th Ed.* Saunders, 2002.

[17] L.Leksell. "The stereotaxic method and radiosurgery of the brain." In: *Acta Chir Scand* 102.4 (1951), pp. 316–319.

[18] A. Chan, R. Cardinale, and J. Loeffler. *Stereotactic Irradiation. In The Principles and Practice of Radiation Oncology Forth Edition*. Lippincott Williams and Wilkins, 2004.

[19] Volker Stieber et al. "Stereotactic body radiation therapy: The report of AAPM Task Group 101". In: *Medical Physics* 37.8 (2010), pp. 4078–4101. DOI: 10.1118/1.3438081.

[20] S. Du et al. "Clinical value of Active Breathing Coordinator (ABC) during three-dimensional conformal radiotherapy for patients with intrahepatic tumor." In: *AustralAsian Journal of Cancer* 7.1 (2008), pp. 15–23.

[21] William B Harms et al. "IMAGE-GUIDED RADIATION THERAPY COMMITTEE Image-Guided Radiotherapy Committee Key Members : Jeffrey Michalski , M . D ., Chair , (1997); James A . Purdy , Ph . D ., Co-Chair ; Laurie Gaspar , M . D ., Co-Chair , Brachytherapy Committee Liaison ; Luis Sou". In: *Radiation Oncology* 51.3 (2001), pp. 60–65.

[22] Albert Tiong et al. "Faculty of Radiation Oncology Position Paper on the use of Image Guided Radiation Therapy". In: *Journal of Medical Imaging and Radiation Oncology* 60.6 (2016), pp. 772–780. ISSN: 17549485. DOI: 10.1111/1754-9485.12463.

[23] Jennifer De Los Santos et al. "Image guided radiation therapy (IGRT) technologies for radiation therapy localization and delivery". In: *International Journal of Radiation Oncology Biology Physics* 87.1 (2013), pp. 33–45. DOI: 10.1016/j.ijrobp.2013.02.021. URL: http://dx.doi.org/10.1016/j.ijrobp.2013.02.021.

[24] R W van der Put et al. "Integrating a 1.5 T MRI scanner with a 6 MV accelerator: proof of concept". In: *Physics in Medicine and Biology* 54.12 (2009), N229–N237. ISSN: 0031-9155. DOI: 10.1088/0031-9155/54/12/n01.

[25] K K Herfarth, J Debus, and Wannenmacher M. "Stereotactic radiation therapy of liver metastases: Update of the initial phase-i/ii trial". In: *Frontiers of Radiation Therapy and Oncology* 38 (2004), pp. 100–105.

[26] A Bujold, C A Massey, and J J Kim. "Sequential phase i and ii trials of stereotactic body radiotherapy for locally advanced hepatocellular carcinoma". In: *Journal of Clinical Oncology* 44 (2013), p. 1659.

[27] D L Andolino et al. "Stereotactic body radiotherapy for primary hepatocellular carcinoma". In: *International Journal of Radiation Oncology*Biology*Physics* 81 (2011), e447–e453.

[28] K A Goodman et al. "Dose-escalation study of single fraction stereotactic body radiotherapy for liver malignancies". In: *International Journal of Radiation Oncology*Biology*Physics* 78 (2010), pp. 486–493.

[29] C C Pan et al. "Radiation-associated liver injury". In: *International Journal of Radiation Oncology*Biology*Physics* 76 (2010), S94–S100.

[30] L J Wang et al. "Radiofrequency ablation versus resection for technically resectable colorectal liver metastasis: a propensity score analysis." In: *World Journal of Surgical Oncology* 16.1 (2011), p. 207.

[31] S H Benedict et al. "Stereotactic body radiation therapy: The report of AAPM Task Group 101". In: *Medical Physics* 37.8 (2010), pp. 4078–4101.

[32] S M Bentzen et al. "Quantitative Analyses of Normal Tissue Effects in the Clinic (QUANTEC): an introduction to the scientific issues". In: *International Journal of Radiation Oncology*Biology*Physics* 76 (2010), S3–9.

[33] M A Clifford et al. "Assessment of hepatic motion secondary to respiration for computer assisted interventions". In: *Computer Aided Surgery* 7.5 (2002), pp. 291–299.

[34] I Suramo, M Paivansalo, and V Myllyla. "Cranio-caudal movements of the-liver, pancreas and kidneys in respiration". In: *Acta Radiologica* 25.2 (1984), pp. 129–131.

[35] T F Chan and L A Vese. "Active contours without edges". In: *Image Processing, IEEE Transactions on* 10.2 (2001), pp. 266–277.

[36] J M Blackall et al. "A statisticalmodel of respiratory motion and deformation of the liver". In: *Lecture Notes in Computer Science* (2001), pp. 1338–1340.

[37] Thirion. J P. "Image matching as a diffusion process: an analogy with Maxwells demons". In: *Medical Image Analysis* 2.3 (1998), pp. 243–260.

[38] R Danrad and D R Martin. "MR imaging of diffuse liver diseases". In: *Magnetic resonance imaging clinics of North America* 13.2 (2005), p. 277.

[39] S C Davies et al. "Ultrasound quantitation of respiratory organ motion in the upper abdomen". In: *British Journal of Radiology* 67.803 (1998), p. 1096.

[40] S Shimizu et al. "Three-dimensional movement of a liver tumor detected by high-speed magnetic resonance imaging". In: *Radiotherapy and Oncology* 50.3 (1999), pp. 367–370.

[41] A K Paulsson et al. “Respiration-induced intraorgan deformation of the liver: implications for treatment planning in patients treated wih fiducial tracking”. In: *Technology in Cancer Research and Treatment* 16.6 (2017), pp. 776–782.

[42] R B Case et al. “Interfraction and Intrafraction Changes in Amplitude of Breathing Motion in Stereotactic Liver Radiotherapy”. In: *International Journal of Radiation Oncology*Biology*Physics* 77.3 (2010), pp. 918–925.

[43] J L Hallman et al. “A Four-Dimensional Computed Tomography Analysis of Multiorgan Abdominal Motion”. In: *International Journal of Radiation Oncology*Biology*Physics* 83.1 (2012), pp. 435–441.

[44] J Yang et al. “Is Diaphragm Motion a Good Surrogate for Liver Tumor Motion?” In: *International Journal of Radiation Oncology*Biology*Physics* 90.4 (2014), pp. 952–958.

[45] J Dhont et al. “The long- and short-term variability of breathing induced tumor motion in lung and liver over the course of a radiotherapy treatment”. In: *Radiotherapy and Oncology* 126.2 (2018), pp. 339–346.

[46] B Wysocka et al. “Interfraction and Intrafraction Changes in Amplitude of Breathing Motion in Stereotactic Liver Radiotherapy”. In: *International Journal of Radiation Oncology*Biology*Physics* 77.1 (2010), pp. 53–59.

[47] M A Zahra et al. “Semiquantitative dynamic contrast-enhanced magnetic resonance imaging measurements predict radiation response in cervix cancer.” In: *International Journal of Radiation Oncology*Biology*Physics* 74.3 (2009), pp. 766–773.

[48] J A Loncaster et al. “Prediction of radiotherapy outcome using dynamic contrast enhanced MRI of carcinoma of the cervix”. In: *International Journal of Radiation Oncology*Biology*Physics* 54 (2002), pp. 759–767.

[49] H Hawighorst et al. “Prediction of radiotherapy outcome using dynamic contrast enhanced MRI of carcinoma of the cervix”. In: *Clinical Cancer Research* 4.2 (1998), pp. 2305–2312.

[50] H Konouchi et al. “Evaluation of tumor proliferation using dynamic contrast enhanced-MRI of oral cavity and oropharyngeal squamous cell carcinoma”. In: *Oral Oncology* 39 (2003), pp. 290–295.

[51] M Andreucci, R Solomon, and A Tasanarong. “Side effects of radiographic contrast media: pathogenesis, risk factors, and prevention”. In: *BioMed Research International* 2014 (2014).

[52] Y Mardor et al. “Early detection of response to radiation therapy in patients with brain malignancies using conventional and high b-values diffusion weighted magnetic resonance imaging”. In: *Journal of Clinical Oncology* 21.6 (2003), pp. 1094–1100.

[53] G Oldrini et al. “Tumor response assessment by MRI following stereotactic body radiation therapy for hepatocellular carcinoma”. In: *PLOS ONE* (2017).

[54] C C Pieper et al. “Evaluation of a simplified intravoxel incoherent motion (IVIM) analysis of diffusion-weighted imaging for prediction of tumor size changes and imaging response in breast cancer liver metastases undergoing radioembolization”. In: *Medicine* 95.14 (2016), e3275.

[55] J Michalski, J A Purdy, and L Gaspar. "Radiation Therapy Oncology Group Research plan 2002-2006". In: *International Journal of Radiation Oncology*Biology*Physics* 51.2 (2001), pp. 60–65.

[56] P J Keall et al. "The management of respiratory motion in radiation oncology report of AAPM Task Group 76". In: *Medical Physics* 33.10 (2006), pp. 3874–3900.

[57] D Nishimura. *Principles of Magnetic Resonance Imaging*. www.lulu.com, 2010.

[58] H E John. *Guyton and Hall Textbook of Medical Physiology 13th Edition*. Elsevier Saunders, 2015.

[59] F Bloch. "Nuclear Induction". In: *Physics Review* 70 (1946), pp. 460–474.

[60] R Brown. "A brief account of microscopical observations made in the months of June, July and August, 1827, on the particles contained in the pollen of plants; and on the generalexistence of active molecules in organic and inorganic bodies". In: *Philisophical Magazine* 4 (1828), pp. 161–173.

[61] A Einstein. "Investigations on the Theory of the Brownian Movement. edited with notes by R. Furth". In: *Dover Publications* (1956).

[62] D Le Bihan and M Iima. "Diffusion Magnetic Resonance Imaging: What Water Tells Us about Biological Tissues". In: *PLoS Biology* 13.7 (2015).

[63] E Hahn. "Spin Echoes". In: *Physical Review* 80 (1950), pp. 580–594.

[64] R Stejskal and J Tanner. "Spin Diffusion Measurements: Spin Echoes in the Presence of a Time Dependent Field Gradient". In: *Journal of Chemistry and Physics* 42 (1965), pp. 288–292.

[65] D Le Bihan and E Breton. "Imagerie de Diffusion In Vivo par Resonance Magnetique Nucleaire". In: *Curie Radiology Acadamy of Sciences Paris* 301 (1985), pp. 1109–1112.

[66] D Le Bihan et al. "MR imaging of intravoxel incoherent motions: application to diffusion and perfusion in neurologic disorders". In: *Radiology* 161.2 (1986), pp. 401–407.

[67] M Iima and D Le Bihan. "Clinical intravoxel incoherent motion and diffusion MR imaging: past, present, and future". In: *Radiology* 278.1 (2015), pp. 13–32.

[68] Y T Li et al. "Liver intravoxel incoherent motion (IVIM) magnetic resonance imaging: a comprehensive review of published data on normal values and applications for fibrosis and tumor evaluation". In: *Quantitative Imaging in Medicine and Surgery* 7.1 (2017), pp. 59–78.

[69] D Le Bihan et al. "Separation of diffusion and perfusion in intravoxel incoherent motion MR imaging." In: *Radiology* 168 (1988), pp. 497–505.

[70] D Le Bihan and R Turner. "The capillary network: a link between IVIM and classical perfusion". In: *Magnetic Resonance in Medicine* 27 (1992), pp. 171–178.

[71] D Le Bihan et al. "Imaging of diffusion and microcirculation with gradient sensitization: design, strategy, and significance". In: *Journal of Magnetic Resonance in Medicine* 1 (1991), pp. 7–28.

[72] I Jambor et al. "Optimization of b-value distribution for biexponential diffusion-weighted MR imaging of normal prostate". In: *Journal of Magnetic Resonance Imaging* 39.5 (2014), pp. 1213–1222.

[73] A D Cohen et al. "The Effect of Low b-Values on the Intravoxel Incoherent Motion Derived Pseudodiffusion Parameter in Liver". In: *Magnetic Resonance in Medicine* 73.1 (2015), pp. 306–311.

[74] S Barbieri et al. "Impact of the calculation algorithm on biexponential fitting of diffusion-weighted MRI in upper abdominal organs". In: *Magnetic Resonance in Medicine* 75.5 (2016), pp. 2175–2184.

[75] Y Pang et al. "Intravoxel incoherent motion MR imaging for prostate cancer: an evaluation of perfusion fraction and diffusion coefficient derived from different b-value combinations". In: *Magnetic Resonance in Medicine* 69.2 (2013), pp. 553–562.

[76] W C Wu et al. "Caveat of measuring perfusion indexes using intravoxel incoherent motion magnetic resonance imaging in the human brain". In: *European Journal of Radiology* 25.8 (2015), pp. 2485–2492.

[77] H J Park et al. "Intravoxel incoherent motion diffusion-weighted MRI of the abdomen: The effect of fitting algorithms on the accuracy and reliability of the parameters". In: *Journal of Magnetic Resonance Imaging* 41.5 (2016), pp. 1236–1241.

[78] J Conklin et al. "A Simplified Model for Intravoxel Incoherent Motion Perfusion Imaging of the Brain". In: *American Journal of Neuroradiology* (2016).

[79] R M Haralick, K Shanmugam, and I Dinstein. "Texture features for image classification." In: *Systems, Man and Cybernetics* 3 (1973), pp. 610–621.

[80] B Julesz et al. "Inability of humans to discriminate between visual textures that agree in second order statistics: revisited". In: *Perception* 2 (1973), pp. 391–405.

[81] M Tuceryan and A K Jain. *Texture Analysis. In: The Handbook of Pattern Recognition and Computer Vision*. World Scientific Publishing Co, 1998.

[82] M G Lubner et al. "CT Texture Analysis: Definitions, Applications, Biologic Correlates, and Challenges". In: *Radiographics* 37.5 (2017), pp. 1483–1503.

[83] H Kaizer. "A quantification of textures on aerial photographs, Technical note". In: *Boston University Research Laboratory* 121 (2017), p. 69484.

[84] G N Srinivasan and G Shobha. "Statistical texture analysis". In: *Proceedings of World Academy of Science, ENgineering, and Technology* 36 (2008), pp. 1264–1269.

[85] R M Haralick and L Watson. "A facet model for imaging data". In: *Computer vision graphics and image processing* 15 (1981), pp. 113–129.

[86] S Kim et al. "Audiovisual biofeedback improves diaphragm motion reproducibility in MRI". In: *Medical Physics* 39.11 (2012), pp. 6921–6928.

[87] Y K Park et al. "Quasi-breath-hold technique using personalized audio-visual feedback for respiratory motion management in radiotherapy". In: *Meidcal Physics* 38.6.1 (2011), pp. 3114–3124.

[88] S Pollock, R Keall, and P Keall. "Breathing guidance in radiation oncology and radiology: A systematic review of patient and healthy volunteer studies". In: *Medical Physics* 42.9 (2015), pp. 5490–5509.

[89] T Kim et al. "Motion management within two respiratory-gating windows: feasibility study of dual quasi-breath-hold technique in gated medical procedures". In: *Physics in Medicine and Biology* 59 (2014), pp. 6583–6594.

[90] T Kim et al. "Development of real time abdominal compression force monitoring and visual biofeedback system". In: *Physics in Medicine and Biology* 63.5 (2018).

[91] J Patel et al. "Diagnosis of cirrhosis with intravoxel incoherent motion diffusion MRI and dynamic contrast-enhanced MRI alone and in combination: preliminary experience". In: *Journal of Magnetic Resonance Imaging* 31.3 (2010), pp. 589–600.

[92] A Luciani et al. "A. Liver cirrhosis: intravoxel incoherent motion MR imaging–pilot study." In: *Radiology* 249.3 (2008), pp. 891–899.

[93] A M Chow et al. "Liver fibrosis: an intravoxel incoherent motion (IVIM) study". In: *Journal of Magnetic Resonance Imaging* 36.1 (2012), pp. 159–167.

[94] H A Dyvorne et al. "Diffusion-weighted imaging of the liver with multiple b values: effect of diffusion gradient polarity and breathing acquisition on image quality and intravoxel incoherent motion parameters–a pilot study". In: *Radiology* 266.3 (2013), pp. 920–929.

[95] R Wirestam et al. "Perfusion-related parameters in intravoxel incoherent motion MR imaging compared with CBV and CBF measured by dynamic susceptibility-contrast MR technique". In: *Acta Radiology* 42.2 (2001), pp. 123–128.

[96] C Federau et al. "Quantitative measurement of brain perfusion with intravoxel incoherent motion MR imaging". In: *Radiology* 265.3 (2012), pp. 874–881.

[97] A Andreou et al. "Short term measurement reproducibility of perfusion fraction (f), pseudo-diffusion coefficient (D*) and diffusion coefficient (D) in col-

orectal liver metastases derived by intravoxel incoherent motion analysis of respiratory-triggered diffusion-weighted MR imaging". In: *ISMRM* (2011).

[98] I Yamada et al. "Diffusion coefficients in abdominal organs and hepatic lesions: evaluation with intravoxel incoherent motion echo-planar MR imaging". In: *Radiology* 210.3 (1999), pp. 617–623.

[99] A Andreou et al. "Measurement reproducibility of perfusion fraction and pseudodiffusion coefficient derived by intravoxel incoherent motion diffusion-weighted MR imaging in normal liver and metastases". In: *European Radiology* 23.2 (2013), pp. 428–434.

[100] M C Wurnig et al. "A Standardized Parameter-Free Algorithm for Combined Intravoxel Incoherent Motion and Diffusion Kurtosis Analysis of Diffusion Imaging Data". In: *Investigative Radiology* 51 (2016), pp. 203–210.

[101] B Leporq et al. "Optimization of intra-voxel incoherent motion imaging at 3.0 Tesla for fast liver examination". In: *Magnetic Resonance Imaging* 41 (2015), pp. 1209–1217.

[102] V Taimouri et al. "Spatially constrained incoherent motion method improves diffusion-weighted MRI signal decay analysis in the liver and spleen". In: *Medical Physics* 42 (2015), pp. 1895–1903.

[103] A Lemke et al. "Toward an optimal distribution of b values for intravoxel incoherent motion imaging". In: *Magnetic Resonance Imaging* 29 (2011), pp. 766–776.

[104] E E ter Voert et al. "Intravoxel Incoherent Motion Protocol Evaluation and Data Quality in Normal and Malignant Liver Tissue and Comparison to the Literature". In: *Investigative Radiology* 51 (2016), pp. 90–99.

[105] M C Wurnig et al. “Systematic analysis of the intravoxel incoherent motion threshold separating perfusion and diffusion effects: Proposal of a standardized algorithm”. In: *Megnetic Resonance in Medicine* 74 (2015), pp. 1414–1422.

[106] O J Gurney-Champion et al. “Minimizing the Acquisition Time for Intravoxel Incoherent Motion Magnetic Resonance Imaging Acquisitions in the Liver and Pancreas”. In: *Investigative Radiology* 51 (2016), pp. 211–220.

[107] B Guiu et al. “Intravoxel incoherent motion diffusion-weighted imaging in nonalcoholic fatty liver disease: a 3.0-T MR study”. In: *Radiology* 265 (2012), pp. 96–103.

[108] P X Lu et al. “Decreases in molecular diffusion, perfusion fraction and perfusion-related diffusion in fibrotic livers: a prospective clinical intravoxel incoherent motion MR imaging study”. In: *PLos One* 9 (2014), e113846.

[109] F Regini et al. “Assessment of Liver Perfusion by IntraVoxel Incoherent Motion (IVIM) Magnetic Resonance-Diffusion-Weighted Imaging: Correlation With Phase-Contrast Portal Venous Flow Measurements”. In: *Journal of Computer Assisted Tomography* 39 (2015), pp. 365–372.

[110] T Hayashi et al. “Diffusion analysis with triexponential function in liver cirrhosis”. In: *Magnetic Resonance Imaging* 38 (2013), pp. 148–153.

[111] S R Chung et al. “Intravoxel incoherent motion MRI for liver fibrosis assessment: a pilot study”. In: *Acta Radiology* 56 (2015), pp. 1428–1436.

[112] J P Cercueil et al. “Intravoxel incoherent motion diffusion-weighted imaging in the liver: comparison of mono-, bi- and tri-exponential modelling at 3.0-T”. In: *European journal of Radiology* 25 (2015), pp. 1541–1550.

[113] S Ichikawa et al. "MRI-based staging of hepatic fibrosis: Comparison of intravoxel incoherent motion diffusion-weighted imaging with magnetic resonance elastography". In: *Magnetic Resonance Imaging* 42 (2015), pp. 2049–2058.

[114] N P Jerome et al. "Comparison of free-breathing with navigator-controlled acquisition regimes in abdominal diffusion-weighted magnetic resonance images: Effect on ADC and IVIM statistics". In: *Magnetic Resonance Imaging* 39 (2014), pp. 235–240.

[115] L Zhu et al. "A comparative study of apparent diffusion coefficient and intravoxel incoherent motion-derived parameters for the characterization of common solid hepatic tumors". In: *Acta Radiology* 56 (2015), pp. 1411–1418.

[116] H S Leitao et al. "Fat deposition decreases diffusion parameters at MRI: a study in phantoms and patients with liver stenosis". In: *European journal of Radiology* 23 (2013), pp. 461–467.

[117] G Gambarota et al. "Eliminating the blood-flow confounding effect in intravoxel incoherent motion (IVIM) using the non-negative least square analysis in liver". In: *Magnetic Resonance in Medicine* 77 (2017), pp. 310–317.

[118] J Zhang et al. "MRI-based estimation of liver function by intravoxel incoherent motion diffusion-weighted imaging." In: *Magnetic Resonance Imaging* 34 (2016), pp. 1220–1225.

[119] M Franca et al. "Evaluation of fibrosis and inflammation in diffuse liver diseases using intravoxel incoherent motion diffusion-weighted MR imaging". In: *Abdominal Radiology* 42.2 (2017), pp. 468–477.

[120] S Kakite et al. “Hepatocellular carcinoma: short-term reproducibility of apparent diffusion coefficient and intravoxel incoherent motion parameters at 3.0T”. In: *Magnetic Resoance Imaging* 41 (2015), pp. 149–56.

[121] H Dyvorne et al. “In vivo cardiac diffusion-weighted magnetic resonance imaging: quantification of normal perfusion and diffusion coefficients with intravoxel incoherent motion imaging”. In: *Investigative Radiology* 47 (2014), pp. 662–670.

[122] Y Cui et al. “IVIM Diffusion weighted imaging of the liver at 3.0T: Comparison with 1.5T”. In: *European Journal of Radiology* 2 (2015), pp. 123–128.

[123] C Reischauer and A Gutzeit. “Image denoising substantially improves accuracy and precision of intravoxel incoherent motion parameter estimates”. In: *PLos ONE* 34 (2017), pp. 1220–1225.

[124] N Wiest-Daessle et al. “. Non-local means variants for denoising of diffusion-weighted and diffusion tensor MRI. In: Medical Image Computing and Computer-Assisted Intervention”. In: *Lecture Notes in Computer Science* 4792 (2007).

[125] J V Manjon et al. “Diffusion weighted image denoising using overcomplete local PCA”. In: *PLos ONE* (2013).

[126] F Lam et al. “Denoising diffusion-weighted magnitude MR images using rand and edge constraints”. In: *Magnetic Resonance in Medicine* 71 (2014), pp. 1272–1284.

[127] A H Penner, A M Sprinkart, and G M Kukuk. “Intravoxel incoherent motion model-based liver lesion characterisation from three b-value diffusion-weighted MRI”. In: *European Journal of Radiology* 23 (2013), pp. 2773–2783.

[128] J H Yoon, J M Lee, and M H Yu. "Evaluation of hepatic focal lesions using diffusion-weighted MR imaging: Comparison of apparent diffusion coefficient and intravoxel incoherent motion-derived parameters". In: *Journal of Magnetic Resonance Imaging* 39 (2014), pp. 276–285.

[129] S Colagrande, F Regini, and F Pasquinelli. "Focal liver lesion classification and characterization in noncirrhotic liver: a prospective comparison of diffusion-weighted magnetic resonance-related parameters". In: *Journal of Computer Assisted Tomography* 37 (2013), pp. 560–567.

[130] Z-H Fan et al. "Evaluation of primary malignancies of the liver using contrast-enhanced sonography: correlation with pathology". In: *Abdominal Imaging* 186 (2006), pp. 1512–1519.

[131] S-S Yin, M H Chen, and K Yan. "Role of gray-scale contrast enhanced ultrasound in diagnosis of liver metastasis". In: *Ultrasonography* 14 (2005), pp. 354–358.

[132] Y Lee et al. "Intravoxel incoherent motion diffusion-weighted MR imaging of the liver: effect of triggering methods on regional variability and measurement repeatability of quantitative parameters". In: *Radiolgy* 274 (2015), pp. 405–415.

[133] A Klauss M andLemke and K Grunberg. "Intravoxel incoherent motion MRI for the differentiation between mass forming chronic pancreatitis and pancreatic carcinoma". In: *Investigative Radiology* 46 (2011), pp. 57–63.

[134] G Boris and J-P Cercueil. "Liver diffusion weighted MR imaging: the tower of Babel?" In: *European Journal of Radiology* 21 (2011), pp. 463–467.

[135] L Filli et al. "Whole-body intravoxel incoherent motion imaging". In: *European Journal of Radiology* 25 (2015), pp. 2049–2058.

[136] J J Neil and G L Bretthorst. "On the use of Bayesian probability theory for analysis of exponential decay data: an example taken from intravoxel incoherent motion experiments". In: *Magnetic Resonance in Medicine* 29 (1993), pp. 642–647.

[137] A Buades, B Coll, and J-M Morel. "A non-local algorithm for image denoising". In: *IEEE Computer Society Conference on Computer Vision and Pattern Recognition* (2005).

[138] E Garyfallidis et al. "DIPY, a library for the analysis of diffusion MRI data". In: *Frontiers in Neuroinformatics* 8.8 (2014).

Appendix A

INTERNAL REVIEW BOARD PROTOCOL

A.1 IRB Protocol MCC-16-13073

Virginia Commonwealth University Massey Cancer Center

MCC Protocol #: MCC-16-13073

VCU IRB #: HM20010234

A Pilot Study to Develop a Clinical MRI Procedure and Application for Precise Stereotactic Body Radiation Therapy to Treat Primary or Metastatic Cancer in the Liver

Sponsor-Investigator
Taeho Kim, PhD
VCU Radiation Oncology
401 College Street
PO Box 980058
Richmond, VA 23298-0058
Phone: 804-828-7418
Email: taeho.kim@vcuhealth.org

Coordinating Study Team
VCU Massey Cancer Center
Radiation Oncology Clinical Trials Program
Phone: 804-628-2334
Fax: 804-628-9960
Email: masseyradonc@vcu.edu

Co-Investigator
Emma Fields, MD
VCU Radiation Oncology
401 College Street
PO Box 980058
Richmond, VA 23298
Phone: 804-628-1031
Email: ecfields@vcu.edu

Co-Investigator
Siyong Kim, PhD
VCU Radiation Oncology
401 College Street
PO Box 980058
Richmond, VA 23298-0058
Phone: 804-828-7232
Email: siyong.kim@vcuhealth.org

Co-Investigator
Julie M. Coe, DDS, MBA, MS
VCU School of Dentistry
520 North 12th Street
Box 980566
Richmond, VA 23298-0566
Phone: 804-828-2977
Email: jmcoe@vcu.edu

Biostatistician
Nitai D. Mukhopadhyay, PhD
VCU Massey Cancer Center
Theater Row, Room 3028
730 East Broad Street
Richmond, VA 23298
Phone: 804-827-2053
Email: nitai.mukhopadhyay@vcuhealth.org

Responsible Research Nurse
Daeryl Williamson, RN, BSN
VCU Radiation Oncology
401 College Street
PO Box 23298-0058
Richmond VA 23298
Phone: 804-628-2334
Email: johnsondl4@vcu.edu

TABLE OF CONTENTS

LIST OF FIGURES

LIST OF TABLES

LIST OF ABBREVIATIONS

ABC	active breathing coordinator
ADC	apparent diffusion coefficient
AV	audiovisual
CARI	Collaborative Advanced Research Imaging
CRF	case report form
CT	computer-aided tomography
DTI	diffusion tensor imaging
DWI	diffusion-weighted imaging
IRB	Institutional Review Board
MCC	Massey Cancer Center
MR	magnetic resonance
MRE	magnetic resonance elastography
MRI	magnetic resonance imaging
PoSA	purpose-oriented sampling approach
PRMC	Protocol Review and Monitoring Committee
RMSE	root-mean-square error
RPM	real-time position management
RT	radiation therapy
SAP-4D MRI	sectional-view-aided pseudo-4 dimensional magnetic resonance imaging
SBRT	stereotactic body radiotherapy
T	tesla
TR	repetition time
TE	echo time
UADE	unanticipated adverse device effect
VCU	Virginia Commonwealth University
WCBP	woman of childbearing potential

1 BACKGROUND

1.1 Overview

Approximately 40,000 liver tumors are diagnosed each year in the United States (1) with only a small fraction of those eligible for curative resection or transplant. Alternative local therapies, such as stereotactic body radiotherapy (SBRT), are therefore a huge potential benefit due to excellent rates of local control and tolerability. SBRT delivers a large radiation dose to a highly localized target in a relatively small number of treatments, however, risk to normal tissue is increased. This is compounded by the current image co-registration performed with magnetic resonance imaging (MRI) and respiratory motion-managed computer-aided tomography (CT), which introduces large errors in the images. Although registration software has made great advances, the CT and MRI images are acquired using different methods of respiratory motion management. Currently, there is no MRI-compatible patient interactive breathing motion management system available, unlike for CT. Without this hardware, MRI images are time averaged over the course of imaging, while the CT images are gated to a specific phase of the respiratory cycle. Increased error leads to expanded margins around the target volume, which includes a greater volume of normal tissue. If the margins could be reduced by using only 4D MRI, then normal tissue sparing could be increased and dose escalation could be implemented to improve the probability of local tumor control.

1.2 Respiratory Motion Management

Patients with primary or metastatic cancer in the liver who are referred for SBRT, where focused high radiation dose delivery is made over a course of few treatments, typically have a diagnostic MR imaging scan. In the treatment planning stage, a four-dimensional (4D) CT scan is performed (2) or a breath-hold CT scan is conducted, if applicable (3-5), because tumors in the thorax can move significantly, up to a 5 cm range, during respiration (2, 6). Image co-registration is then performed between the MRI and respiratory motion-managed CT in the treatment position. This image fusion is often subject to significant uncertainties caused mainly by both inadequate breathing motion management during MR imaging procedures and inconsistent motion management between different imaging procedures (ie, MR scan and CT scan). Because of such uncertainties, it is common practice to generously encompass surrounding normal liver tissue in the radiation target volume to ensure adequate dose delivery to tumor cells. This practice can sometimes become a cause of surrounding normal tissue toxicity (2).

In current radiation oncology clinical practice, motion related to normal breathing is typically assessed with a single 4D CT imaging set for treatment planning. 4D CT scans use a reference respiratory cycle to sort images in each phase of the breathing motion. In reality, however, tumor motion is not the same from one cycle to another. Therefore, tumor trajectory should be taken into account as a probability density function rather than a simple deterministic function in sorting images for 4D motion. In order to accurately target the tumor at all times, the entire range of tumor motion must be captured and such cycle-to-cycle variation must be included in tumor motion management.

Accomplishing such a task requires multiple acquisitions of high quality images, which is not applicable to conventional 4D CT simulation due to excessive imaging radiation doses and inferior soft tissue contrast. Contrary to CT, MRI is free from ionizing radiation risk and provides superior soft tissue characteristics. MRI is generally believed to be a de facto

standard in soft tissue imaging. Unfortunately, however, 4D MR imaging has not been implemented in current clinical practice because existing non-optimized procedures degrade image quality and lengthen scan time by approximately 30 minutes/4D MR scan compared to approximately 5 minutes/4D CT scan. In addition, there has been no clear and concerted effort made in establishing an optimal and practical procedure for MR imaging without degrading image quality.

We have recently demonstrated that patient interactive respiratory motion management can be utilized in medical imaging techniques including MRI and CT (7-11). The feasibility of infrared camera-based respiratory motion management using the AV-aided patient interactive system was performed with healthy participants by our team using multiple 3T MRI systems (Siemens and GE MRI) and a CT system (GE CT) as shown in Figure 1. Our studies demonstrated a reduction of motion artifacts, improvement of organ motion reproducibility in MRI, a reduction of residual motion within the gating window, and an improvement of scan efficiency in CT using the AV-aided patient interactive system in conjunction with the infrared camera-external position management system.

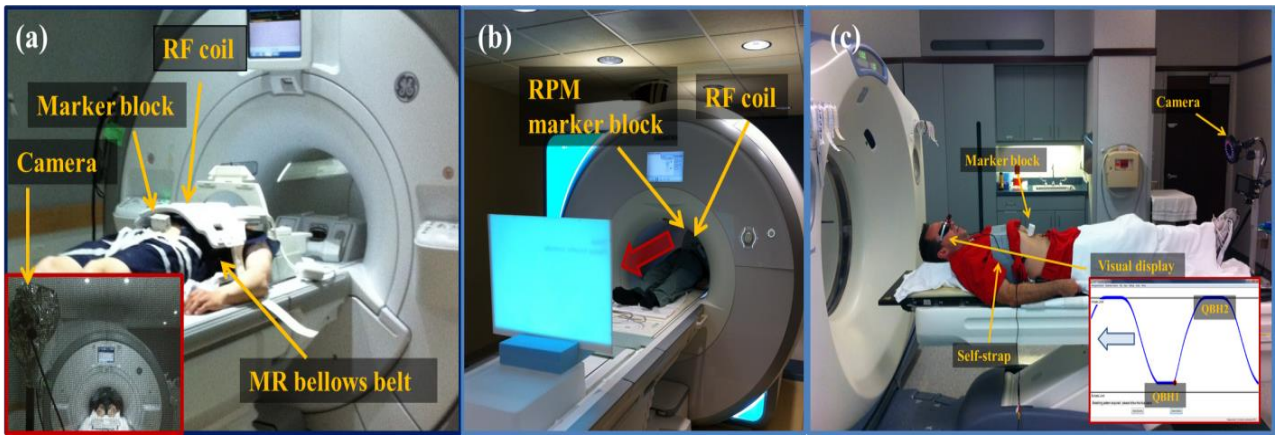

Figure 1. Infrared Camera-Based Respiratory Motion Management

Infrared camera-based respiratory motion management for healthy human participants using the AV-aided patient interactive system with (a) 3T GE MRI (b) 3T Siemens MRI and (c) GE CT systems. The system utilized an external marker position detected by an infrared camera temporarily installed at the MRI/CT room to monitor external respiratory motion and an in-house made AV-aided interactive system to guide the human participants for regular respiratory motion.

In summary, respiratory motion management provides superior image quality and accurate characterization compared to conventional free-breathing imaging techniques. Therefore, an MR-compatible patient interactive breathing motion management system will be developed in this pilot study (5, 12). Upon successful completion of this study, current practice will be improved with adequate and consistent respiratory motion management. This will facilitate accurate co-registration of MRI with CT images and improved target/organs delineation. Improved delineation will not only allow for improved targeting and increased subsequent local tumor control, but also decrease the dose to the normal surrounding tissues and risk of complications such as radiation-induced liver disease.

1.3 Optimal 4D Magnetic Resonance Imaging Acquisition Procedures

It is well known that soft tissue images of MRI are in higher quality than those of CT. Several studies, in fact, have demonstrated that MRI-based treatment planning is superior to CT-based treatment planning for liver metastases as the target is often inadequately covered with CT imaging alone, which can lead to decreased local control (13, 14).

The feasibility of real-time position management (RPM)-based retrospective 4D MR measurements with healthy human participants was tested on a 3T GE MRI with/without AV-aided patient interactive guidance by our team (Figure 2). Multiple coronal-plane 2D MR images were measured for a designated time (< 10 minutes) and 4D MR images were reconstructed using a conventional phase-based reconstruction method. Sagittal and axial-plane images were reformed from the coronal-plane images to evaluate image quality and process compliance. As shown in (b) and (c), irregular respiratory motion affected image quality on sagittal and axial-plane images (dark stripes on the images) with free breathing. In contrast, the RPM-based 4D MR measurement with AV-aided patient interactive guidance regulated respiratory motion, increasing image quality and process compliance in 4D MR measurement as shown in (d).

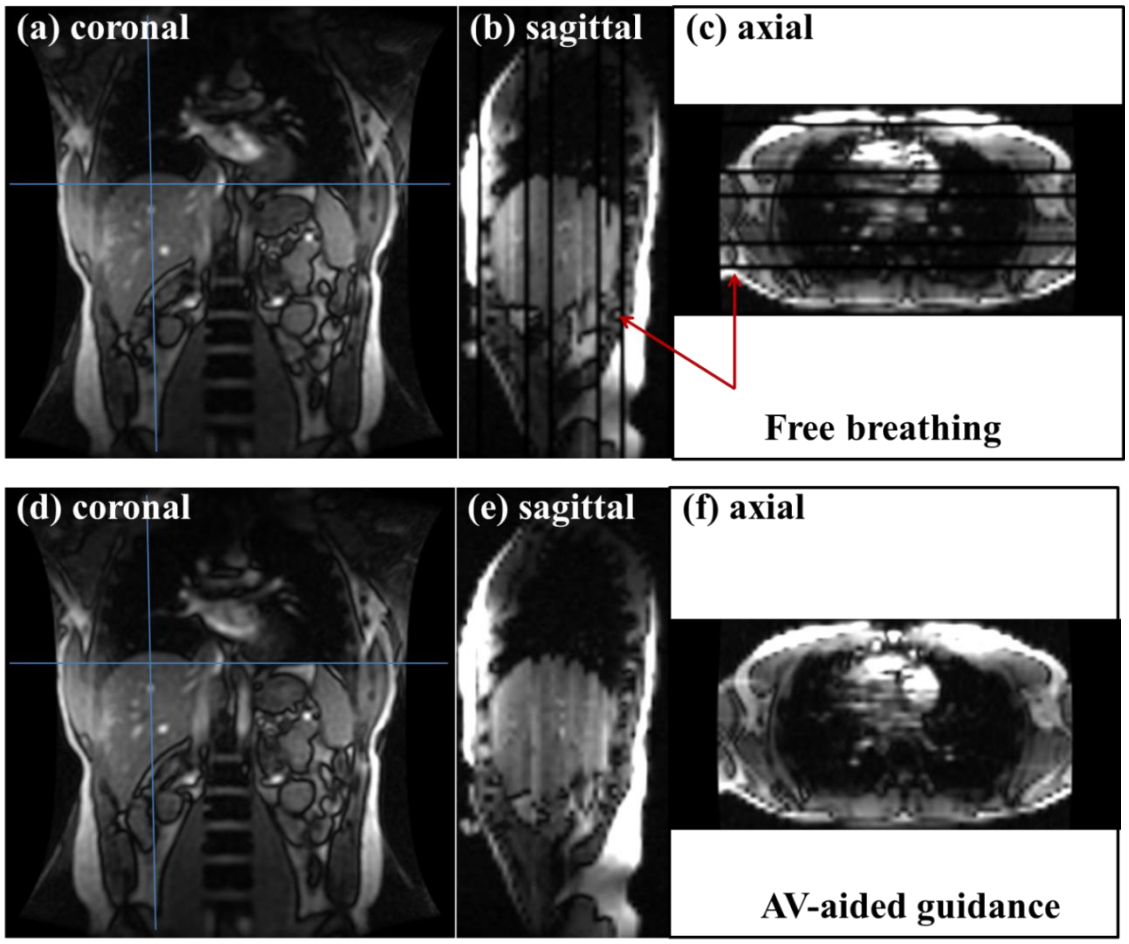

Figure 2. RPM-based 4D MRI of a Healthy Volunteer

RPM-based 4D MRI of a healthy volunteer with free breathing as presented in (a), (b), and (c) and with AV-aided interactive motion management system as shown in (d), (e), and (f): Multiple coronal-plane 2D MR images were measured for a designated time and 4D MR images were reconstructed using the conventional phase-based reconstruction method. Sagittal and axial-plane images were reformed from the coronal-plane images. The blue cross lines in (a) and (d) indicate the reformed image planes. The red arrows in (b) and (c) indicate the missing data from the coronal plane.

However, the preliminary results have not been optimized, so image quality and acquisition time can be further improved through procedure optimization including pulse sequence selection, repetition time (TR), echo time (TE), acquisition mode, and reconstruction technique. Studies will be performed to achieve optimal 4D MR configurations with the AV-aided patient interactive motion management system described in Section 6.1. Upon successful completion of this pilot study, the current practice with 4D CT scan for tumor motion evaluation can be changed to 4D MRI scan-based enabling more precise tumor identification. This will facilitate more accurate and consistent target delineation, which would ultimately translate into better local control and less treatment toxicity.

1.4 Purpose-Oriented Sampling Approach for 4D Magnetic Resonance Imaging

Tumor motion is not the same from one breathing cycle to another (2, 6). In order to irradiate the tumor at all times, the entire range of tumor motion including cycle-to-cycle variation must be included in radiotherapy, which requires a large number of 4D imaging scans to extract reliable statistical behavior of tumor motion. However, conventional 4D CT simulation is not applicable for this purpose due to excessive imaging radiation doses and inferior imaging quality. Obviously, MRI, having no associated radiation dose, has great potential for this purpose. However, even though there is a huge benefit in using MRI, a conventional single 4D MRI acquisition would take about 30 minutes, so it is not appropriate for multiple acquisitions of images under current practice.

An illustration of 2D tumor motion studied by our team is shown in Figure 3. In order to irradiate the tumor at all times, the entire range of tumor motion must be utilized and such cycle-to-cycle variation must be included in tumor motion management.

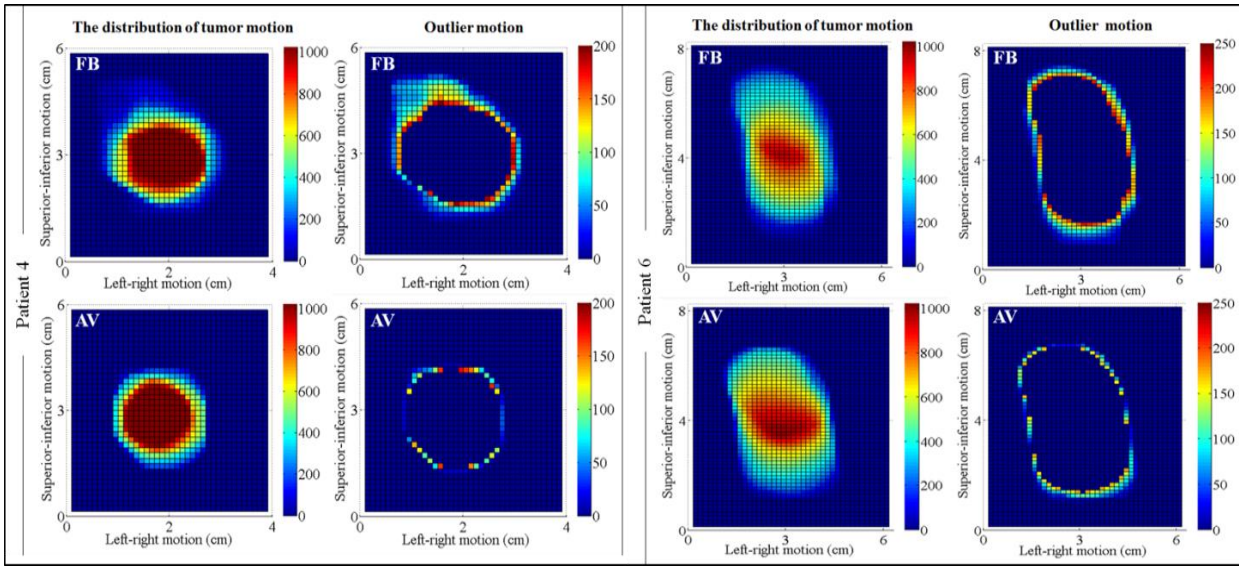

Figure 3. Distribution of Tumor Motion and Outlier Motion for Patients with Lung Cancer

The color bar scale indicates the ratio of the distribution of tumor motion.

Upon completion of the breathing motion management system, we will further develop 4D MR imaging strategies to take cycle-to-cycle variation into account for target definition. To achieve this goal, we will use a purpose-oriented sampling approach (PoSA) which provides statistical information of tumor motion over each breathing cycle. The developed 4D MRI simulation should be fast enough to acquire multi-respiratory cycles of the tumor motion (< 5 minutes), enabling the use of 4D MRI for the establishment of a statistical model of tumor motion under a reasonably acceptable time frame in the clinic. Specifically, we will develop a PoSA for confidence-weighted target definition based on a sectional-view-aided pseudo-4D MRI (SAP-4D MRI).

1.5 Diffusion Tensor Imaging and Magnetic Resonance Elastography

An optimized set of diffusion tensor imaging (DTI) and magnetic resonance elastography (MRE) acquisition parameters for application to liver SBRT is not currently available, but is proposed in this study. Once these parameters have been determined they may be evaluated against the conventional MR-based assessment tools for tissue characterization.

1.5.1 Diffusion Tensor Imaging

Diffusion-weighted imaging (DWI) MRI of diseased livers has been extensively used in clinical practice because it offers noninvasive indirect assessment of microstructure and microcirculation using microscopic diffusion of water molecules. For example, ADC has been used as a practical MR parameter to identify liver tumors , fibrosis, and inflammation (15). Furthermore, DWI has been included in a radiotherapy assessment MRI protocol in addition to conventional MRI techniques (16). ADC from DWI, however, is insensitive to the characteristics of diffusion in anisotropic environments, and diffusion in heterogeneous tumors is not well identified. Therefore, DTI with additional diffusion gradients (DWI: 3 directions and DTI: 6 or more directions) has been introduced to obtain more precise ADC calculation and information on anisotropic diffusions and orientations. DTI requires long scan time and can be adversely affected by motion which is why the utilization of DTI has been limited mainly to brain imaging where patient motion is minimal. Once the motion management technique is established, we believe DTI can be applied to liver regions. Before practical utilization of DTI on liver regions, however, DTI acquisition procedures must be optimized with scan parameters, scan time, the number of diffusion gradient directions, and image quality.

1.5.2 Magnetic Resonance Elastography

Another useful MR technique for liver disease is MRE. MRE is an emerging clinical technique to assess chronic liver diseases because it offers noninvasive assessment of mechanical properties of tissue such as tissue stiffness (elastograms) (17, 18). Because stiffness of a diseased liver increases with the development of fibrosis, MRE can be used in clinical practice to assess liver fibrosis and cirrhosis instead of using a needle biopsy. It can be a reliable and noninvasive tool for assessing hepatic fibrosis. In addition, several studies found that MRE can be used to characterize hepatic tumors because the stiffness of malignant liver tumors is considerably different than that of benign tumors. MRE, a highly advanced technology, is available at VCU to support the MRE protocol in clinical research. MRE is obtained in multiple sessions, thus, parameter optimization of MRE with consistent motion management is also needed before its practical utilization for liver regions.

In this pilot study, the optimal DTI and MRE acquisition procedures will be first provided for liver SBRT in terms of MR pulse sequence parameters, image analysis, and assessment tools such as diffusivity maps and elastograms. In the evaluation, the proposed assessment tools from DTI and MRE will be compared with conventional MR-based assessment tools on tissue characterization. Upon successful completion of this pilot study, we will have novel tools to quantitatively assess liver tumors, thus providing clinicians with the ability to functionally distinguish between healthy and tumor tissues.

1.6 Proposed MR Procedures

The proposed MR imaging procedures combined with the AV-aided patient interactive system is illustrated schematically in Figure 4.

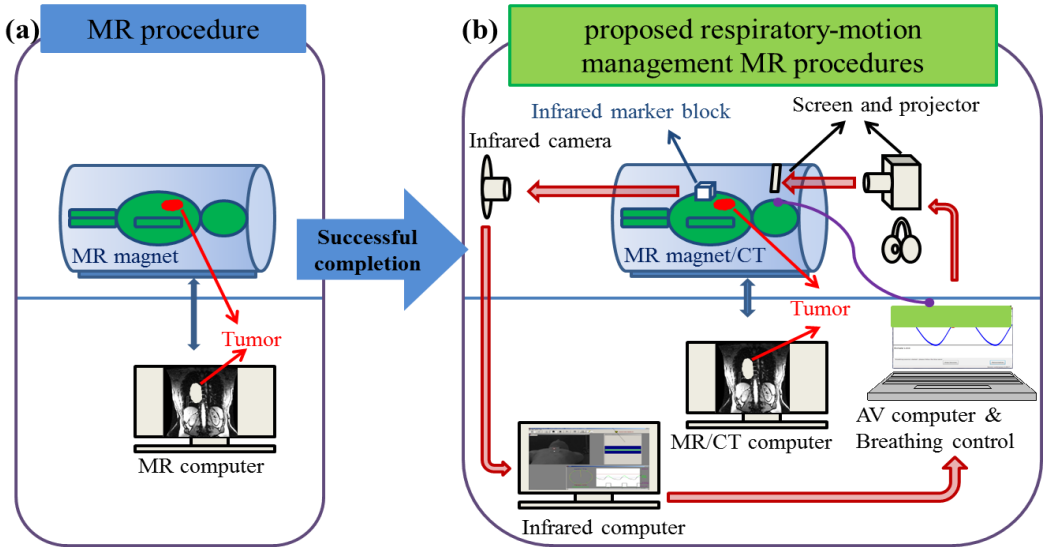

Figure 4. Schematic of Respiratory Motion Management System-based MRI Procedures

(a) Current 3D MRI procedures; (b) Proposed MRI procedures combined with AV-aided patient interactive guidance with MR compatibility

1.7 Known and Potential Risks and Benefits

1.7.1 Risks

It is possible that participants in the MRI phases of the study may experience claustrophobia-related anxiety. There are no other anticipated risks associated with the strategies planned in this feasibility study.

1.7.2 Benefits

Upon successful completion of this pilot study, the following will be established: 1) an audiovisual-aided patient interactive respiratory motion management system for imaging and radiation treatment; 2) optimized 4D MRI procedures under consistent breathing; and 3) optimized DTI and MRE procedures under consistent breath-hold for radiotherapy planning. The potential benefits include:

- Reduction in tumor motion variation among the various medical procedures using the proposed patient interactive respiratory motion management system
- Image artifact reduction
- More accurate and consistent tumor localization with consistent breathing control
- Precise delineation of tumors and normal tissues in radiotherapy

2 OBJECTIVES

2.1 Primary Objectives

2.1.1 To develop an MR-compatible audiovisual (AV)-aided patient interactive breathing motion management system

2.1.2 To develop optimized MRI procedures for 4D and multiparametric MRIs with the assistance of an MR-compatible audiovisual (AV)-aided patient interactive breathing motion management system

2.2 Secondary Objectives

2.2.1 To establish optimal DTI and MRE acquisition procedures with the AV-aided patient interactive motion management system and 4D motion phantom

2.2.2 To compare DTI and MRE acquisition from participants with primary or metastatic cancer in the liver to conventional MRI acquisition metrics

2.2.3 To compare DTI and MRE acquisition from participants with primary or metastatic cancer in the liver to the DTI and MRE results of the healthy participants

2.2.4 To develop a SAP-4D MRI acquisition to obtain multi-dimensional statistical tumor motion information for confidence-weighted target definition

3 STUDY DESIGN

3.1 General Description

The purpose of this pilot study is to develop MRI-compatible systems and procedures to optimize SBRT treatment planning. During the first phase of the study, an in-room patient interactive motion management system will be developed and its feasibility will be evaluated.

In the second phase, MR imaging on a 4D motion phantom will be performed. Using a 4D motion phantom provides a standard to generate optimal imaging and image analysis parameters before evaluating the procedures with healthy participants who have an unknown set of contrast and motion values. Following completion of MR imaging with the MRI-compatible patient interactive breathing motion management system in healthy participants, MR imaging will be conducted with participants who have primary or metastatic cancer in the liver. The results from healthy participants will be used for comparison with the results from the participants with cancer in the liver to evaluate how healthy and unhealthy liver structure varies. All of the human scans will be conducted using the AV-aided patient interactive motion management system to reduce variation in breathing motion.

3.2 Investigational Device

This feasibility study includes the development of a breathing motion management system. A component of this system is a non-significant risk (NSR) investigational device which is

illustrated in Part B of Figure 5.
MCC-16-13073 study will be conducted according to the abbreviated investigational device exemption (IDE) requirements of the Food and Drug Administration [21 CFR 812.2(b)].

3.3 Cohort Definitions

The study plan will be carried out with 4 participant cohorts.

- **Cohort A**: Healthy participants who will have photographs and/or videos taken of their dental structure and oral cavity (Section 6.1.3)
- **Cohort B**: Healthy participants who will test the effectiveness of the respiratory motion management system (Section 6.1.4)
- **Cohort C**: Healthy participants who will have MRI scans of the torso while using the MRI-compatible in-room patient interactive respiratory motion management system mouthpiece and breathing device (Sections 6.2.2 and 6.3)
- **Cohort D**: Patients with primary or metastatic cancer in the liver who require SBRT will have MRI scans of the torso using the MRI-Compatible In-Room Patient Interactive Respiratory Motion Management System (Sections 6.4.2 and 6.5)

3.4 Study Accrual

A maximum total of 33-47 participants will be enrolled in the study. Because healthy participants may be enrolled in more than one of the 3 healthy participant cohorts, the total number of participants may be fewer than 33.

Accrual in the 4 cohorts will be:

- Cohort A: 15-20 healthy participants
- Cohort B: 10-15 healthy participants
- Cohort C: 4-6 healthy participants
- Cohort D: 4-6 participants with primary or metastatic cancer in the liver who are candidates for SBRT

3.5 Primary Endpoints

3.5.1 Variation in breathing motion of the MR-compatible AV-aided patient interactive motion management system when compared to free breathing and the Elekta ABC system currently used in clinical practice during CT scans

3.5.2 The acquisition speed and image accuracy provided by the optimized 4D MRI, DTI, and MRE image parameters developed in this pilot study compared to current clinical MR-based assessment tools for tissue characterization and motion monitoring

3.6 Secondary Endpoints

3.6.1 Optimal DTI and MRE acquisition procedures with the AV-aided patient interactive motion management system with a 4D motion phantom

3.6.2 DTI and MRE acquisition from participants with primary or metastatic cancer in the liver compared to conventional MRI acquisition metrics

3.6.3 DTI and MRE acquisition from participants with primary or metastatic cancer in the liver compared to the DTI and MRE results of the healthy participants

3.6.4 SAP-4D MRI acquisition to generate multi-dimensional statistical tumor motion information based on 2 orthogonal 2D-cine MRIs for confidence-weighted target definition

4 PARTICIPANT SELECTION

The inclusion and exclusion criteria are specific for each of the 4 participant cohorts. Descriptions of the 4 cohorts are provided in Section 3.3 and the cohort-specific research activities are described in Section 6.

Refer to Sections 4.1 and 4.2 for Cohort A; Sections 4.3 and 4.4 for Cohort B; Sections 4.5 and 4.6 for Cohort C; and Sections 4.7 and 4.8 for Cohort D.

Note: Healthy participants may be enrolled in more than one of the 3 cohorts for healthy participants (ie, Cohorts A, B, and C) assuming that the participant is eligible and has signed the cohort-specific consent form.

4.1 Inclusion Criteria for Healthy Participants – Cohort A

Healthy individuals being considered for participation in **Cohort A** must meet all of the following inclusion criteria to be eligible to participate in this pilot study.

4.1.1 Age ≥ 18 years

4.1.2 Karnofsky Performance Status score of ≥ 70 % (see Appendix 2 for KPS criteria)

4.1.3 Ability to understand and the willingness to sign a written informed consent document

4.2 Exclusion Criteria for Healthy Participants – Cohort A

Individuals who meet any of the following **Cohort A** exclusion criteria are ineligible to participate in this pilot study.

4.2.1 Dentures

Note: Individuals with dental bridges, implants, and crowns should not be excluded.

4.2.2 Medical, psychological, or social condition that, in the opinion of the investigator, may increase the participant's risk or limit the participant's adherence with study requirements

4.3 Inclusion Criteria for Healthy Participants – Cohort B

Healthy individuals being considered for participation in **Cohort B** must meet all of the following inclusion criteria to be eligible to participate in this pilot study.

4.3.1 Age ≥ 18 years

4.3.2 Karnofsky Performance Status score of ≥ 70 % (see Appendix 2 for KPS criteria)

4.3.3 Ability to maintain breath hold for at least 20 seconds repeatedly (ie, approximately 10 repetitions with breaks of about a minute between each)

Note: The patient's ability to maintain breath hold for 20 seconds should be demonstrated to determine eligibility. Repeating the breath hold for 10 repetitions is not required for eligibility screening.

4.3.4 Ability to understand and the willingness to sign a written informed consent document

4.4 Exclusion Criteria for Healthy Participants – Cohort B

Individuals who meet any of the following **Cohort B** exclusion criteria are ineligible to participate in this pilot study.

4.4.1 Respiratory conditions (eg, asthma) or illnesses that are symptomatic (eg, upper respiratory infection) that will affect participation in Cohort B study requirements

4.4.2 Medical, psychological, or social condition that, in the opinion of the investigator, may increase the patient's risk or limit the patient's adherence with study requirements

4.5 Inclusion Criteria for Healthy Participants – Cohort C

Healthy individuals being considered for participation in **Cohort C** must meet all of the following inclusion criteria to be eligible to participate in this pilot study.

4.5.1 Age ≥ 18 years

4.5.2 Karnofsky Performance Status score of ≥ 70 % (see Appendix 2 for criteria)

4.5.3 Determination that the patient is an acceptable candidate for an MRI at the CARI facility (see Section 6.6.2)

4.5.4 Ability to lie flat for about 2 hours

4.5.5 Ability to maintain breath hold for at least 20 seconds repeatedly (ie, approximately 10 repetitions with breaks of about a minute between each breath hold)

Note: The patient's ability to maintain breath hold for 20 seconds should be demonstrated to determine eligibility. However, repeating the breath hold for 10 repetitions is not required to determine eligibility.

4.5.6 A woman of childbearing potential, defined as a woman who is < 60 years of age and has not had a hysterectomy, must have a documented negative pregnancy test within 14 days prior to the pilot study MRI

4.5.7 Ability to understand and the willingness to sign a written informed consent document

4.6 Exclusion Criteria for Healthy Participants – Cohort C

Individuals who meet any of the following **Cohort C** exclusion criteria are ineligible to participate in this pilot study.

4.6.1 Respiratory conditions (eg, asthma) or illnesses that are symptomatic (eg, upper respiratory infection) that will affect participation in Cohort C study requirements

4.6.2 Requirement for sedation or anti-anxiety medications to manage MRI-related claustrophobia

4.6.3 Pregnancy

4.6.4 Medical, psychological, or social condition that, in the opinion of the investigator, may increase the patient's risk or limit the patient's adherence with study requirements

4.7 Inclusion Criteria for Patients with Cancer in the Liver – Cohort D

Patients being considered for participation in **Cohort D** must meet all of the following inclusion criteria to be eligible to participate in this pilot study.

4.7.1 Age ≥ 18 years

4.7.2 Karnofsky Performance Status score of ≥ 70 % (see Appendix 2 for criteria)

4.7.3 Documented primary cancer in the liver or liver metastases from any solid tumor

4.7.4 Determination by the treating radiation oncologist that the patient is a candidate for SBRT to tumor(s) in the liver

4.7.5 Determination that the patient is an acceptable candidate for an MRI at the CARI facility (see Section 6.6)

4.7.6 Ability to lie flat for about 2 hours

4.7.7 Ability to maintain breath hold for at least 20 seconds repeatedly (ie, approximately 10 repetitions with breaks of about a minute between each breath hold)

Note: The patient's ability to maintain breath hold for 20 seconds should be demonstrated to determine eligibility. However, repeating the breath hold for 10 repetitions is not required to determine eligibility.

4.7.8 A woman of childbearing potential, defined as a woman who is < 60 years of age and has not had a hysterectomy, must have a documented negative pregnancy test within 14 days prior to the pilot study MRI

4.7.9 Ability to understand and the willingness to sign a written informed consent document

4.8 Exclusion Criteria for Participants with Cancer in the Liver – Cohort D

Patients who meet any of the following **Cohort D** exclusion criteria are ineligible to participate in this pilot study.

4.8.1 Respiratory conditions (eg, asthma) or illnesses that are symptomatic (eg, upper respiratory infection) that will affect participation in Cohort D study requirements

4.8.2 Requirement for sedation or anti-anxiety medications to manage MRI-related claustrophobia

4.8.3 Pregnancy

4.8.4 Medical, psychological, or social condition that, in the opinion of the investigator, may increase the patient's risk or limit the patient's adherence with study requirements

5 STUDY ENTRY AND WITHDRAWAL PROCEDURES

5.1 Study Entry Procedures

5.1.1 Required Pre-Registration Screening Tests and Procedures

Refer to the appropriate cohort-specific study calendar in Section 8 for the screening tests and procedures that are required prior to registration and for the timing of these events relative to the start of the study intervention.

5.1.2 Registration Process

Study registration will be performed by the study team (email: masseyradonc@vcu.edu). The following documents are required for study registration:

- Completed registration cover sheet
- Completed, signed, and dated eligibility checklist
- Signed and dated consent form

The registrar will complete the registration process by assigning a study ID number and forwarding the "Confirmation of Registration" form to the registering study team. The study intervention may not begin until the Confirmation of Registration has been received and a study ID number has been assigned.

The study team will enter the patient's initial enrollment data (eg, demographics, consent, eligibility) into the OnCore database following study registration (before study procedures are initiated).

5.2 Study Withdrawal Procedures

A participant, either a healthy participant or a patient with primary or metastatic cancer in the liver, may decide to withdraw from study participation at any time. Participants must be removed from the study when any of the following occurs:

- The participant has withdrawn consent for the cohort-specific study procedures
- If, in the investigator's opinion, continuation of the cohort-specific study requirements would be harmful to the participant's well-being
- The participant cannot be contacted prior to completing study requirements
- The sponsor has terminated the study

The reason for and date associated with study withdrawal or removal from the study must be documented in source documents and in the OnCore database.

6 STUDY PROCEDURES/EVALUATIONS

6.1 Development of MRI-Compatible In-Room Patient Interactive Respiratory Motion Management System

6.1.1 Overview

We will utilize our previous motion management experience to develop an MRI-compatible in-room patient interactive respiratory motion-management system with the Philips 3 Tesla (3T) MRI located at and in cooperation with the Collaborative Advanced Research Imaging (CARI) facility. The participant's abdominal position from an infrared camera will be fed into the breathing management system to control the participant's breathing motion. Under this control, participants will be guided for regular breathing or breath-holding at designated levels and times during MR imaging.

In Figure 5 (a) and (b), a mouthpiece of the Active Breathing Coordinator (ABC) System from Elekta, which is currently used in radiotherapy, is presented. Due to its unsatisfactory connectivity and patient discomfort, significant modification of the mouthpiece is required. Our dentistry team will develop an improved connection mechanism for the breathing control system that will offer improved patient comfort as well as more secure airflow control as illustrated in (b), (c), and (d). The mouthpiece in (b) will be replaced with the novel thru-mouth-breathing airflow control mouthpiece developed by our dentistry team. The same guidance for breathing control will be tested in the planning CT scan procedure and radiotherapy in the VCU Radiation Oncology Department.

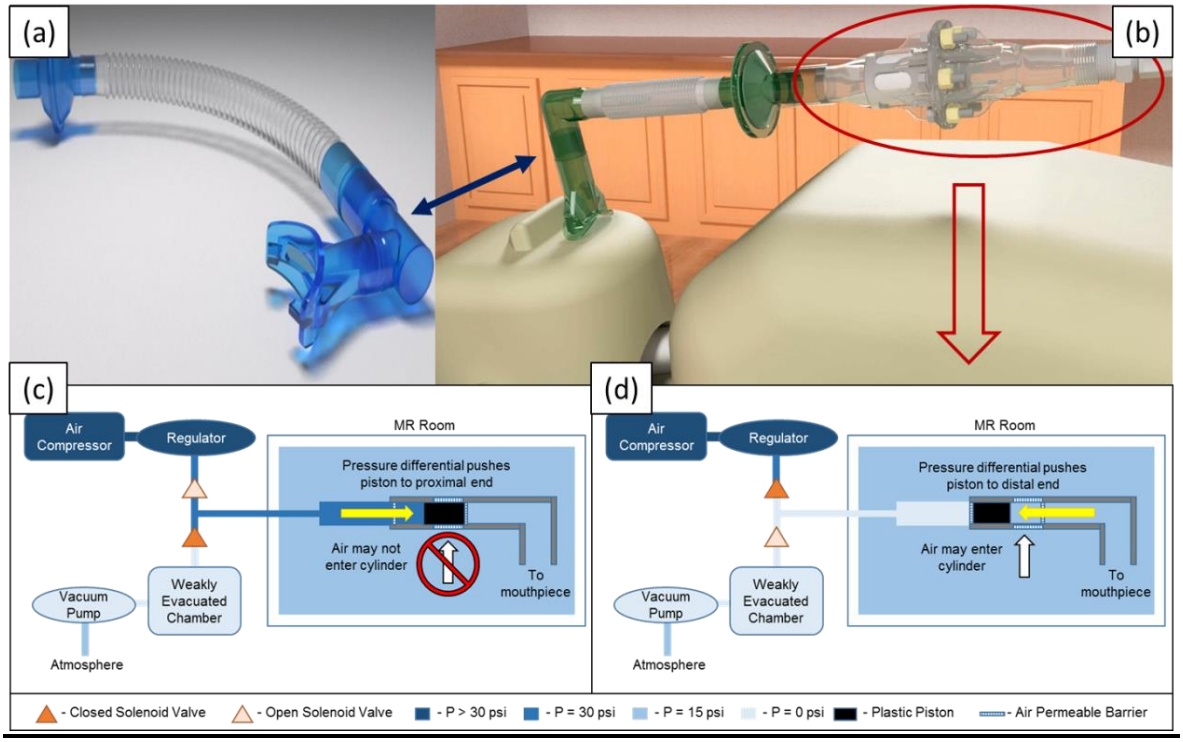

Figure 5. Proposed Respiratory Tubing System

The system utilizes pneumatic power and MR-compatible materials in a piston form to control respiratory motion. An in-house AV-aided interactive system will be used to guide participants in achieving regular respiratory motion. (a) Commercial mouthpiece (arrow) connected to a respiratory tube from Elekta; (b) demo sketch of the proposed system; the circle indicates the schematic of the breath-hold control system driven by pneumatic power; (c-d) schematic of breath-hold control mechanism in detail

6.1.2 Components

The following components will be integrated to create the MRI-compatible in-room patient interactive respiratory motion management system:

6.1.2.1 Dentistry Team

The dentistry team will design, simulate, conduct 3D printing, polish, and test the physical/mechanical properties of the following:

- Mouthpiece component as described in Section 6.1.1; a patient-adaptive, stable, and tightly sealed thru-mouthpiece will be developed to replace the current clinical device from Elekta (Figure 5).
- Non-metallic (ie, MR-safe) airflow control device which will be driven by pneumatic power. The air-chamber and piston will be simulated and 3D-printed. Responding time will be tested with designated pneumatic power (pressure).

6.1.2.2 Radiation Oncology Team

The radiation oncology team will design, simulate, assemble and test all of the devices:

- Breathing control device (investigational device developed by the Sponsor-Investigator)
- Motion monitoring device using an infrared camera to monitor the breathing motion
- Safety device using optic fiber technique so that the patient can communicate with the clinical staff if the patient cannot tolerate the involuntary breath-hold control

6.1.3 Research Assessments for **Participants in Cohort A**

A total of 10-15 healthy participants will be enrolled in Cohort A. The procedures described below will be performed.

- Participants will have photos taken and/or a video filmed of their dental structure and oral cavity. This oral assessment will take place in the VCU Radiation Oncology Department. (The participant's face will not be included in the photographs or video images.)
- Multiple preliminary prototypes with differences in size, shape, and function will be created through computer-aided design (CAD). These will be 3D-printed using biocompatible resin.

6.1.4 Research Assessments for **Participants in Cohort B**

A total of 10-15 healthy participants will be enrolled, and the following procedures will be performed.

- An optimized mouthpiece prototype will be selected for the participant based on mouth size (eg, small, medium, or large) or other criteria.
- The novel non-metallic thru-mouth breathing airflow control system will be tested. This system (the "MRI-Compatible In-Room Patient Interactive Respiratory Motion Management System") combines the selected optimized mouthpiece and an airflow control device that utilizes pneumatic power and electronic control.
- Breathing traces with and without the MRI-Compatible In-Room Patient Interactive Respiratory Motion Management System will be recorded during assessments in the VCU Radiation Oncology Department to test the effectiveness of the MRI-Compatible In-Room Patient Interactive Respiratory Motion Management System. The data will be analyzed in terms of the RMSE of displacement and period for breathing motion regularity. (There will be no imaging acquisition during this process.)

6.2 Optimization of 4D MRI Acquisition Procedures

Studies will be performed to achieve optimal 4D MR configurations with the AV-aided patient interactive motion management system described in Section 6.1.1.

6.2.1 Procedure Optimization with the 4D Motion Phantom

- MRI pulse sequence optimization to improve image quality and process compliance
- Image reconstruction development in cooperation with pulse sequence to improve image quality and calculation time
- 4D MRI pulse sequence optimization and image reconstruction development with the 4D motion phantom

6.2.2 Research Assessments for **Participants in Cohort C**

Upon completion of the procedure optimization using the 4D motion phantom, a total of 4-6 healthy participants will be enrolled and will have 2 research MRIs. The MRI scans performed as part of this study are for research purposes only. These scans are not diagnostic and cannot be used for any medical or diagnostic purposes.

6.2.2.1 MRI Screening Process

- An MRI safety survey will be completed to establish eligibility for having MRI scans at the CARI facility (Section 6.6)
- A urine pregnancy test will be performed for WCBP prior to each MRI.

6.2.2.2 MRI Scans

4D MRI images of the torso will be acquired using the optimized 4D MRI pulse sequences with the AV-aided interactive motion management system. The MRIs will be performed at the CARI facility at the following 2 time points:

- Within 3 weeks following study registration
- Within 1 to 4 weeks following the first study-required MRI

6.2.2.3 Incidental Finding on Research MRI Scan

As noted previously, the scans performed at the CARI facility are research, not diagnostic, scans and can only be used for research purposes. However, if an incidental finding is noted on the research images of a healthy participant in Cohort C, a VCU radiologist will be asked to review the research images to provide additional information, if possible. The finding will be communicated to the Cohort C participant by the study physician (ie, co-investigator), and recommendations for follow-up with the participant's primary care physician (PCP) will also be discussed. If the participant is not in the care of a PCP or other physician, the study team will assist the participant in arranging for appropriate follow-up.

6.3 Optimization of DTI and MRE Acquisition Procedures

Studies will be performed to achieve optimal DTI and MRE acquisition procedures with the AV-aided patient interactive motion management system for active breath-hold. These studies will be conducted in healthy participants (Cohort C) who will have MRI scans at CARI as described in Section 6.2.2.

6.3.1 Procedure Optimization with the 4D Motion Phantom with Designated Diffusivity and Stiffness Properties

- DTI and MRE pulse sequence optimization to improve image quality and process compliance eg, imaging parameters/the number of diffusion gradient directions (for DTI) and the frequency of the applied waves/motion-encoding gradient (for MRE)
- ADC map and elastogram analysis development

6.3.2 Feasibility Tests in Healthy Participants

Upon completion of the DTI procedure optimization using the 4D Motion Phantom (with designated diffusivity and stiffness properties), the following feasibility tests will be performed:

- DTI and MRE images will be acquired using the optimized pulse sequences with the AV-aided interactive motion management system for active breast-hold.
- ADC map and elastogram analysis of the healthy participants will be evaluated and determined as the reference of healthy tissue.

6.4 Development of the Purpose-Oriented Sampling Approach for the Supportive 4D MRI

Studies will be performed to develop the PoSA for the supportive 4D MRI. A SAP-4D MRI will be conducted to obtain multidimensional statistical tumor motion information based on 2 orthogonal 2D cine MRIs for confidence-weighted target definition.

6.4.1 SAP-4D MR Imaging with the 4D Motion Phantom

- Two orthogonal cine 2D MR images in multi-respiratory cycles (approximately one minute/plane) will be acquired with < 200ms sampling time/frame monitored with the patient interactive motion management system. Statistical tumor trajectory will be obtained using both internal position information from 2D MR images and external position information from the respiratory monitoring system. The target identified in the reference 4D MR images will be superimposed on the statistical tumor trajectory to define a confidence-weighted target.
- In evaluation, the statistical target definition obtained from SAP-4D MRI will be compared with the target trajectory from the reference 4D MR images.

6.4.2 Research Assessments for **Participants in Cohort D**

The feasibility of the method established in the phantom study will be evaluated with 4-6 participants who have primary or metastatic cancer in the liver.

The scans performed as part of this study will not be diagnostic scans and cannot be used for any medical or diagnostic purposes. These research scans will also not be used for SBRT treatment planning. Therefore, the imaging conducted will have no influence on patient treatment.

6.4.2.1 MRI Screening Process

- An MRI safety survey will be completed to establish eligibility for having MRI scans at the CARI facility (Section 6.6)
- A urine pregnancy test will be performed for WCBP prior to each MRI.

6.4.2.2 MRI Scan Time Points

4D MRI images of the torso will be acquired using the optimized 4D MRI pulse sequences with the AV-aided interactive motion management system. The MRIs will be performed at the CARI facility at the following 2 time points:

- Within 3 weeks following study registration but must be before SBRT is initiated
- Within 1 to 4 weeks following the last SBRT treatment

6.4.2.3 MRI Acquisition Procedures

- Patient simulation will be made under AV-aided patient interactive guidance. The reference 4D MR images will be acquired for target identification. Two orthogonal cine 2D MR images over multi-respiratory cycles will be acquired with < 200 ms sampling time/frame. The target identified in the reference 4D MR images will be superimposed on the statistical tumor trajectory to define a confidence-weighted target.
- If the required image acquisition time for appropriate image quality is >200 ms, the internal respiratory position (eg, diaphragm) from 2D images will be determined based on the external position information from the respiratory monitoring system to obtain the entire range/probability of tumor motion. Regarding the internal-external respiratory motion correlation, our team reported the strong motion correlation between the diaphragm and the abdomen under AV guidance (mean Pearson's R correlation = 0.96).
- For evaluation of the method, 1 or 2 additional 4D MR image sets, depending on the participant's condition, will be acquired for each participant with cancer in the liver. Tumor trajectories from 2 to 3 4D MR image sets will be compared with the statistical tumor trajectory obtained in the SAP-4D-MRI.

6.5 Establishment of Optimal DTI and MRE Acquisition with Participants Who Have Cancer in the Liver

To establish DTI and MRE acquisition with 4-6 participants with cancer in the liver in addition to conventional MR tools, the following procedures will be conducted with **Cohort D Participants** (see Section 6.4.2 for additional information regarding Cohort D and Section 6.6 regarding MRI scans at CARI):

- DTI and MRE procedure optimization with actual patients will be performed in addition to conventional MRI acquisition such as T1-weighted (T1w) and T2-weighted (T2w) MRI.
- Optimizing ADC map and elastogram analysis will be performed in cooperation with imaging parameters and acquisition.
- Diffusivity maps and elastrograms of the participants with cancer in the liver will be processed to compare to those of the healthy participants.
- The regions of interest (ROIs) in healthy tissues and tumors identified in the reference 3D MR images of the participants with cancer in the liver will be analyzed in terms of the diffusivity maps and the elastograms to determine the correlation of the diffusivity and elasticity with tissue types.

6.6 MRI Scans at CARI for Participants in Cohorts C and D

6.6.1 General Information

- The research MRI scans in this study will be performed at the VCU CARI facility:

  VCU Collaborative Advanced Research Imaging (CARI) Program
  203 East Cary Street
  Richmond, VA 23219
  804-828-3639

- The MRI scans performed in this study **impart no ionizing radiation dose.**
- Contrast material will not be used.

6.6.2 Contraindications for MRI

- Participants in Cohorts C and D will be assessed prior to study registration for MRI contraindications using the VCU Health System MRI Safety Checklist.
- After the cohort-specific consent form has been signed, the study team will assist the participant in completing the MRI Safety Checklist or, if a previously completed MRI Safety Checklist is available, the study team will review the checklist with the participant and update, as needed. The completed/updated checklist will be provided by the study team to the CARI facility staff for review to identify any contraindications that would prevent performing the MRI. Additionally, to screen for the presence of any contraindication since the previous checklist was completed, CARI facility staff will update or complete a new MRI Safety Checklist on site within 24 hours prior to each of the MRI scans.

- Examples of contraindications include:
  - *Inability to independently move onto an MRI exam table*
  - *Need for sedation in order to proceed with the MRI*

    Individuals who are known to experience claustrophobia-related anxiety to the extent that they require sedation in order to undergo the MRI procedure will be excluded from this trial. In the event that an enrolled participant experiences new significant anxiety due to claustrophobia during the initial MRI, the CARI facility staff will notify the study team to determine if the participant will be able to undergo the second scan.
  - *Presence of ferromagnetic objects or materials*

    The presence of some pacemakers, metal or electromechanical implants, and metallic foreign bodies including some tattoo ink can lead to injury during the MRI procedure. In some cases, the duration that the metallic material has resided in the body may impact whether its presence is a contraindication to the MRI.
  - *Pregnancy*

    The risks of MRI for the fetus are unknown. Pregnant women will be excluded from participation in Cohorts C and D of this study. For WCBP, a urine pregnancy test will be performed at CARI immediately prior to each MRI.

6.7 Follow-Up

There are no follow-up requirements in this study. Study participation will conclude when the cohort-specific requirements have been completed.

7 STUDY RISKS/REPORTING UNANTICIPATED ADVERSE DEVICE EFFECTS

7.1 Unanticipated Adverse Device Effects

7.1.1 Definition of Serious Injury

A serious injury is an injury or illness that:

- Is life-threatening;
- Results in permanent impairment of a body function or permanent damage to a body structure; or
- Necessitates medical or surgical intervention to preclude permanent impairment of a body function or permanent damage to a body structure.

7.1.2 Definition of Unanticipated Adverse Device Effects

Unanticipated adverse device effect (UADE) includes any incident, experience, or outcome that meets **all of the following criteria**:

Serious adverse effect (see Section 7.1.1 for definition of serious injury) on health or safety or any life-threatening problem or death or any other unanticipated serious problem associated with a device that relates to the rights, safety, or welfare of participants

- Caused by or associated with a device
- Not previously identified in nature, severity, or degree of incidence in the investigational plan or application (including a supplementary plan/application)

7.2 Known Risks

7.2.1 Dental Assessment (Cohort A)

There are no anticipated risks associated with the dental assessment with a photo camera and/or a video camera (Section 6.1.3). The participant's face will not be included in photographs/videos.

7.2.2 Breathing Device Testing (Cohorts B, C, and D)

There are no anticipated risks associated with testing the breath motion management system (Section 6.1.4) or with use of breath motion management system during the MRIs.

7.2.3 MRI Scans (Cohorts C and D)

- Metal objects may pose a risk due to the high magnetic fields utilized. As described in Section 6.6.2, proper screening will be performed to omit individuals who are at risk due to: artificial joints, limbs, or valves, embedded bullet or shrapnel, implantable defibrillators, metal clips, pacemakers, and other metallic objects.
- Potential participants who require medication to manage claustrophobia-related anxiety during MRI scans will be excluded from participation in Cohort C or Cohort D (Sections 4.6.2 and 4.8.2), but some participants may experience MRI-related claustrophobia.

7.3 Time Period and Procedures for Reporting UADEs

- The time period required for reporting UADEs begins with the initiation of cohort-specific study procedures and ends 30 days after the final cohort-specific requirement.
- All UADEs will be recorded in MCC's OnCore Clinical Trials Management System in the OnCore Deviations domain. (Refer to Table 1 for expedited reporting requirements for UADEs.)

7.4 Expedited Reporting Requirements for UADEs

Expedited reporting is required for UADEs (defined in Section 7.1) as outlined on Table 1.

Table 1. Expedited Reporting Requirements for UADEs

Report Recipient	Requirements
Sponsor-Investigator Taeho Kim, MD Phone: 804-828-7418 Email: taeho.kim@vcuhealth.org	Report the UADE to the Sponsor-Investigator and Study Team **within 1 business day** of becoming aware of the occurrence.
Study Team Daeryl Williamson, RN, BSN Telephone: 804-628-2334 Fax: 804-628-9960 Email: masseyradonc@vcu.edu	
VCU IRB	Report any UADE that meets the criteria outlined in Section 7.1 to the IRB **within 5 business days** of becoming aware of the occurrence.
FDA	Using MedWatch Form 3500A, the Sponsor-Investigator will report to the FDA any UADE that meets the criteria outlined in Section 7.1 **within 10 business days** of the Sponsor-Investigator becoming aware of the occurrence.

8 STUDY CALENDARS

The schedule of exams, assessments, and other requirements are listed on Table 2 for Cohort A, Table 3 for Cohort B, Table 4 for Cohort C, and Table 5 for Cohort D.

Table 2. Study Calendar for **Cohort A**

Required Assessments	Within 21 Days Prior to Study Registration	Within 21 Days After Study Registration
Informed Consent (Cohort A)	X	
Demographics	X	
Performance Status (Appendix 2)	X	
Height and Weight	X	
Dental Assessment, Photographs, and Video Imaging*		X
*Conducted by the VCU School of Dentistry in the Department of Radiation Oncology (Section 6.1.3).		

Table 3. Study Calendar for **Cohort B**

Required Assessments	Within 21 Days Prior to Study Registration	Within 21 Days After Study Registration
Informed Consent (Cohort B)	X	
Demographics	X	
Performance Status (Appendix 2)	X	
Height and Weight	X	
Respiratory Assessment[A]	X	
Breathing Testing[B]		X
A. Limited to asking the potential participant to demonstrate breath hold for 20 seconds (see Section 4.3.3). B. See Section 6.1.4.		

Table 4. Study Calendar for **Cohort C**

Required Tests and Assessments	Prior to Study Registration		After Study Registration	
	Within 21 Days	**Within 14 Days**	**Within 21 Days Following Study Registration**	**Within 7-28 Days Following First MRI at CARI**
Informed Consent (Cohort C)	X			
Demographics	X			
Performance Status (Appendix 2)	X			
Height and Weight	X			
Respiratory Assessment[A]	X			
Pregnancy Test[B]		X	X[C]	X[C]
Assessment for MRI at CARI[D]	X		X[E]	X[E]
MRI of Torso[F]			X	X

A. Limited to the patient demonstrating breath hold for 20 seconds (see Section 4.5.5).

B. Only required for WCBP (see Section 4.5.6); if required, perform within 14 days prior to study registration; serum or urine pregnancy test is acceptable.

C. Pregnancy test (urine test) at this time point will be performed at the CARI facility prior to the MRI.

D. See Section 6.6.2 regarding MRI contraindications.

E. Review of MRI contraindications at CARI.

F. Research MRI at the CARI facility with the Philips 3T MRI unit (see Sections 6.2.2 and 6.6).

Table 5. Study Calendar for **Cohort D**

Required Tests and Assessments	Prior to Study Registration		After Study Registration		
	Within 21 Days	Within 14 Days	Within 21 Days Following Study Registration	Stereotactic Body Radiotherapy	Within 7-28 Days After Last SBRT Treatment
Informed Consent (Cohort D)	X				
Demographics	X				
Performance Status (Appendix 2)	X				
Height and Weight	X				
Respiratory Assessment[A]	X				
Pregnancy Test[B]		X	X[C]		X[C]
Determination that Patient is Candidate for SBRT to Liver	X				
Assessment for MRI at CARI[D]	X		X[E]		X[E]
MRI of Torso[F]			X		X

A. Limited to the patient demonstrating breath hold for 20 seconds (see Section 4.7.7).
B. Only required for WCBP (see Section 4.7.8); if required, perform within 14 days prior to study registration; serum or urine pregnancy test is acceptable.
C. Pregnancy test (urine test) will be performed at the CARI facility prior to the MRI.
D. See Section 6.6.2 regarding MRI contraindications.
E. Review of MRI contraindications at CARI.
F. Research MRI at the CARI facility with the Philips 3T MRI unit (see Sections 6.4.2 and 6.6).

9 STATISTICAL CONSIDERATIONS

9.1 Study Design

The primary goals of this pilot study are to develop a breathing motion management system, which includes an investigational device, and using this system to optimize MRI procedures needed for SBRT treatment planning for liver cancer. Phases of development and optimization will be conducted with 4 participant cohorts as defined in Section 3.3.

9.2 Sample Size/Accrual Rates

According to the preliminary results with 10 to 15 healthy participants, assuming a type I error rate of 5%, 80% power and a moderate effect size of 0.512σ for the paired differences between free breathing and respiratory motion management breathing, a sample size of 10 to 15 participants will be required. Therefore, 10 to 15 healthy participants will be recruited for the feasibility study of the motion management system.

9.2.1 Sample Size for Developing an MR-Compatible AV-aided Patient Interactive Breathing Motion Management System

The sample size for the primary objective of developing an MR-Compatible AV-aided patient interactive breathing motion management system will be 15-20 healthy participants in Cohort A and 10-15 healthy participants in Cohort B. Accrual for these 2 cohorts is expected to take about 3 months.

9.2.2 Sample Size for Developing Optimized MRI Procedures with the Assistance of an MR-Compatible AV-aided Patient Interactive Breathing Motion Management System

The sample size for the primary objective of developing optimized MRI procedures will be 4-6 healthy participants in Cohort C and 4-6 participants with primary or metastatic cancer in the liver in Cohort D. Accrual for these 2 cohorts is expected to take about 6 months.

9.3 Analysis of Primary Endpoints

The information will be summarized in a clinical study report as a result of statistical analysis. For the primary objective in this application, internal organ motion reproducibility with the respiratory motion management system will be quantified. Results will be evaluated using the RMSE method and comparison of the data between the healthy participants and the participants with primary or metastatic cancer in the liver will be performed using statistical analysis methods such as the Student t-test.

9.3.1 Cohort A

Healthy volunteers will be used to develop the mouthpiece for the breath control device. Measurements from healthy volunteers will be summarized and used to guide the specifications of the new mouthpiece to be developed.

9.3.2 Cohort B

The second phase of the study uses healthy participants to demonstrate the reproducibility of the motion management strategy. Each participant will have a positional marker on the abdominal area and the position of the subsequent breath-holds will be recorded 3 more times. Displacement from the initial position will be measured. Because the data will be repeated measures within each participant, a mixed effects model for longitudinal data will be used to estimate the within participant variation. The model for variation will be a compound symmetric covariance matrix. We expect within participant variation to be less than 3 mm which will be an acceptable demonstration of reproducibility of our strategy.

9.3.3 Cohorts C and D

The goal of the pilot study with 4-6 healthy participants (Cohort C) and 4-6 participants with primary or metastatic cancer in the liver (Cohort D) will be to optimize the MRI planning process and to develop goals for subsequent development of the treatment planning procedure. Imaging time, image outcomes, and other dosimetric parameters will be summarized and reported through their median and range of values.

9.4 Analysis of Secondary Endpoints

Results will be evaluated using the RMSE method and comparison of the data between the healthy participants and the participants with primary or metastatic cancer in the liver will be performed using statistical analysis methods such as the Student's t-test.

10 DATA AND SAFETY MONITORING

10.1 Study Team

The study team minimally consists of the Sponsor-Investigator, the research nurse, the clinical research associate, and the study biostatistician. The Sponsor-Investigator, the research nurse, and the clinical research associate will meet at least monthly to review study status; quarterly meetings will be held with the study biostatistician. This review will include, but not be limited to, reportable UADEs and an update of the ongoing study summary that describes study progress. All meetings, including attendance, are documented.

10.2 Monitoring and Auditing

Compliance specialists in the MCC Compliance Office will provide ongoing monitoring and auditing for this study.

11 REGULATORY COMPLIANCE AND ETHICS

11.1 Ethical Standard

This study will be conducted in conformance with the principles set forth in *The Belmont Report: Ethical Principles and Guidelines for the Protection of Human Subjects of Research* (US National Commission for the Protection of Human Subjects of Biomedical and Behavioral Research, April 18, 1979).

11.2 Regulatory Compliance

This pilot study will be conducted in compliance with:

- The protocol
- Federal regulations, as applicable, including: 21 CFR Part 812, Investigational Device Exemptions; 21 CFR 50 (Protection of Human Subjects/Informed Consent); 21 CFR 56 (Institutional Review Boards); and 45 CFR 46 Subparts A (Common Rule), B (Pregnant Women, Human Fetuses and Neonates), C (Prisoners), and D (Children)

11.3 Institutional Review Board

The VCU IRB will review and provide approval for the protocol, the associated informed consent documents, and recruitment materials. Any amendments to these materials must also be approved.

11.4 Informed Consent Process

Informed consent is a process that is initiated prior to the individual's agreeing to participate in the study and continues throughout the individual's study participation. Discussion of the risks and possible benefits of this pilot study will be provided to study participants and their families. Cohort-specific consent forms describing the study procedures and risks are given to the potential participant, and written documentation of informed consent is required prior to starting study participation.

Cohort-specific consent forms will be IRB-approved and the participant will be asked to read and review the appropriate document for the cohort they are considering. Upon reviewing the document, the investigator will explain the study and answer any questions that may arise. The participant will sign the cohort-specific consent document prior to any procedures being done specifically for the study. Potential participants should have the opportunity to discuss the study with their surrogates or think about it prior to agreeing to participate. A copy of the informed consent document will be given to participants for their records.

Participants may withdraw consent at any time throughout the course of the trial. The rights and welfare of participants in Cohort D will be protected by emphasizing to them that the quality of their medical care will not be adversely affected if they decline to participate in this study.

11.5 Participant Confidentiality and Access to Source Documents/Data

Participant confidentiality is strictly held in trust by the participating investigators and their staff. This confidentiality includes the clinical information relating to participants.

The study protocol, documentation, data, and all other information generated will be held in strict confidence. No information concerning the study or the data will be released to any unauthorized third party without prior written approval of the Sponsor-Investigator.

The Sponsor-Investigator will allow access to all source data and documents for the purposes of audits, IRB review, and regulatory inspections. Source documents provided for the purpose of auditing will be de-identified and labeled with the study number, participant ID, and participant initials.

The study monitor or other authorized representatives of the Sponsor-Investigator may inspect all documents and records required to be maintained by the investigator, including but not limited to, medical records (office, clinic, or hospital) for the participants in this study. The clinical study site will permit access to such records.

12 DATA HANDLING AND RECORD KEEPING

12.1 Data Management Responsibilities

The Sponsor-Investigator is responsible for: (i) the overall conduct of the investigation; (ii) ongoing review of trial data including all safety reports; and (iii) apprising participating investigators of any UADEs.

The Sponsor-Investigator is responsible for: (i) the data management; and (ii) reviewing and, if required, reporting UADEs as described in Section 7.4.

12.2 CRFs and Data Collection

MCC OnCore data management will provide standard electronic CRFs (eCRFs) and create study-specific eCRFs to be able to capture all information required by the protocol. The eCRFs will be approved by the study team to ensure the most effective data acquisition.

Data will be entered into MCC's OnCore database on an ongoing basis. The Coordinating Study Team will review electronic data submissions periodically for data timeliness and accuracy. All eCRFs should be completed and available for collection within a timely manner, preferably no more than 14 days after the participant's visit.

The investigator(s) and study coordinator must maintain source documents for each participant in the study. All information on eCRFs will be traceable to these source documents, which are generally maintained in the participant's file.

12.3 Study Record Retention

As applicable, study records will be maintained a minimum of 5 years beyond the publication of any abstract or manuscript reporting the results of the protocol.

13 REFERENCES

1. Siegel RL, Miller KD, Jemal A. Cancer statistics, 2017. *CA Cancer J Clin*. 2017; 67:7-30.
2. Keall PJ, Mageras GS, Balter JM, Emery RS, Forster KM, Jiang SB, Kapatoes JM, Low DA, Murphy MJ, Murray BR, Ramsey CR, Van Herk MB, Vedam SS, Wong JW, Yorke E. The management of respiratory motion in radiation oncology report of aapm task group 76. *Med Phys*. 2006; 33:3874-3900.
3. Wang Y, Christy PS, Korosec FR, Alley MT, Grist TM, Polzin JA, Mistretta CA. Coronary mri with a respiratory feedback monitor: The 2d imaging case. *Magn Reson Med*. 1995; 33:116-121.
4. Wong JW, Sharpe MB, Jaffray DA, Kini VR, Robertson JM, Stromberg JS, Martinez AA. The use of active breathing control (abc) to reduce margin for breathing motion. *Int J Radiat Oncol Biol Phys*. 1999; 44:911-919.
5. Mittauer KE, Deraniyagala R, Li JG, Lu B, Liu C, Samant SS, Lightsey JL, Yan G. Monitoring abc-assisted deep inspiration breath hold for left-sided breast radiotherapy with an optical tracking system. *Med Phys*. 2015; 42:134-143.
6. Suh Y, Dieterich S, Cho B, Keall PJ. An analysis of thoracic and abdominal tumour motion for stereotactic body radiotherapy patients. *Phys Med Biol*. 2008; 53:3623-3640.
7. Kim T, Pollock S, Lee D, O'Brien R, Keall P. Audiovisual biofeedback improves diaphragm motion reproducibility in mri. *Med Phys*. 2012; 39:6921-6928. PMCID:PMC3494729.
8. Kim T, Pooley R, Lee D, Keall P, Lee R, Kim S. Quasi-breath-hold (qbh) biofeedback in gated 3d thoracic mri: Feasibility study. *Prog Med Phys*. 2014; 25:72-78.
9. Lee D, Greer PB, Ludbrook J, Arm J, Hunter P, Pollock S, Makhija K, O'Brien R T, Kim T, Keall P. Audiovisual biofeedback improves cine-magnetic resonance imaging measured lung tumor motion consistency. *Int J Radiat Oncol Biol Phys*. 2016; 94:628-636.
10. Steel H, Pollock S, Lee D, Keall P, Kim T. The internal-external respiratory motion correlation is unaffected by audiovisual biofeedback. *Australas Phys Eng Sci Med*. 2014; 37:97-102.
11. Pollock S, Lee D, Keall P, Kim T. Audiovisual biofeedback improves motion prediction accuracy. *Med Phys*. 2013; 40:041705. PMCID:PMC3612118.
12. Arnold JF, Morchel P, Glaser E, Pracht ED, Jakob PM. Lung mri using an mr-compatible active breathing control (mr-abc). *Magn Reson Med*. 2007; 58:1092-1098.
13. Blackall JM, Ahmad S, Miquel ME, McClelland JR, Landau DB, Hawkes DJ. Mri-based measurements of respiratory motion variability and assessment of imaging strategies for radiotherapy planning. *Phys Med Biol*. 2006; 51:4147-4169.
14. Shimizu S, Shirato H, Aoyama H, Hashimoto S, Nishioka T, Yamazaki A, Kagei K, Miyasaka K. High-speed magnetic resonance imaging for four-dimensional treatment planning of conformal radiotherapy of moving body tumors. *Int J Radiat Oncol Biol Phys*. 2000; 48:471-474.

15. Taouli B, Chouli M, Martin AJ, Qayyum A, Coakley FV, Vilgrain V. Chronic hepatitis: Role of diffusion-weighted imaging and diffusion tensor imaging for the diagnosis of liver fibrosis and inflammation. *J Magn Reson Imaging*. 2008; 28:89-95.

16. Eccles CL, Haider EA, Haider MA, Fung S, Lockwood G, Dawson LA. Change in diffusion weighted mri during liver cancer radiotherapy: Preliminary observations. *Acta Oncol*. 2009; 48:1034-1043.

17. Mariappan YK, Glaser KJ, Ehman RL. Magnetic resonance elastography: A review. *Clin Anat*. 2010; 23:497-511. PMCID:PMC3066083. NIHMSID:NIHMS278057.

18. Yin M, Talwalkar JA, Glaser KJ, Manduca A, Grimm RC, Rossman PJ, Fidler JL, Ehman RL. Assessment of hepatic fibrosis with magnetic resonance elastography. *Clin Gastroenterol Hepatol*. 2007; 5:1207-1213 e1202. PMCID:PMC2276978. NIHMSID:NIHMS32401.

APPENDIX 1. INVESTIGATIONAL DEVICE LABEL

The investigational device, an integral part of the breathing motion management system, is illustrated in Figure 5 (Part B). This device will be labeled in accordance with CFR 812.5 which includes the information listed below.

- Name and place of business of the manufacturer, packer, or distributor
- Quantity of contents, if appropriate
- The following statement: “CAUTION: Investigational device. Limited by Federal law to investigational use.”

There are no contraindications, hazards, adverse effects, interfering substances or devices, warnings, or precautions included on the label because none have been identified to be associated with this device.

APPENDIX 2. PERFORMANCE STATUS CRITERIA

ECOG Performance Status Scale		Karnofsky Performance Scale	
Grade	**Description**	**Percent**	**Description**
0	Normal activity. Fully active, able to carry on all pre-disease performance without restriction.	100	Normal, no complaints, no evidence of disease.
		90	Able to carry on normal activity; minor signs or symptoms of disease.
1	Symptoms, but ambulatory. Restricted in physically strenuous activity, but ambulatory and able to carry out work of a light or sedentary nature (eg, light housework, office work).	80	Normal activity with effort; some signs or symptoms of disease.
		70	Cares for self; unable to carry on normal activity or to do active work.
2	In bed < 50% of the time. Ambulatory and capable of all self-care, but unable to carry out any work activities. Up and about > 50% of waking hours.	60	Requires occasional assistance, but is able to care for most of his/her needs.
		50	Requires considerable assistance and frequent medical care.
3	In bed > 50% of the time. Capable of only limited self-care, confined to bed or chair > 50% of waking hours.	40	Disabled; requires special care and assistance.
		30	Severely disabled; hospitalization indicated. Death not imminent.
4	100% bedridden. Completely disabled. Cannot carry on any self-care. Totally confined to bed or chair.	20	Very sick, hospitalization indicated. Death not imminent.
		10	Moribund, fatal processes progressing rapidly.
5	Dead.	0	Dead.

A.2 IRB MCC-16-13073 Cohort A

RESEARCH PARTICIPANT INFORMED CONSENT FORM

TITLE: A Pilot Study to Develop A Clinical MRI Procedure and Application for Precise Stereotactic Body Radiation Therapy to Treat Primary or Metastatic Cancer in the Liver

Group A Participants –Photographs and Videos of Mouth and Teeth in Healthy Volunteers

PROTOCOL #: MCC-16-13073

VCU IRB #: HM20010234

SPONSOR-INVESTIGATOR: Taeho Kim, PhD
Virginia Commonwealth University
Massey Cancer Center
PO Box 980058
Richmond, VA 23298
804-828-7418

INTRODUCTION

This consent form will tell you about this research study. The researchers or study team will explain the research study to you. Research studies only include people who choose to take part. You have the option to not participate. You may take home an unsigned copy of this consent form so that you can discuss the study with your family or friends before making your decision. If you have any questions, ask Dr. Kim or a member of the study team for more explanation.

WHY IS THIS STUDY BEING DONE?

This study is being done to develop and test systems that may be able to improve the process of treatment planning for a type of radiation therapy called “stereotactic body radiation therapy” (SBRT) for patients with cancer. You are being asked to participate as a healthy volunteer by having a photographs and videos of your mouth and teeth to help improve the device used to manage breathing during SBRT planning.

There will be about 15 to 20 healthy volunteers taking part in Group A of this study.

WHAT WILL I BE ASKED TO DO IF I TAKE PART IN THIS STUDY?

Participants in Group A will be asked to attend one 30-minute session, which will take place in the Radiation Oncology Department at Virginia Commonwealth University (VCU). A member of the study team will photograph and videotape your mouth and teeth. The images of your mouth and teeth will be used to develop a mouthpiece for a breathing motion management device which will be tested by other groups participating in this study

Before or during your session, you will be weighed and have your height measured. Information about you including your age, sex, race, and ethnicity will be collected.

.

HOW LONG WILL I BE IN THIS STUDY?

Your participation in Group A will take place on one day during a session lasting about 30 minutes.

WHAT POSSIBLE RISKS CAN I EXPECT FROM TAKING PART IN THIS STUDY?

There are no anticipated risks or discomforts.

WHAT POSSIBLE BENEFITS CAN I EXPECT FROM TAKING PART IN THIS STUDY?

You will not receive any benefit from taking part in this study. In the future, patients with cancer may benefit from the knowledge gained through your participation.

CAN I STOP TAKING PART IN THIS STUDY?

Yes. You can decide to stop at any time. If you decide to stop taking part in this study, the images of your mouth and teeth and the information collected about you up to the time that you stop taking part will be kept in the study records and will not be removed.

The researchers will tell you about new information or changes in the study that may affect your willingness to take part in the study. If the study is stopped by the sponsor or the institutional review board (IRB), which is a group of people who review the research with the goal of protecting the people who take part in the study, the researchers may take you out of the study before you have your dental session.

WHAT ARE MY RIGHTS IN THIS STUDY?

Taking part in this study is your choice. No matter what decision you make, and even if your decision changes, there will be no penalty to you. Your decision will not affect your relationship with the researchers or with VCU. You will not lose any legal rights.

WHAT ARE THE COSTS OF TAKING PART IN THIS STUDY?

You will not be billed for the photographs or video images taken of your mouth and teeth.

You will not be paid for taking part in this study.

WHO WILL SEE MY INFORMATION?

Your privacy is very important to us. The researchers will make every effort to protect it but your information may be given out if required by law. However, the researchers will do their best to make sure that any information that is released will not identify you.

Your face will not appear in the photographs and videos. Your photographs, videos, and personal identifying information will be kept private through the use of password-protected electronic files and locked research areas. Study identification numbers and your initials instead of your name will be used on any images and other study records. The results of this research may be presented at meetings or in publications, but you will not be identified by name.

There are groups that may inspect your records. These groups are required to make sure your information is kept private, unless required by law to provide information. Some of these groups are:

- Virginia Commonwealth University (VCU)
- VCU IRB
- National Cancer Institute (NCI)

WHO CAN ANSWER MY QUESTIONS ABOUT THIS STUDY?

You can talk to Dr. Kim about any questions or concerns you have about this study. You can also contact a study team member at 804-628-2334.

The Office of Sponsored Research can answer your general questions or concerns about your rights as a participant in this or any other research. Also, if you would like to speak to a person who does not work directly with Dr. Kim and the study team or if you cannot reach the researchers or a member of the study team, you may contact the Office of Research.

Office of Research
Virginia Commonwealth University
800 East Leigh Street, Suite 3000
PO Box 980568
Richmond, VA 23298
804-827-2157

MY SIGNATURE AGREEING TO TAKE PART IN GROUP A OF THIS STUDY

I have been given the opportunity to carefully read this consent form. All of the questions that I wish to raise concerning this study have been answered.

By signing this consent form, I have not given up any of my legal rights or benefits. My signature indicates that I freely consent to participate in this research study. I will receive a copy of the signed consent form.

_____
Participant Name (*Printed*)

_____ _____
Participant Name (*Signature*) Date

_____
Person Conducting Informed Consent Discussion (*Printed Name*)

_____ _____
Person Conducting Informed Consent Discussion (*Signature*) Date

_____ _____
Signature of Investigator (*If different than above*) Date

A.3 IRB MCC-16-13073 Cohort B

RESEARCH PARTICIPANT INFORMED CONSENT FORM

TITLE: A Pilot Study to Develop A Clinical MRI Procedure and Application for Precise Stereotactic Body Radiation Therapy to Treat Primary or Metastatic Cancer in the Liver

Group B Participants – Testing a Breathing Motion Management Device in Healthy Volunteers

PROTOCOL #: MCC-16-13073

VCU IRB #: HM20010234

SPONSOR-INVESTIGATOR: Taeho Kim, PhD
Virginia Commonwealth University
Massey Cancer Center
PO Box 980058
Richmond, VA 23298
804-828-7418

INTRODUCTION

This consent form will tell you about this research study. The researchers or study team will explain the research study to you. Research studies only include people who choose to take part. You have the option to not participate. You may take home an unsigned copy of this consent form so that you can discuss the study with your family or friends before making your decision. If you have any questions, ask Dr. Kim or a member of the study team for more explanation.

WHY IS THIS STUDY BEING DONE?

This study is being done to develop and test systems that may be able to improve the process of treatment planning for a type of radiation therapy called “stereotactic body radiation therapy” (SBRT) for patients with cancer. Managing the normal breathing movement of the chest and abdomen can improve SBRT treatment planning. You are being asked to participate as a healthy volunteer by testing the device that will be used to manage breathing during treatment planning.

There will be about 10 to 15 healthy volunteers taking part in Group B of this study.

WHAT WILL I BE ASKED TO DO IF I TAKE PART IN THIS STUDY?

Participants in Group B will be asked to attend one 60-minute session to test a breathing device. The session will take place in the Radiation Oncology Department at Virginia Commonwealth University (VCU). While lying on a couch, you will use the breathing device that has been developed for this study. Tracings will be made of your breathing and the movement of your chest and abdomen.

Before or during your session, you will be weighed and have your height measured. Information about you including your age, sex, race, and ethnicity will be collected.

HOW LONG WILL I BE IN THIS STUDY?

Your participation in Group B will take place on one day during a session lasting about one hour.

WHAT POSSIBLE RISKS CAN I EXPECT FROM TAKING PART IN THIS STUDY?

There are no anticipated risks or discomforts.

WHAT POSSIBLE BENEFITS CAN I EXPECT FROM TAKING PART IN THIS STUDY?

You will not receive any benefit from taking part in this study. In the future, patients with cancer may benefit from the knowledge gained through your participation in this study.

CAN I STOP TAKING PART IN THIS STUDY?

Yes. You can decide to stop at any time. If you decide to stop taking part in this study, the information collected about you up to the time that you stop taking part in the study will be kept in the study and will not be removed.

The researchers will tell you about new information or changes in the study that may affect your willingness to take part in the study. If the study is stopped by the sponsor or the institutional review board (IRB), which is a group of people who review the research with the goal of protecting the people who take part in the study, the researchers may take you out of the study.

WHAT ARE MY RIGHTS IN THIS STUDY?

Taking part in this study is your choice. No matter what decision you make, and even if your decision changes, there will be no penalty to you. Your decision will not affect your relationship with the researchers or with VCU. You will not lose any legal rights.

WHAT ARE THE COSTS OF TAKING PART IN THIS STUDY?

You will not be billed for any of the research activities for this study.

You will not be paid for taking part in this study.

WHO WILL SEE MY INFORMATION?

Your privacy is very important to us. The researchers will make every effort to protect it but your information may be given out if required by law. However, the researchers will do their best to make sure that any information that is released will not identify you.

Your research records will be kept private through the use of password-protected electronic files and locked research areas. Study identification numbers and your initials instead of your name will be used on any study records. The results of this research may be presented at meetings or in publications, but you will not be identified by name.

There are groups that may inspect your records. These groups are required to make sure your information is kept private, unless required by law to provide information. Some of these groups are:

- Virginia Commonwealth University (VCU)
- VCU IRB
- National Cancer Institute (NCI)

WHO CAN ANSWER MY QUESTIONS ABOUT THIS STUDY?

You can talk to Dr. Kim about any questions or concerns you have about this study. You can also contact a study team member at 804-628-2334.

The Office of Sponsored Research can answer your general questions or concerns about your rights as a participant in this or any other research. Also, if you would like to speak to a person who does not work directly with Dr. Kim and the study team or if you cannot reach the researchers or a member of the study team, you may contact the Office of Research.

Office of Research
Virginia Commonwealth University
800 East Leigh Street, Suite 3000
PO Box 980568
Richmond, VA 23298
804-827-2157

MY SIGNATURE AGREEING TO TAKE PART IN GROUP B OF THIS STUDY

I have been given the opportunity to carefully read this consent form. All of the questions that I wish to raise concerning this study have been answered.

By signing this consent form, I have not given up any of my legal rights or benefits. My signature indicates that I freely consent to participate in this research study. I will receive a copy of the signed consent form.

_____
Participant Name (*Printed*)

_____ _____
Participant Name (*Signature*) Date

_____
Person Conducting Informed Consent Discussion (*Printed Name*)

_____ _____
Person Conducting Informed Consent Discussion (*Signature*) Date

_____ _____
Signature of Investigator (*If different than above*) Date

A.4 IRB MCC-16-13073 Cohort C

RESEARCH PARTICIPANT INFORMED CONSENT FORM

TITLE: A Pilot Study to Develop A Clinical MRI Procedure and Application for Precise Stereotactic Body Radiation Therapy to Treat Primary or Metastatic Cancer in the Liver

Group C Participants – Magnetic Resonance Imaging (MRI) of the Chest and Abdomen Using the Breathing Motion Management System in Healthy Volunteers

PROTOCOL #: MCC-16-13073

VCU IRB #: HM20010234

SPONSOR-INVESTIGATOR: Taeho Kim, PhD
Virginia Commonwealth University
Massey Cancer Center
PO Box 980058
Richmond, VA 23298
804-828-7418

INTRODUCTION

This consent form will tell you about this research study. The researchers or study team will explain the research study to you. Research studies only include people who choose to take part. You have the option to not participate. You may take home an unsigned copy of this consent form so that you can discuss the study with your family or friends before making your decision. If you have any questions, ask Dr. Kim or a member of the study team for more explanation.

WHY IS THIS STUDY BEING DONE?

This study is being done to develop and test systems that may be able to improve the process of treatment planning for a type of radiation therapy called “stereotactic body radiation therapy” (SBRT) for patients with cancer. You are being asked to participate as a healthy volunteer by having a magnetic resonance imaging (MRI) scan of your chest and abdomen while using the breathing motion management device developed for this study. An MRI is a type of scan that uses magnetic fields and radio waves to make a picture. In this study, the purpose of the MRI is to find out how managing the normal breathing movement of the chest and abdomen during the MRI affects the MRI pictures.

There will be about 4 to 6 healthy participants in Group C of this study.

WHAT WILL I BE ASKED TO DO IF I TAKE PART IN THIS STUDY?

Participants in Group C will be asked to have MRI scans of the chest and abdomen while using the breathing motion management device that has been developed for this study. You will have the following tests and procedures for the purposes of this research study:

Before Study Enrollment

- You will be asked to complete a standard MRI questionnaire to identify any reason you should not have an MRI scan, for example, the presence of metal objects in your body or implanted medical devices.
- You will be weighed and have your height measured. Information about you including your age, sex, race, and ethnicity will be collected.

After Study Enrollment

- You will have two research MRI scans while using the breathing motion management device developed for this study. These research MRIs will be performed at a nearby imaging facility called "Collaborative Advanced Research Imaging (CARI)". The CARI facility is located in Richmond, Virginia near the VCU campus.
- You will have the MRIs at the following time points:
  - About 2 to 3 weeks after you are enrolled in the study
  - About 1 to 4 weeks after the first MRI
- If you are able to become pregnant, you will have a urine pregnancy test at CARI before each scan.
- Before the MRI, you will practice using the breathing management device so that you are able to breathe evenly and consistently over a short period of time. During the MRI, you will lie inside a small closed area inside a large magnetic tube. Each of the two sessions will take 1 to 2 hours including the breathing practice and MRI.

Results of the MRI scans will not be provided to you because the type of research scan being performed are not for the purpose of detecting problems or diagnosing illnesses. However, in the unlikely event that an abnormality is noted on your research MRI images, the study doctor will talk with you about the abnormal finding and suggest follow-up steps.

HOW LONG WILL I BE IN THIS STUDY?

You will be in the study as a participant in Group C for about 1 to 2 months depending on when you have your MRI scans.

WHAT POSSIBLE RISKS CAN I EXPECT FROM TAKING PART IN THIS STUDY?

You may be bothered by the MRI machine noise and by feelings of being closed in (claustrophobia). Using the breathing motion management device during the MRI may possibly increase your feeling of being closed in.

WHAT POSSIBLE BENEFITS CAN I EXPECT FROM TAKING PART IN THIS STUDY?

You will not receive any benefit from taking part in this study. In the future, patients with cancer may benefit from the knowledge gained through your participation in this study.

CAN I STOP TAKING PART IN THIS STUDY?

Yes. You can decide to stop at any time. If you decide to stop taking part in this study, the information collected about you up to the time that you stop taking part in the study will be kept in the study and will not be removed.

The researchers will tell you about new information or changes in the study that may affect your willingness to take part in the study. If the study is stopped by the sponsor or the institutional review board (IRB), which is a group of people who review the research with the goal of protecting the people who take part in the study, the researchers may take you out of the study.

WHAT ARE MY RIGHTS IN THIS STUDY?

Taking part in this study is your choice. No matter what decision you make, and even if your decision changes, there will be no penalty to you. Your decision will not affect your relationship with the researchers or with VCU. You will not lose any legal rights.

WHAT ARE THE COSTS OF TAKING PART IN THIS STUDY?

You will not be billed for any of the research activities for this study.

You will not be paid for taking part in this study, but a small stipend ($50.00 for each MRI scan) will be provided.

WHO WILL SEE MY INFORMATION?

Your privacy is very important to us. The researchers will make every effort to protect it but your information may be given out if required by law. However, the researchers will do their best to make sure that any information that is released will not identify you.

Your MRI images and research records will be kept private through the use of password-protected electronic files and locked research areas. Study identification numbers and your initials instead of your name will be used on any study records. The results of this research may be presented at meetings or in publications, but you will not be identified by name.

There are groups that may inspect your records. These groups are required to make sure your information is kept private, unless required by law to provide information. Some of these groups are:

- Virginia Commonwealth University (VCU)
- VCU IRB
- National Cancer Institute (NCI)

WHO CAN ANSWER MY QUESTIONS ABOUT THIS STUDY?

You can talk to Dr. Kim about any questions or concerns you have about this study. You can also contact a study team member at 804-628-2334.

The Office of Sponsored Research can answer your general questions or concerns about your rights as a participant in this or any other research. Also, if you would like to speak to a person who does not work directly with Dr. Kim and the study team or if you cannot reach the researchers or a member of the study team, you may contact the Office of Research.

Office of Research
Virginia Commonwealth University
800 East Leigh Street, Suite 3000
PO Box 980568
Richmond, VA 23298
804-827-2157

MY SIGNATURE AGREEING TO TAKE PART IN GROUP C OF THIS STUDY

I have been given the opportunity to carefully read this consent form. All of the questions that I wish to raise concerning this study have been answered.

By signing this consent form, I have not given up any of my legal rights or benefits. My signature indicates that I freely consent to participate in this research study. I will receive a copy of the signed consent form.

_____
Participant Name (*Printed*)

_____ _____
Participant Name (*Signature*) Date

_____
Person Conducting Informed Consent Discussion (*Printed Name*)

_____ _____
Person Conducting Informed Consent Discussion (*Signature*) Date

_____ _____
Signature of Investigator (*If different than above*) Date

A.5 IRB MCC-16-13073 Cohort D

RESEARCH PARTICIPANT INFORMED CONSENT FORM

TITLE: A Pilot Study to Develop A Clinical MRI Procedure and Application for Precise Stereotactic Body Radiation Therapy to Treat Primary or Metastatic Cancer in the Liver

Group D Participants – Magnetic Resonance Imaging (MRI) of the Chest and Abdomen Using the Breathing Motion Management System in Participants with Cancer in the Liver

PROTOCOL #: MCC-16-13073

VCU IRB #: HM20010234

SPONSOR-INVESTIGATOR: Taeho Kim, PhD
Virginia Commonwealth University
Massey Cancer Center
PO Box 980058
Richmond, VA 23298
804-828-7418

INTRODUCTION

This consent form will tell you about this research study. The researchers or study team will explain the research study to you. Research studies only include people who choose to take part. You have the option to not participate. You may take home an unsigned copy of this consent form so that you can discuss the study with your family or friends before making your decision. If you have any questions, ask Dr. Kim or a member of the study team for more explanation.

WHY IS THIS STUDY BEING DONE?

This study is being done to develop and test systems that may be able to improve the process of treatment planning for a type of radiation therapy called “stereotactic body radiation therapy” (SBRT) for patients with cancer. You are being asked to participate by having a magnetic resonance imaging (MRI) scan of the chest and abdomen while using the breathing motion management device developed for this study. An MRI is a type of scan that uses magnetic fields and radio waves to make a picture. In this study, the purpose of the MRI is to find out how managing the normal breathing movement of the chest and abdomen during the MRI affects the MRI pictures.

There will be about 4 to 6 participants with cancer in the liver taking part in Group D of this study.

WHAT WILL I BE ASKED TO DO IF I TAKE PART IN THIS STUDY?

All participants in Group D will be asked to have MRI scans of the chest and abdomen while using the breathing motion management device that has been developed for this study. Results of the MRI scans will not be used for planning your SBRT treatment because the methods used are still being researched.

You will have the following tests and procedures for the purposes of this research study:

Before Study Enrollment

- You will be asked to complete a standard MRI questionnaire to identify any reason you should not have an MRI scan, for example, the presence of metal objects in your body or implanted medical devices.
- Information about you including your age, sex, race, ethnicity, height, and weight will be collected.

After Study Enrollment

- You will have two research MRI scans while using the breathing motion management device developed for this study. These research MRIs will be performed at a nearby imaging facility called "Collaborative Advanced Research Imaging (CARI)". The CARI facility is located in Richmond, Virginia near the VCU campus.
- You will have the MRIs at the following time points:
  - Before your first SBRT treatment (within 3 weeks after you are enrolled in the study)
  - Within 1 to 4 weeks after your SBRT treatments have been completed
- If you are able to become pregnant, you will have a urine pregnancy test at CARI before each scan.
- Before the MRI, you will practice using the breathing management device so that you are able to breathe evenly and consistently over a short period of time. During the MRI, you will lie inside a small closed area inside a large magnetic tube. Each of the two sessions will take 1 to 2 hours including the breathing practice and MRI.

HOW LONG WILL I BE IN THIS STUDY?

You will be in the study as a participant in Group D for about 1 to 2 months depending on when you have your MRI scans.

WHAT POSSIBLE RISKS CAN I EXPECT FROM TAKING PART IN THIS STUDY?

You may be bothered by the MRI machine noise and by feelings of being closed in (claustrophobia). Using the breathing motion management device during the MRI may possibly increase your feeling of being closed in.

WHAT POSSIBLE BENEFITS CAN I EXPECT FROM TAKING PART IN THIS STUDY?

You will not receive any benefit from taking part in this study. Future patients with cancer may benefit from the knowledge gained through your participation in this study.

CAN I STOP TAKING PART IN THIS STUDY?

Yes. You can decide to stop at any time. If you decide to stop taking part in this study, the information collected about you up to the time that you stop taking part in the study will be kept in the study and will not be removed.

The researchers will tell you about new information or changes in the study that may affect your willingness to have the MRI scans. If the study is stopped by the sponsor or the institutional review board (IRB), which is a group of people who review the research with the goal of protecting the people who take part in the study, the researchers may take you out of the study.

WHAT ARE MY RIGHTS IN THIS STUDY?

Taking part in this study is your choice. No matter what decision you make, and even if your decision changes, there will be no penalty to you. Your decision will not affect your medical care or your relationship with the researchers or with VCU. You will not lose any legal rights.

WHAT ARE THE COSTS OF TAKING PART IN THIS STUDY?

You will not be billed for any of the research activities for this study.

You will not be paid for taking part in this study, but a small stipend ($50.00 for each MRI scan) will be provided.

WHO WILL SEE MY INFORMATION?

Your privacy is very important to us. The researchers will make every effort to protect it but your information may be given out if required by law. However, the researchers will do their best to make sure that any information that is released will not identify you.

Your research records will be kept private through the use of password-protected electronic files and locked research areas. Study identification numbers and your initials instead of your name will be used on any study records. The results of this research may be presented at meetings or in publications, but you will not be identified by name.

There are groups that may inspect your records. These groups are required to make sure your information is kept private, unless required by law to provide information. Some of these groups are:

- Virginia Commonwealth University (VCU)
- VCU IRB
- National Cancer Institute (NCI)

WHO CAN ANSWER MY QUESTIONS ABOUT THIS STUDY?

You can talk to Dr. Kim about any questions or concerns you have about this study. You can also contact a study team member at 804-628-2334.

The Office of Sponsored Research can answer your general questions or concerns about your rights as a participant in this or any other research. Also, if you would like to speak to a person who does not work directly with Dr. Kim and the study team or if you cannot reach the researchers or a member of the study team, you may contact the Office of Research.

Office of Research
Virginia Commonwealth University
800 East Leigh Street, Suite 3000
PO Box 980568
Richmond, VA 23298
804-827-2157

MY SIGNATURE AGREEING TO TAKE PART IN GROUP D OF THIS STUDY

I have been given the opportunity to carefully read this consent form. All of the questions that I wish to raise concerning this study have been answered.

By signing this consent form, I have not given up any of my legal rights or benefits. My signature indicates that I freely consent to participate in this research study. I will receive a copy of the signed consent form.

_____
Participant Name (*Printed*)

_____ _____
Participant Name (*Signature*) Date

_____
Person Conducting Informed Consent Discussion (*Printed Name*)

_____ _____
Person Conducting Informed Consent Discussion (*Signature*) Date

_____ _____
Signature of Investigator (*If different than above*) Date

Appendix B

MATLAB CODE

B.1 GUI script

```
%Script to create GUI for DICOM import, image registration, denoising, and
%IVIM analysis of DW MRI acquisitions.
%% Run IVIM GUI app to get user selected options
clear

run IVIM_GUI_v1.mlapp

waitfor(IVIM_GUI_v1)

%Prints selected parameters to command window.
fprintf('%s\n\n', 'Selected parameters'); fprintf('Number of folders: ');
fprintf(num_folders_value); fprintf('\nImage registration: '); fprintf(registration_value);
fprintf('\nDenoising: '); fprintf(denoising_value); fprintf('\nROI preference: ');
fprintf(ROI_value); fprintf('\nADC: '); fprintf(mat2str(ADC_calc_value));
```

```
fprintf('\nIVIM calculation type: '); fprintf(IVIM_calc_value
    ); fprintf('\n');
fprintf('\nTA calc: '); fprintf(mat2str(TA_calc_value));

if ADC_calc_value == 0
    ADC_calc = 'No ADC calculation';
end

if ADC_calc_value == 1
    ADC_calc = 'ADC calculation performed';
end

%%
%Open selected folders and save DICOM files in folders to
    matrix, and
%extract image matrix, b values, and number of b values.

if num_folders_value == 'One folder'
    folder_one_name = uigetdir('','Select folder containing
        diffusion weighted image set for analysis')

    if isequal(folder_one_name,0)
        disp('User pressed cancel')
        return
    end
```

```
    [full_matrix num_b_vals unique_b_vals image_size] =
        DICOM_to_matrix_one(folder_one_name);
end

if num_folders_value == 'Two folders'
    folder_one_name = uigetdir('','Select first folder
        containing diffusion weighted image set for analysis')
    folder_two_name = uigetdir('','Select second folder
        containing diffusion weighted image set for analysis')

    if isequal(folder_one_name,0)|isequal(folder_two_name,0)
        disp('User pressed cancel')
        return
    end

    [full_matrix num_b_vals unique_b_vals image_size] =
        DICOM_to_matrix_two(folder_one_name, folder_two_name);
end

original_image = full_matrix;

%%
%Perform image registration using MI based rigid registration

```

```
if registration_value == 'Mutual information based rigid registration'
    [full_matrix] = MI_reg(full_matrix);
    registered_image = full_matrix;
end

if registration_value == 'No image registration'
    registered_image = [];
end



%%
%Perform denoising using desired denoising method

if denoising_value == 'Non-local means filtering'
    [full_matrix] = MRI_denoised(full_matrix);
    denoised_image = full_matrix;
end

if denoising_value == 'No denoising'
    denoised_image = []
end

image_size = size(full_matrix);
```

```
82 %%
83 %Prompts user to draw ROI for desired calculation volume
84
85 if ROI_value == 'Draw custom ROI'
86     [roi_mask] = ROI_contour(full_matrix);
87 end
88
89 if ROI_value == 'Load ROI from .mat file'
90     [file,path] = uigetfile;
91     full_file = fullfile(path, file);
92     roi_mask = load(full_file);
93 end
94
95 if ROI_value == 'No ROI'
96     [roi_mask] = ones(image_size);
97 end
98
99 %%
100 %Perform ADC calc for volume if desired
101
102 if ADC_calc_value == 1
103     [ADC_full] = ADC_calc(full_matrix,unique_b_values);
104 end
105
106 if ADC_calc_value == 0
```

```
    ADC_full = [];
end

%%
%Perform desired IVIM calculation method

if IVIM_method == 'Biexponential method'
    [D_map D_star_map PF_map] = Biexponential_IVIM(full_matrix roi_mask unique_b_values);
    D_star_map = [];
end

if IVIM_method == 'Monoexponential method'
    [D_map PF_map] = Monoexponential_IVIM(full_matrix ADC_map roi_mask unique_b_values);
    D_star_map = [];
end

if IVIM_method == 'LeBihan method'
    [D_map PF_map] = LeBihan_IVIM(full_matrix roi_mask unique_b_values);
    D_star_map = [];
end

%%
```

```
%Perform Texture analysis if desired

if TA_calc_value == 1
    [TA_values] = TA_calc(full_matrix);
end

if TA_calc_value == 0
    TA_values = [];
end
%%
%Generate cell array containing Original image,

Output_values = cell(1,9)
Output_values(1,:) = original_image;
Output_values(2,:) = denoised_image;
Output_values(3,:) = registered_image;
Output_values(4,:) = roi_mask;
Output_values(5,:) = ADC_map;
Output_values(6,:) = D_map;
Output_values(7,:) = D_star_map;
Output_values(8,:) = PF_map;
Output_values(9,:) = TA_values;
```

B.2 GUI main code

```
classdef IVIM_GUI_v1_exported < matlab.apps.AppBase

```

```
    % Properties that correspond to app components
    properties (Access = public)
        UIFigure                                matlab.ui.Figure
        PerformdenoisingwithselectedmethodButtonGroup   matlab
            .ui.container.ButtonGroup
        NodenoisingButton                       matlab.ui.control.
            RadioButton
        NonlocalmeansfilteringButton            matlab.ui.control.
            RadioButton
        DrawROItodefinecalculationvolumeButtonGroup   matlab.
            ui.container.ButtonGroup
        NoROIButton                             matlab.ui.control.
            RadioButton
        LoadROIfrommatfileButton                matlab.ui.control.
            RadioButton
        DrawcustomROIButton                     matlab.ui.control.
            RadioButton
        SelectIVIMcalculationmethodButtonGroup   matlab.ui.
            container.ButtonGroup
        LeBihanmethodnoDatleast3bvaluesButton   matlab.ui.
            control.RadioButton
        MonoexponentialmethodNoDrequires2bvaluesButton
            matlab.ui.control.RadioButton
        BiexponentialmethodButton               matlab.ui.control.
            RadioButton
```

```
17          PerformADCcalculationCheckBox     matlab.ui.control.
                CheckBox
18          NumberoffolderscontainingDWimagesetsButtonGroup
                matlab.ui.container.ButtonGroup
19          OnefolderButton                   matlab.ui.control.
                RadioButton
20          TwofoldersButton                  matlab.ui.control.
                RadioButton
21          PerformimageregistrationButtonGroup   matlab.ui.
                container.ButtonGroup
22          NoimageregistrationButton         matlab.ui.control.
                RadioButton
23          MutualinformationbasedrigidregistrationButton   matlab
                .ui.control.RadioButton
24          OptionsforIVIMandTextureAnalysisCalculationToolboxLabel
                  matlab.ui.control.Label
25          DoneButton                        matlab.ui.control.
                Button
26          PerformTextureAnalysisCheckBox    matlab.ui.control.
                CheckBox
27      end
28
29      methods (Access = private)
30
31          % Button pushed function: DoneButton
```

```
32          function DoneButtonPushed(app, event)
33              ADC_calc_button = app.
                    PerformADCcalculationCheckBox.Value;
34              denoising_button = app.
                    PerformdenoisingwithselectedmethodButtonGroup.
                    SelectedObject;
35              IVIM_calc_button = app.
                    SelectIVIMcalculationmethodButtonGroup.
                    SelectedObject;
36              num_folders_button = app.
                    NumberoffolderscontainingDWimagesetsButtonGroup
                    .SelectedObject;
37              registration_button = app.
                    PerformimageregistrationButtonGroup.
                    SelectedObject;
38              ROI_button = app.
                    DrawROItodefinecalculationvolumeButtonGroup.
                    SelectedObject;
39              TA_calc_button = app.
                    PerformTextureAnalysisCheckBox.Value;
40
41              ADC_calc_value = ADC_calc_button;
42              denoising_value = denoising_button.Text;
43              IVIM_calc_value = IVIM_calc_button.Text;
44              num_folders_value = num_folders_button.Text;
```

```
            registration_value = registration_button.Text;
            ROI_value = ROI_button.Text;
            TA_calc_value = TA_calc_button

            assignin('base','ADC_calc_value',ADC_calc_value);
            assignin('base','denoising_value',denoising_value);
            assignin('base','IVIM_calc_value',IVIM_calc_value);
            assignin('base','num_folders_value',num_folders_value);
            assignin('base','registration_value',registration_value);
            assignin('base','ROI_value',ROI_value);
            assignin('base','TA_calc_value',TA_calc_value);

            app.delete
        end
    end

    % App initialization and construction
    methods (Access = private)

        % Create UIFigure and components
        function createComponents(app)
```

```
66
67          % Create UIFigure
68          app.UIFigure = uifigure;
69          app.UIFigure.Position = [100 100 640 480];
70          app.UIFigure.Name = 'UI Figure';
71
72          % Create
            PerformdenoisingwithselectedmethodButtonGroup
73          app.PerformdenoisingwithselectedmethodButtonGroup
             = uibuttongroup(app.UIFigure);
74          app.PerformdenoisingwithselectedmethodButtonGroup
            .Title = 'Perform denoising with selected
            method';
75          app.PerformdenoisingwithselectedmethodButtonGroup
            .Position = [24 211 258 80];
76
77          % Create NodenoisingButton
78          app.NodenoisingButton = uiradiobutton(app.
            PerformdenoisingwithselectedmethodButtonGroup)
            ;
79          app.NodenoisingButton.Text = 'No denoising';
80          app.NodenoisingButton.Position = [11 37 92 22];
81          app.NodenoisingButton.Value = true;
82
83          % Create NonlocalmeansfilteringButton
```

```
84          app.NonlocalmeansfilteringButton = uiradiobutton(
                app.
                PerformdenoisingwithselectedmethodButtonGroup)
                ;
85          app.NonlocalmeansfilteringButton.Text = 'Non-
                local means filtering';
86          app.NonlocalmeansfilteringButton.Position = [11
                15 154 22];
87
88          % Create
                DrawROItodefinecalculationvolumeButtonGroup
89          app.DrawROItodefinecalculationvolumeButtonGroup =
                 uibuttongroup(app.UIFigure);
90          app.DrawROItodefinecalculationvolumeButtonGroup.
                Title = 'Draw ROI to define calculation volume
                ';
91          app.DrawROItodefinecalculationvolumeButtonGroup.
                Position = [371 300 229 106];
92
93          % Create NoROIButton
94          app.NoROIButton = uiradiobutton(app.
                DrawROItodefinecalculationvolumeButtonGroup);
95          app.NoROIButton.Text = 'No ROI';
96          app.NoROIButton.Position = [11 60 62 22];
97          app.NoROIButton.Value = true;
```

```
98
99          % Create LoadROIfrommatfileButton
100         app.LoadROIfrommatfileButton = uiradiobutton(app.
                DrawROItodefinecalculationvolumeButtonGroup);
101         app.LoadROIfrommatfileButton.Text = 'Load ROI
                from .mat file';
102         app.LoadROIfrommatfileButton.Position = [11 38
                146 22];
103
104         % Create DrawcustomROIButton
105         app.DrawcustomROIButton = uiradiobutton(app.
                DrawROItodefinecalculationvolumeButtonGroup);
106         app.DrawcustomROIButton.Text = 'Draw custom ROI';
107         app.DrawcustomROIButton.Position = [11 16 117
                22];
108
109         % Create SelectIVIMcalculationmethodButtonGroup
110         app.SelectIVIMcalculationmethodButtonGroup =
                uibuttongroup(app.UIFigure);
111         app.SelectIVIMcalculationmethodButtonGroup.Title
               = 'Select IVIM calculation method';
112         app.SelectIVIMcalculationmethodButtonGroup.
                Position = [371 60 229 136];
113
114         % Create LeBihanmethodnoDatleast3bvaluesButton
```

```
115             app.LeBihanmethodnoDatleast3bvaluesButton =
                    uiradiobutton(app.
                    SelectIVIMcalculationmethodButtonGroup);
116             app.LeBihanmethodnoDatleast3bvaluesButton.Text =
                    {'LeBihan method (no D*'; ' at least 3 b-
                    values)'};
117             app.LeBihanmethodnoDatleast3bvaluesButton.
                    Position = [11 40 147 28];
118             app.LeBihanmethodnoDatleast3bvaluesButton.Value =
                     true;
119
120             % Create
                    MonoexponentialmethodNoDrequires2bvaluesButton
121             app.
                    MonoexponentialmethodNoDrequires2bvaluesButton
                     = uiradiobutton(app.
                    SelectIVIMcalculationmethodButtonGroup);
122             app.
                    MonoexponentialmethodNoDrequires2bvaluesButton
                    .Text = {'Monoexponential method(No D*'; '
                    requires 2 b-values)'};
123             app.
                    MonoexponentialmethodNoDrequires2bvaluesButton
                    .Position = [11 77 194 28];
124
```

```
125             % Create BiexponentialmethodButton
126             app.BiexponentialmethodButton = uiradiobutton(app
                    .SelectIVIMcalculationmethodButtonGroup);
127             app.BiexponentialmethodButton.Text = '
                    Biexponential method';
128             app.BiexponentialmethodButton.Position = [11 10
                    137 22];
129
130             % Create PerformADCcalculationCheckBox
131             app.PerformADCcalculationCheckBox = uicheckbox(
                    app.UIFigure);
132             app.PerformADCcalculationCheckBox.Text = 'Perform
                     ADC calculation';
133             app.PerformADCcalculationCheckBox.Position = [382
                     211 153 22];
134
135             % Create
                    NumberoffolderscontainingDWimagesetsButtonGroup

136             app.
                    NumberoffolderscontainingDWimagesetsButtonGroup
                     = uibuttongroup(app.UIFigure);
137             app.
                    NumberoffolderscontainingDWimagesetsButtonGroup
                    .Title = 'Number of folders containing DW
```

```
image sets';
138             app.
                NumberoffolderscontainingDWimagesetsButtonGroup
                .Position = [24 337 258 69];
139
140             % Create OnefolderButton
141             app.OnefolderButton = uiradiobutton(app.
                NumberoffolderscontainingDWimagesetsButtonGroup
                );
142             app.OnefolderButton.Text = 'One folder';
143             app.OnefolderButton.Position = [11 23 78 22];
144             app.OnefolderButton.Value = true;
145
146             % Create TwofoldersButton
147             app.TwofoldersButton = uiradiobutton(app.
                NumberoffolderscontainingDWimagesetsButtonGroup
                );
148             app.TwofoldersButton.Text = 'Two folders';
149             app.TwofoldersButton.Position = [11 1 83 22];
150
151             % Create PerformimageregistrationButtonGroup
152             app.PerformimageregistrationButtonGroup =
                uibuttongroup(app.UIFigure);
153             app.PerformimageregistrationButtonGroup.Title = '
                Perform image registration';
```

```
154             app.PerformimageregistrationButtonGroup.Position
                    = [24 91 258 87];
155
156             % Create NoimageregistrationButton
157             app.NoimageregistrationButton = uiradiobutton(app
                    .PerformimageregistrationButtonGroup);
158             app.NoimageregistrationButton.Text = 'No image
                    registration';
159             app.NoimageregistrationButton.Position = [11 45
                    136 22];
160             app.NoimageregistrationButton.Value = true;
161
162             % Create
                    MutualinformationbasedrigidregistrationButton
163             app.MutualinformationbasedrigidregistrationButton
                     = uiradiobutton(app.
                    PerformimageregistrationButtonGroup);
164             app.MutualinformationbasedrigidregistrationButton
                    .Text = 'Mutual information based rigid
                    registration';
165             app.MutualinformationbasedrigidregistrationButton
                    .Position = [10 22 247 22];
166
167             % Create
                    OptionsforIVIMandTextureAnalysisCalculationToolboxLabel
```

```
168             app.
                    OptionsforIVIMandTextureAnalysisCalculationToolboxLabel
                     = uilabel(app.UIFigure);
169             app.
                    OptionsforIVIMandTextureAnalysisCalculationToolboxLabel
                    .HorizontalAlignment = 'center';
170             app.
                    OptionsforIVIMandTextureAnalysisCalculationToolboxLabel
                    .FontSize = 20;
171             app.
                    OptionsforIVIMandTextureAnalysisCalculationToolboxLabel
                    .Position = [58 440 529 24];
172             app.
                    OptionsforIVIMandTextureAnalysisCalculationToolboxLabel
                    .Text = 'Options for IVIM and Texture Analysis
                     Calculation Toolbox';
173
174             % Create DoneButton
175             app.DoneButton = uibutton(app.UIFigure, 'push');
176             app.DoneButton.ButtonPushedFcn =
                    createCallbackFcn(app, @DoneButtonPushed, true
                    );
177             app.DoneButton.Position = [271 22 100 22];
178             app.DoneButton.Text = 'Done';
```

```
            % Create PerformTextureAnalysisCheckBox
            app.PerformTextureAnalysisCheckBox = uicheckbox(
                app.UIFigure);
            app.PerformTextureAnalysisCheckBox.Text = '
                Perform Texture Analysis';
            app.PerformTextureAnalysisCheckBox.Position =
                [381 256 155 22];
        end
    end

    methods (Access = public)

        % Construct app
        function app = IVIM_GUI_v1_exported

            % Create and configure components
            createComponents(app)

            % Register the app with App Designer
            registerApp(app, app.UIFigure)

            if nargout == 0
                clear app
            end
```

```
        end

        % Code that executes before app deletion
        function delete(app)

            % Delete UIFigure when app is deleted
            delete(app.UIFigure)
        end
    end
end
```

B.3 DICOM input

```
function [full_matrix num_b_vals unique_b_vals image_size] =
    DICOM_to_matrix_one(folder_one_name)
%DICOM_to_matrix_one
%   Takes in the directory of a single folder with a
    diffusion weighted
%   image set and converts the DICOM files to an array with
    the
%   dimmensions: [x y b-values slices]

%%MRI Read in DICOM data for IVIM scan


cd folder_one_name
image_files = dir(folder_one_name)
```

```
num_images = size(image_files,1)  %Counts the number of files in the selected folder

b_values1 = zeros(1,num_images);
position = zeros(1,num_images);

cd folder_one_name


%%

%%Generate 4D Matrix of 2D images in a and b, by b-value in c, and slice in
%d, matrix form [a,b,c,d]

first_name = getfield(image_files,{3,1},'name');
first_image = dicomread(first_name);
image_size = size(first_image)


%% Find all b-values and number of b_values

for i = 1:num_images
    name = getfield(image_files,{(i+2),1},'name');
    info = dicominfo(name);
```

```
    b_values((i)) = getfield(info,'DiffusionBValue');
end

unique_b_values = unique(b_values);

num_b_values = length(unique_b_values);

num_slices = num_images/num_b_values;

image_matrix = zeros(image_size(1),image_size(2),num_b_values
    ,num_slices);

j = 0;

for s = 1:num_slices
    for b = 1:num_b_values
        j = j+1;
        name = getfield(image_files,{(j+2),1},'name');
        image = dicomread(name);
        image_matrix(:,:,b,s) = image;
    end
end

full_matrix = image_matrix;

```

```
full_matrix(full_matrix == 0) = eps;

image_size = size(full_matrix);

end
```

```
function [full_matrix num_b_vals unique_b_vals image_size] =
    DICOM_to_matrix_two(folder_one_name,folder_two_name)
%DICOM_to_matrix_one
%   Takes in the directory of a single folder with a
    diffusion weighted
%   image set and converts the DICOM files to an array with
    the
%   dimmensions: [x y b-values slices]

%%MRI Read in DICOM data for IVIM scan


cd folder_one_name
image_files = dir(folder_one_name)
num_images1 = size(image_files,1)  %Counts the number of
    files in the selected folder

b_values1 = zeros(1,num_images1);
position = zeros(1,num_images1);

```

```
cd folder_one_name

%%

%%Generate 4D Matrix of 2D images in a and b, by b-value in c
    , and slice in
%d, matrix form [a,b,c,d]

first_name1 = getfield(image_files,{3,1},'name');
first_image1 = dicomread(first_name1);
image_size = size(first_image1)


%% Find all b-values and number of b_values

for i = 1:num_images1
    name = getfield(image_files,{(i+2),1},'name');
    info = dicominfo(name);
    b_values1((i)) = getfield(info,'DiffusionBValue');
end

unique_b_values1 = unique(b_values1);

num_b_values1 = length(unique_b_values1);

```

```
num_slices1 = num_images/num_b_values1;

image_matrix1 = zeros(image_size(1),image_size(2),
    num_b_values1,num_slices1);

j = 0;

for s = 1:num_slices1
    for b = 1:num_b_values1
        j = j+1;
        name = getfield(image_files,{(j+2),1},'name');
        ivim_image = dicomread(name);
        image_matrix1(:,:,b,s) = ivim_image;
    end
end

image_matrix1(image_matrix1 == 0) = eps;

%% Call dicom images from 2nd image set
cd folder_two_name
image_files = dir(folder_one_name)
num_images2 = size(image_files,1)  %Counts the number of
    files in the selected folder

b_values1 = zeros(1,num_images1);
```

```
position = zeros(1,num_images1);

cd folder_two_name

%%

%%Generate 4D Matrix of 2D images in a and b, by b-value in c
    , and slice in
%d, matrix form [a,b,c,d]

first_name2 = getfield(image_files,{3,1},'name');
first_image2 = dicomread(first_name2);
image_size = size(first_image2)


%% Find all b-values and number of b_values

for i = 1:num_images2
    name = getfield(image_files,{(i+2),1},'name');
    info = dicominfo(name);
    b_values2((i)) = getfield(info,'DiffusionBValue');
end

unique_b_values2 = unique(b_values2);

```

```
num_b_values2 = length(unique_b_values2);

num_slices2 = num_images/num_b_values2;

image_matrix2 = zeros(image_size(1),image_size(2),
    num_b_values2,num_slices2);

j = 0;

for s = 1:num_slices2
    for b = 1:num_b_values2
        j = j+1;
        name = getfield(image_files,{(j+2),1},'name');
        ivim_image = dicomread(name);
        image_matrix2(:,:,b,s) = ivim_image;
    end
end

image_matrix2(image_matrix2 == 0) = eps;

total_b_values = num_b_values1+num_b_values2-1
unique_b_values = zeros(1,total_b_values);
unique_b_values(1,1:num_b_values1) = unique_b_values1;
unique_b_values(1,(num_b_values1+1):end) = unique_b_values2
    (2:end);
```

```
full_matrix = zeros(image_size(1),image_size(2),
    total_b_values,num_slices1);

full_matrix(:,:,1:num_b_values1,:) = image_matrix1;
full_matrix(:,:,(num_b_values1+1):(total_b_values),:) =
    image_matrix2(:,:,2:end,:);


full_matrix(full_matrix == 0) = eps;
```

B.4 Image registration

```
function [full_matrix] = MI_reg(full_matrix);

image_size = size(full_matrix);

num_slices = image_size(4);
total_b_values = image_size(3);

%%Rigid registration of images

[optimizer,metric] = imregconfig('multimodal');

optimizer.InitialRadius = 0.009;
optimizer.Epsilon = 1.5e-4;
optimizer.GrowthFactor = 1.01;
```

```
optimizer.MaximumIterations = 300;


movingRegistered = zeros(image_size(1),image_size(2),
    total_b_values,num_slices1);
%difference_map = zeros(image_size(1),image_size(2),1,
    total_b_values);
movingRegistered(:,:,1,:) = full_matrix(:,:,1,:);

for k = 1:num_slices
    for i = 2:total_b_values
        fixed = full_matrix(:,:,1,k);
        moving = full_matrix(:,:,i,k);
        movingRegistered(:,:,i,k) = imregister(moving,fixed,'
            rigid',optimizer,metric);
    end
end

end
```

B.5 Noise Removal

```
function [filtered_matrix] = MRI_denoised(full_matrix)

image_matrix = full_matrix;

image_size = size(image_matrix);
```

```
num_slices = image_size(4);
num_b_values = image_size(3);

%% Calls the simple nlm function

slice_max = zeros(num_b_values,num_slices);

[n x] = hist(image_matrix(:));

cutoff = x(8);

image_matrix(image_matrix > cutoff) = cutoff;

for s = 1:num_slices
    for b = 1:num_b_values
        slice = image_matrix(:,:,b,s);
        slice_max(b,s) = max(slice(:));
        filtered_matrix(:,:,b,s) = simple_nlm((image_matrix
            (:,:,b,s)/slice_max(b,s)*100),1,0,1,1,0);
        filtered_matrix(:,:,b,s) = filtered_matrix(:,:,b,s)*
            slice_max(b,s)/100);
    end
end

```

```
filtered_matrix(filtered_matrix <= 0) = eps;

    function [output]=simple_nlm(input,t,f,h1,h2,selfsim)

    %  For details see:
    %     A. Buades, B. Coll and J.M. Morel, "A non-local algorithm for image denoising"

    [m n]=size(input);
    pixels = input(:);

    s = m*n;

    psize = 2*f+1;
    nsize = 2*t+1;

     % Compute patches
     padInput = padarray(input,[f f],'symmetric');
     filter = fspecial('gaussian',psize,h1);
     patches = repmat(sqrt(filter(:))',[s 1]) .* im2col(padInput, [psize psize], 'sliding')';

    % Compute list of edges (pixel pairs within the same search window)
    indexes = reshape(1:s, m, n);
```

```
    padIndexes = padarray(indexes, [t t]);
    neighbors = im2col(padIndexes, [nsize, nsize], 'sliding')
        ;
    TT = repmat(1:s, [nsize^2 1]);
    edges = [TT(:) neighbors(:)];
    RR = find(TT(:) >= neighbors(:));
    edges(RR, :) = [];

    % Compute weight matrix (using weighted Euclidean
        distance)
    diff = patches(edges(:,1), :) - patches(edges(:,2), :);
    V = exp(-sum(diff.*diff,2)/h2^2);
    W = sparse(edges(:,1), edges(:,2), V, s, s);

    % Make matrix symetric and set diagonal elements
    if selfsim > 0
        W = W + W' + selfsim*speye(s);
    else
        maxv = max(W,[],2);
        W = W + W' + spdiags(maxv, 0, s, s);
    end

    % Normalize weights
    W = spdiags(1./sum(W,2), 0, s, s)*W;

```

```
    % Compute denoised image
    output = W*pixels;
    output = reshape(output, m , n);

    end

end
```

B.6 ROI selection

```
function [roi_mask] = ROI_contour(full_matrix)
%Generate a binary ROI mask using the roipoly function in
    matlab

image_size = size(full_matrix);

roi_mask = zeros(image_size(1),image_size(2),image_size(4));

for k = 1:num_slices1
    slice = full_matrix(:,:,1,k);
    im_max = max(slice(:));
    roi_mask(:,:,k) = roipoly((4*(full_matrix(:,:,1,k)/im_max
        )));
end


end
```

B.7 ADC calculation

```
function [ADC_full] = ADC_calc(full_matrix,unique_b_values)

%Calculates ADC_map using the smallest and largest b value
    images

image_size = size(full_matrix);

ADC_map = zeros(image_size(1),image_size(2),num_slices1);

ind = length(unique_b_values);


for k = 1:image_size(4)
    for l = 1:image_size(1)
        for m = 1:image_size(2)
                ADC_map(l,m,k) = (log(movingRegistered(l,m,
                    ind,k)/movingRegistered(l,m,1,k))/(
                    unique_b_values(1)-unique_b_values(2)));
        end
    end
end

end
```

B.8 IVIM parameter calculatin

B.8.1 LeBihan's method

```
function [D_map PF_map] = LeBihan_IVIM(full_matrix roi_mask
    unique_b_values)

%Calculated D and f maps using LeBihan's method and least
    squares fitting

D_map = zeros((box_size+1),(box_size+1));
PF_map = zeros((box_size+1),(box_size+1));

ind = find(unique_b_values > 150, 1);

xdata = [unique_b_values];
x0 = [0 0];

f = @(x,xdata)exp(-xdata*x(1)+log(1-x(2)));


for s = 1:image_size(4)
    for k = 1:image_size(1)
        for l = 1:image_size(2)
            if roi_mask(k,l,s) == 1
                for b = ind:image_size(3)
                    ratio(b-ind+1) = full_matrix(k,l,b,s)/
```

```
                    full_matrix(k,l,ind,s);
                end

                a = lsqcurvefit(f,x0,xdata,ratio);

                D_map(k,l) = a(1);
                PF_map(k,l) = a(2);
            end
        end
    end
end


D_map(D_map <= 0) = eps;
PF_map(PF_map <= 0) = eps;

end
```

B.8.2 Monoexponential method

```
function [D_map PF_map] = Monoexponential_IVIM(full_matrix
    ADC_map roi_mask unique_b_values)

%% Calculate D_slow_LB using Le Bihan Model

image_size = size(full_matrix)

```

```
ind = find(unique_b_values > 90, 1);

D_map = zeros(image_size(1),image_size(2),image_size(4));

for k = 1:image_size(4)
    for l = 1:image_size(1)
        for m = 1:image_size(2)
            D_map(l,m,k) = log(movingRegistered(l,m,end,k)/
                movingRegistered(l,m,ind,k))/(unique_b_values(
                ind)-unique_b_values(end));
        end
    end
end

%% Calculate f map using simplified Lebihan Model.

f_map = zeros(image_size(1),image_size(2),image_size(4));  %
    Map of pseudo-diffusion fraction X(1)

for k = 1:image_size(4)
    for l = 1:image_size(1)
        for m = 1:image_size(2)
            f_map(l,m,k) = 1-exp(-unique_b_values(end)*(
                ADC_map(l,m,k)-D_map(l,m,k)));
        end
```

```
    end
end

f_map(f_map <= 0) = eps;
f_map(f_map >=1) = eps;

end
```

B.8.3 Biexponential method

```
function [D_map D_star_map PF_map] = Biexponential_IVIM(full_matrix roi_mask unique_b_values)
%%Calculation of IVIM parameters using the biexponential model

image_size = size(full_matrix);

f_map = zeros(image_size(1),image_size(2),image_size(4)); % Map of pseudo-diffusion fraction X(1)
D_map = zeros(image_size(1),image_size(2),image_size(4)); % Map of true diffusion coefficients X(2)
D_star_map = zeros(image_size(1),image_size(2),image_size(4)); %Map of perfusion coefficients X(3)

F = @(x,xdata)x(1)*exp(-x(3)*xdata)+(1-x(1))*exp(-x(2)*xdata);

```

```
x0 = [.2  10^-3  7*10^-2]; %[PF D D*]
LB = [0.025  0.4*10^-3  5*10^-3];
UB = [0.5  0.003  0.14];


ratio = zeros(1,(total_b_values));

b_values = zeros(1,(total_b_values));
b_values(1:total_b_values) = unique_b_values;


opts = optimset('Algorithm','levenberg-marquardt');


for k = 1:image_size(4)
    for l = 1:image_size(1)
        for m = 1:image_size(2)
            if roi_mask(l,m,k) == 1
                for b = 1:total_b_values
                    ratio(b) = movingRegistered(l,m,b,k)/
                        movingRegistered(l,m,1,k);
                end

                for b = (total_b_values+6):length(ratio)
                    ratio(b) = movingRegistered(l,m,
```

```
                    total_b_values,k)/movingRegistered(l,m,1,k);
                end

                X = lsqcurvefit(F,x0,b_values,ratio,LB,UB,opts);
                f_map(l,m,k) = X(1);
                D_map(l,m,k) = X(2);
                D_star_map(l,m,k) = X(3);
            else
                f_map(l,m,k) = NaN;
                D_map(l,m,k) = NaN;
                D_star_map(l,m,k) = NaN;
            end
        end
    end
end
end
```

B.9 Texture analysis

```
function [TA_values] = TA_calc(full_matrix)
%Calculates texture analysis features by slice for the volume
image_size = size(full_matrix);


for s = 1:image_size(4)
```

```
    im_slice = full_matrix(:,:,:,s);

    for b = 1:image_size(3)
        a_roi_entropy(b,s) = mean(mean(entropy(im_slice(:,:,b))));
        a_roi_entropyfilt(b,s) = mean(mean(entropyfilt(im_slice(:,:,b))));
        a_roi_rangefilt(b,s) = mean(mean(rangefilt(im_slice(:,:,b))));
        a_roi_stdfilt(b,s) = mean(mean(stdfilt(im_slice(:,:,b))));
        calced_graycomatrix(:,:,b,s) = graycomatrix(im_slice(:,:,b));
        a_glcm_stats(b,s) = graycoprops(calced_graycomatrix(:,:,b,s));

    end

end
```

VITA

Benjamin Charles Lewis was born on June 8, 1992, in Naperville, Illinois. He graduated from Naperville North High School, Naperville, Illinois in 2010. He received his Artium Baccalaurei in Physics from Washington University in St. Louis, St. Louis, Missouri, in May 2014. In August 2014, he entered the Medical Physics Graduate Program at Virginia Commonwealth University and joined the research group of Dr. Siyong Kim. While completing his degree at VCU, Ben published "A pressure based respiratory motion management system with biofeedback for MR-based radiotherapy" in *Biomedical Physics and Engineering Express* and "Monitoring frequency of intra-fraction patient motion using the ExacTrac system for LINAC-based SRS treatments" in *The Journal of Applied Clinical Medical Physics*. He also was the primary author on six oral presentations at the national meetings of AAPM and ISMRM, and two poster presentations. In addition, he was co-author on two peer-reviewed research articles and a meeting abstract. For his academic achievements, Ben was selected by the School of Medicine to receive the MCV Alumni Association's Basic Health Sciences award.